

University of Pretoria

# Development of numerical techniques for evaluation of point-focus solar cavity receiver performance

by

Justin Marsberg

Under the supervision of

Prof KJ Craig

Prof JP Meyer

Submitted in partial fulfilment for the degree of

Master of Engineering (Mechanical)

Department of Mechanical and Aeronautical Engineering

2018

# Abstract

**Title:** Development of numerical techniques for evaluation of point-focus solar cavity receiver performance

**Author:** J Marsberg

**Student number:** 28051123

**Supervisors:** Prof KJ Craig; Prof JP Meyer

Solar receiver cavities, which are designed to absorb large amounts of concentrated solar irradiation, form the central component of a solar collection plant. Since this receiver's efficiency is directly proportional to the plant's overall performance, the optimum design of these receivers is an important research field, as it is key to the maximisation of electricity output, while maintaining reasonable costs as an alternative to the high costs of fossil fuel energy generation technologies.

Due to the high temperatures that are reached inside a solar receiver, the prediction of heat flux distribution and the subsequent effects on conjugate heat transfer have been key areas of research in the solar field. Initially dominated by experimental studies, research has trended towards numerical prediction using finite volume methods (FVM), due to the low turnaround time and cost-effective nature of this type of analysis.

Owing to the need to accurately predict these heat flux distributions, a methodology to numerically simulate concentrated heat flux on complex surfaces of a solar receiver is developed. A combination of Monte Carlo ray tracing (MCRT) methods and computational fluid dynamics (CFD) is implemented to estimate system performance, while minimising computational time and expense, with limited sacrifice of accuracy.

After successful validation of this method with experimental data, iterative performance simulations on a candidate geometry, implemented in a realistic solar-concentrating field, are performed to showcase the ability of the methodology to accurately predict system performance. The sample geometry is based on a number of implementations from various case studies and receivers that are used nowadays, with each iteration allowing for parameter adjustment to maximise optical and thermal efficiency.

Key result outputs include the prediction of heat flux distributions and subsequent thermal stress raisers, such as hot spots, convective and re-radiation heat losses, and operating temperatures. Determining which of these thermal stress raisers from the implementation of this model can further improve and streamline designs.

# Acknowledgments

I would like to acknowledge the following people for their support and contribution throughout the completion of this dissertation:

- Prof KJ Craig, for his infinite patience, hours of help and relentless belief and guidance throughout the duration of my time at the University of Pretoria
- My parents, for their endless patience and understanding throughout this process
- Ms KJ Scheepers, for her never-ending love, support and motivation
- Mr WJ Reid for being the best office mate, sounding board and friend
- The National Research Foundation (NRF) (Solar Spoke) and the University of Pretoria for the funding of my bursary



# Table of contents

Abstract .....	i
Acknowledgments.....	ii
Table of contents.....	iii
List of figures.....	vii
List of tables.....	xi
List of symbols.....	xii
Chapter 1: Introduction.....	1
1.1 Background.....	1
1.2 Problem statement.....	6
1.3 Objectives of the study.....	7
1.4 Scope.....	7
1.5 Dissertation layout .....	8
Chapter 2: Literature review .....	9
2.1 Preamble .....	9
2.2 Solar receiver design.....	9
2.2.1 Conventional solar receiver designs.....	9
2.2.2 Suggested concept.....	16
2.3 Conjugate heat transfer .....	17
2.3.1 Internal forced convection to HTF.....	18
2.3.2 Convective heat losses .....	19
2.3.3 Internal and external radiation and re-radiation effects .....	20
2.4 Determining the performance of solar collectors.....	21
2.4.1 Optical efficiency .....	22
2.4.2 Thermal efficiency .....	22
2.4.3 Overall efficiency.....	23
2.4.4 Efficiency calculation using FVM .....	23
2.4.5 Efficiency calculation using MCRT .....	23
2.5 Finite volume method .....	24
2.5.1 Governing equations .....	24
2.5.2 Determining convergence .....	24



2.5.3	Solving of the radiative transfer equation .....	25
2.6	Monte Carlo ray tracing .....	26
2.7	Numerical estimation of solar loads.....	28
2.8	Additional considerations .....	29
2.8.1	Thermal stress and hot spots .....	29
2.8.2	Coatings .....	29
2.8.3	Glass.....	30
2.9	Conclusion .....	30
Chapter 3: Numerical methods .....		31
3.1	Preamble .....	31
3.2	Radiation modelling using RTE.....	31
3.2.1	Finite volume solution of RTE using discrete ordinates .....	31
3.2.2	Biomass cavity receiver .....	32
3.2.3	Multi-tube solar reactor case study .....	34
3.3	Modelling complex geometry .....	36
3.3.1	Parabolic tubular cavity receiver case.....	36
3.3.2	Complex geometry modelling methodology.....	38
3.3.3	Heat source patching with Brayton cycle test case .....	40
3.4	Conclusion .....	43
Chapter 4: Verification and validation .....		44
4.1	Preamble .....	44
4.2	Experimental case for validation.....	44
4.3	CFD model validation.....	48
4.3.1	Computational domain setup .....	48
4.3.2	Boundary conditions .....	51
4.4	Comparison of model validation results .....	52
4.5	Conclusion .....	54
Chapter 5: An iterative analysis of cavity receiver performance.....		56
5.1	Preamble .....	56
5.2	Problem definition .....	56
5.2.1	Power source.....	56
5.2.2	Thermal cycle.....	57



5.2.3	Objective function.....	60
5.2.4	Constraints .....	62
5.3	Numerical setup .....	62
5.3.1	Initial conditions .....	62
5.3.2	Materials and properties.....	62
5.3.3	Boundary conditions .....	66
5.3.4	Solver setup.....	68
5.3.5	Convergence criteria .....	68
5.3.6	SolTrace .....	69
5.4	Simulation implementation and results.....	72
5.4.1	First generation .....	72
5.4.2	Second generation.....	77
5.5	Optimisation.....	83
5.5.1	Design of experiments .....	83
5.5.2	Response surface and sensitivity analysis.....	84
5.5.3	Goal-driven optimisation .....	84
5.6	Conclusion .....	85
Chapter 6: Conclusion .....		86
6.1	Preamble .....	86
6.2	Scope of future work.....	86
6.2.1	Convective losses from cavity receivers .....	86
6.2.2	SolTrace complex surface modelling.....	87
6.2.3	Full optimisation study.....	88
6.3	Conclusion .....	88
References .....		89
Appendix A:	UDF Copy UDS to UDM.....	A1
Appendix B:	Python Functions for SolTrace Mesh Import.....	B1
	Code overview .....	B1
	Python main executable code .....	B1
	Read_MSH_Func.py .....	B2
	Optic_Lib_Tools.py.....	B14
Appendix C:	SolTrace Functions .....	C1



Code overview .....	C1
Import mesh elements.....	C1
Write.ip file.....	C8
Write profile file .....	C11

# List of figures

Figure 1.1: Renewable Energy Independent Power Producer Programme (REIPPP) growth in energy produced during 2014 (Department of Energy, 2015) .....	1
Figure 1.2: A direct normal irradiation map of South Africa (GeoSun Africa, 2016).....	2
Figure 1.3: An illustration of a basic CST plant system (Hamilton, 2010, Hamilton and Statistics, 2011) .....	3
Figure 1.4(a): Linear Fresnel (TUBOSOL PE2, 2011); and (b): parabolic trough line-focus systems (Rajput, 2010) .....	3
Figure 1.5(a): Parabolic dish (Tessera Solar, 2010) and (b): central solar power (CSP) receiver (Abengoa Solar, 2018) point-focus systems .....	4
Figure 1.6: !Khi Solar One (Upington, South Africa) in operation with (a): 1 482 acre heliostat field; and (b): close-up of the 50 MW CST (Abengoa Solar, 2018) .....	5
Figure 2.1: Schematic of open and cavity CSP receivers (Ho and Iverson, 2014) .....	10
Figure 2.2(a): REFOS receiver module (Buck et al., 2001); and (b): HiTRec receiver (Hoffschmidt et al., 2003) .....	11
Figure 2.3: Solid particle receiver used in water-splitting thermo-chemical process (Chen et al., 2006) .....	12
Figure 2.4: Arrangement and cross-section through pyramid geometry (Garbrecht et al., 2013) .....	12
Figure 2.5: Conceptual SCRAP receiver (Lubkoll, 2017) .....	13
Figure 2.6: Multistage solar receiver (Kribus et al., 1999) .....	14
Figure 2.7: Tubular cavity receivers for (a): the Solugas project (Korzynietz et al., 2016); and (b): the SOLHYCO project (Jedamski et al., 2010) .....	14
Figure 2.8: Direct exposure internal falling film receiver for use in surrounding field CST applications (Ho and Iverson, 2014) .....	15
Figure 2.9: Tubular cavity receiver for direct steam generation on a dish concentrator (Pye et al., 2015) .....	16
Figure 2.10: Suggested tubular cavity receiver concept .....	17
Figure 2.11: Conjugate heat transfer for the conceptual tubular cavity receiver .....	18
Figure 2.12: (a) Internal forced convection for cylinder (Cengel and Ghajar, 2011); and (b) applied non-uniform heat flux solution using a differential control volume .....	19
Figure 2.13: Geometry of axisymmetric dimpled tube (Chen et al., 2001) .....	19
Figure 2.14: Convective heat loss from example cavity at 30° inclination angle with variable size of aperture (Li et al., 2015) .....	20
Figure 2.15(a): The electromagnetic spectrum; and (b): diffusivity of a blackbody and real surface (Cengel and Ghajar, 2011).....	20

Figure 2.16: Comparison between blackbody, grey surface and real surface emissivity .....	21
Figure 2.17: Angular discretisation of discrete ordinates method (Versteeg and Malalasekera, 2007)	26
Figure 2.18: Replication of PS10 field in SolTrace .....	27
Figure 2.19: Definition of an element in SolTrace .....	27
Figure 2.20: Probabilistic outcomes of ray interactions with SolTrace Surfaces (Wendelin et al., 2013) .....	28
Figure 2.21: The magnified condition of multi-layer tube interface, after (a): 0; (b): 50; and (c): 500 cycles (Buck et al., 2001).....	29
Figure 3.1: Theoretical 2D radiation test case (Moghimi et al., 2015) .....	31
Figure 3.2: The test case result comparison with MCRT using second-order DO settings $100 \times 100$ mesh and $N\theta \times N\phi$ of $3 \times 40$ (Moghimi et al., 2015).....	32
Figure 3.3: A reflective cavity multi-tube solar reactor (Lichy et al., 2010) .....	32
Figure 3.4: The biogas receiver configuration for: (a) one pipe; and (b): five pipes (Martinek and Weimer, 2013) .....	33
Figure 3.5: The normalised heat flux $qs, n$ on pipe surface for (a): a single-pipe absorbing cavity; and (b): a reflecting cavity .....	33
Figure 3.6: The normalised heat flux values $qs, n$ for (a): the front pipe; and (b): the back pipe in a five- pipe reflective cavity receiver .....	34
Figure 3.7(a): Gaussian; and (b) MCRT solution heat flux maps .....	35
Figure 3.8(a): The incident radiation distribution for MCRT solution solar load; and (b): temperature on the surface of the middle tubes .....	36
Figure 3.9(a): Tubular receiver geometry of test case; and (b): experimental setup of parabolic dish and tubular receiver (Craig et al., 2015) .....	37
Figure 3.10: Incident radiation contours $[W/m^2]$ , for (a): axisymmetric (DO $80 \times 80$ ); and (b): full 3D model (DO $25 \times 25$ ) (Craig et al., 2015).....	37
Figure 3.11: Total absorbed radiation $[W]$ on receiver tube for the 2 <sup>nd</sup> order (2ndO) Discrete Ordinates axisymmetric and 3D case (Craig et al., 2015) .....	38
Figure 3.12: Flow diagram depicting the process of producing a heat flux distribution over a complex geometry surface.....	39
Figure 3.13(a): A replication of meshed surface using circles in SolTrace; and (b): points used in Python script to calculate the properties of the element.....	39
Figure 3.14: Tubular receiver geometry (a): position in SolTrace simulation and close-up with (b): coarse mesh (3 629 elements); and (c): fine mesh (46 423 elements) used to represent a complex surface .....	41
Figure 3.15: Absorbed radiation flux $[W/m^2]$ on tubular cavity walls plotted as a function of cavity vertical position $[m]$ for different mesh sizes used and 1 million SolTrace ray intersections .....	42

Figure 3.16: The CFD simulation of heating of HTF (a): surface temperature; (b): tube temperature distribution (Craig et al., 2016b); and (c) as a result of applied solar absorbed radiation (Craig et al., 2015).....	43
Figure 4.1: Parabolic dish and helical absorber experimental setup (Maharaj, 2015).....	45
Figure 4.2: Numerical representation of experimental geometry in ANSYS SpaceClaim.....	45
Figure 4.3(a): Representation of geometry in SolTrace computational domain; and (b): zoomed view of insulation cone and sting shadow.....	46
Figure 4.4: A numerical representation of helical absorber tube in the SolTrace computational domain using 1.9 M plotted rays.....	47
Figure 4.5(a): Coarse mesh; and (b): fine mesh using 24 K and 100 K elements, respectively .....	47
Figure 4.6: Convergence study indicating the element number versus the number of generated rays .	48
Figure 4.7: Validation case pipe mesh and HTF inflation layer .....	49
Figure 4.8: A numerical model of receiver cavity and boundary conditions .....	50
Figure 4.9: An example of SolTrace data patched to the equivalent volume in ANSYS Fluent with corresponding percentage errors of interpolated values.....	51
Figure 4.10: Temperature contours for the plane and inner absorber tube for the validation case .....	53
Figure 4.11: The temperature distribution on the tubular absorber surface .....	54
Figure 5.1: Helio100 (S.T.E.R.G., 2017).....	56
Figure 5.2: The Brayton cycle.....	57
Figure 5.3: Parameterised cavity.....	59
Figure 5.4: The candidate tubular high-pressure air receiver geometry with bounding box dimensions .....	60
Figure 5.5: The iterative determination of the performance flow diagram.....	61
Figure 5.6: The PML tube with corresponding dimensions (Jedamski et al., 2010) .....	64
Figure 5.7: The total hemispherical emittance as a function of temperature for Pyromark 2500 (Ho et al., 2012) .....	66
Figure 5.8: Absorption spectra of Philips 441 glass (Loenen and Van der Tempel, 1996) .....	68
Figure 5.9(a): SolTrace receiver geometry; and (b): detailed sectional view used for iterative cases..	70
Figure 5.10: A candidate cavity receiver with: (a) a full system view; and (b): a detailed cavity view	71
Figure 5.11: Variation of the focal point.....	71
Figure 5.12(a): Optical efficiencies; and (b): thermal efficiencies for a first-generation receiver with variation in the focal point .....	74
Figure 5.13: Variation of absorber tube surface temperature vs cavity height with a variation in focal point .....	76
Figure 5.14: Heat loss with corresponding heat transfer to the HTF for first-generation receivers .....	76



Figure 5.15: The maximum recorded temperatures for key components in first-generation receiver geometry ..... 77

Figure 5.16(a): The optical efficiencies; and (b): the thermal efficiencies for the second generation with variation in the focal point ..... 79

Figure 5.17: The variation of absorber tube surface temperature vs cavity height with a variation in focal point ..... 80

Figure 5.18: Heat loss with corresponding outlet temperature for second-generation receivers ..... 81

Figure 5.19: The maximum recorded temperatures for key components in second-generation receiver geometry ..... 82

Figure 6.1: An open cavity receiver that experiences convective loss (Pye et al., 2015) ..... 86

Figure 6.2(a): The shadowing zone due to circular elements; and (b): irregular quadrilateral elements used to minimise shadowing effects ..... 87

# List of tables

Table 1.1: Global CSP plants at commercial scale capacity listed in descending output capacity (NREL, 2017) .....	5
Table 2.1: Classification of volumetric absorbers (Ávila-Marín, 2011) .....	11
Table 3.1: Biomass cavity simulation properties .....	35
Table 3.2: Comparison of the absorbed radiation flux on tubular walls in SolTrace and integrated volumetric heat sources in ANSYS Fluent, using DNI = 1000 W/m <sup>2</sup> .....	42
Table 4.1: Validation case material properties (Maharaj, 2015) .....	50
Table 4.2: Boundary conditions used for the validation case based on Maharaj (2015) .....	52
Table 4.3: Radiation and total heat transfer rates at validation case boundaries .....	52
Table 4.4: Comparison of the experimental and numerical results .....	53
Table 5.1: The variable states of a typical Brayton cycle (Korzynietz et al., 2016) .....	58
Table 5.2: Ideal gas properties of air at 10 bar (Sonntag et al., 1998) .....	63
Table 5.3: Insulation material properties for use in high-flux receivers (Ebert et al., 2015) .....	64
Table 5.4: Properties of Heraeus’s fused silica (Heraeus, 2017) .....	65
Table 5.5: General atmospheric properties .....	67
Table 5.6: Stage descriptions used in SolTrace simulations .....	70
Table 5.7: The first-generation geometry parameters and graphical representation .....	73
Table 5.8: The first-generation outlet temperature and efficiencies .....	73
Table 5.9: Contour maps for temperature and incident radiation distribution for a first-generation receiver with variation in the focal point .....	75
Table 5.10: Second-generation geometry parameters and graphic representation .....	78
Table 5.11: Second-generation outlet temperature and efficiencies .....	78
Table 5.12: Contour maps for temperature and incident radiation distribution for the second-generation receiver with variation in the focal point .....	80
Table 5.13: Variables for use in the design of experiments .....	83



# List of symbols

Symbol	Description	Units
$\dot{Q}_{conv}$	Convective heat transfer	$W$
$Q_{HTF}$	Net HTF heat transfer	$W$
$\dot{q}_{rad}$	Radiative heat flux	$W/m^2$
$A_{tube}$	Surface area of inner tube wall	$m^2$
$A_{aper}$	Aperture Area	$m^2$
$h$	Heat transfer coefficient	$W/m^2K$
$A_s$	Area	$m^2$
$L$	Length	$m$
$T$	Temperature	$K$
$s$	Window Thickness	$m$
$Nu$	Nusselt number	-
$k$	Thermal conductivity	$W/mK$
$d$	Diameter	$m$
$\dot{m}$	Mass flow rate	$kg \cdot s^{-1}$
$C_p$	Heat capacity at constant pressure	$\frac{J}{kg \cdot K}$
$\rho$	Density	$kg \cdot m^{-3}$
$v$	Velocity	$m \cdot s^{-1}$
$t$	Time	$s$
$p$	Pressure	$Pa$
$E$	Energy	$W$



$\alpha_c$	Absorption coefficient	-
$S_h$	Source term	$W/m^3$

### Subscripts

$ab$	Absorbed
$i$	Inlet
$e$	Outlet
$op$	Optical
$proj$	Projected area
$rad$	Radiation
$refl$	Reflective
$ther$	Thermal

### Greek letters

$\alpha$	Absorptivity
$\varepsilon$	Helical emissivity
$\theta_D$	Rim angle
$\kappa$	Absorption coefficient
$\tau$	Transmissivity
$\rho$	Reflectivity
$\eta$	Efficiency
$\partial$	Partial derivative

### Acronyms

AMO	Adaptive multi-objective optimisation
ASO	Adaptive single-objective optimisation
CFD	Computational fluid dynamics
CRS	Central receiver system
CSP	Concentrated solar power
CST	Central solar tower
DIAPR	Directly Irradiated Annular Pressurized Receiver
DNI	Direct normal irradiation



DO	Discrete ordinates
FVM	Finite volume method
HPAR	High-pressure air receiver
HTF	Heat transfer fluid
IR	Infrared
MCRT	Monte Carlo ray tracing
MOGA	Multi-objective genetic algorithm
NREL	National Renewable Energy Laboratory (Unites States)
NRF	National Research Foundation
PML	Profiled multi-layer
PPR	Power per ray
REFOS	Receiver for solar-hybrid gas turbine and CC systems
REIPPP	Renewable Energy Independent Power Producer Programme
RTE	Radiative transport equation
SAURAN	Southern African Universities Radiometric Network
SCRAP	Spiky Central Receiver Air Pre-heater
SOLHYCO	Solar-hybrid power and cogeneration plants
SRP	Salt River Project
SST	Shear Stress Transport
STERG	Solar Thermal Energy Research Group (Stellenbosch University, South Africa)
UDF	User-defined function
UDM	User-defined memory
UDS	User-defined scalar
UV	Ultraviolet

# Chapter 1: Introduction

## 1.1 Background

It has become well known that there is a growing need to reduce the burning of fossil fuels in order to reduce harmful by-products, such as carbon dioxide, that lead to climate change. With greenhouse gas emissions predicted to double by 2050, natural gas and oil resources diminishing and their prices projected to double in 20 years, it has become necessary to develop cleaner and more environmentally friendly alternatives in energy generation (Behar et al., 2013). Alternative power-generation methods include, but are not limited to, solar, nuclear, hydrodynamic and wind power, which all fit these criteria.

Many countries around the world have already adopted renewable power-generation programmes with great success. World leaders in renewable power generation include Spain, Germany, India and China (Department of Energy, 2015). Considerable contributions also include countries such as Sweden and Austria, which produce over 60% of their total power output from renewable sources (Eurostat, 2015). South Africa has also begun the process of integrating alternative energy sources into its own grid. As can be seen in Figure 1.1, in 2015 alone, South Africa raised its monthly output from wind and photovoltaic plants by almost 720%.

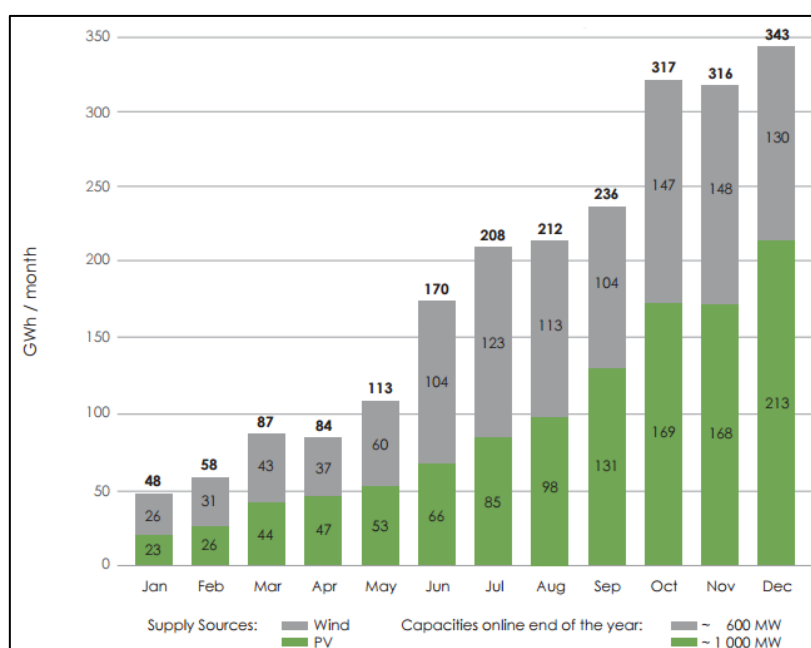


Figure 1.1: Renewable Energy Independent Power Producer Programme (REIPPP) growth in energy produced during 2014 (Department of Energy, 2015)

Since South Africa has one of the best solar resources in the world, with good distribution over large areas of the country, (see Figure 1.2), solar energy generation has continuously become a more viable option, not only in the reduction of emissions, but also to improve the reliability of supply from the current grid.

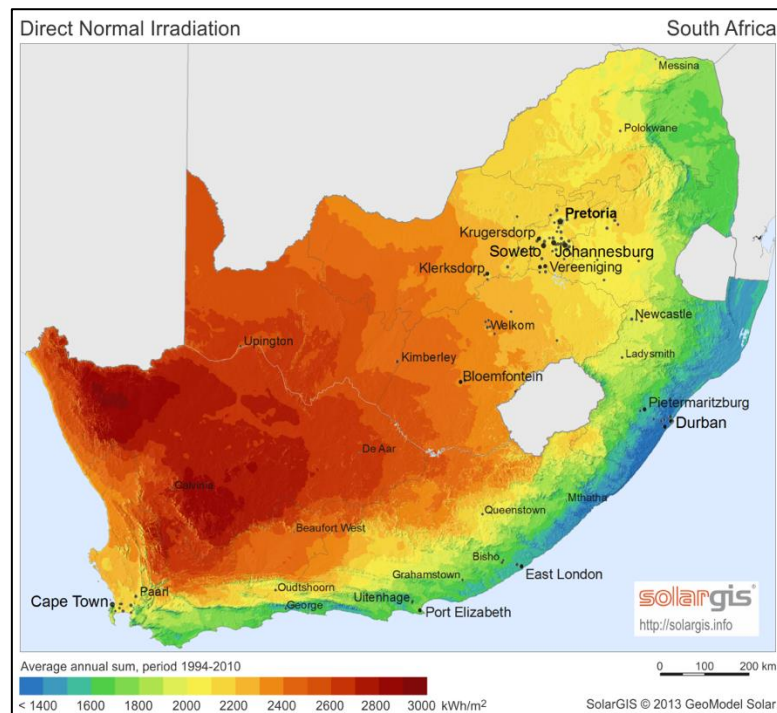


Figure 1.2: A direct normal irradiation map of South Africa (GeoSun Africa, 2016)

Solar power plants operate with the same major systems in place, with a possibility of additional subsystems being integrated. The main systems needed for the plant to operate (Behar et al., 2013), as illustrated by the central solar tower (CST) plant in Figure 1.3, are the following:

- Collectors: Reflective surfaces, usually mirrors, the geometry of which is such that they can concentrate reflected irradiation onto a point of focus either individually, or as a multi-faceted entity
- Receivers: Geometries that contain a means of harnessing solar irradiation, and transferring this energy to a specialised fluid, known as heat transfer fluid, as a means of transporting this energy to the power-generation system
- Power-generation systems: Power-generation systems can vary from using pre-heated air for a Brayton cycle, to Rankine cycles using generated steam, either from direct conversion in the receiver, or from stored energy, via heat exchange

The following subsystems can be included:

- Thermal storage: Means of thermally storing collected energy to be utilised later in the power-generation cycle. Thermal storage solutions include fluidised rock bed storage, or thermal “molten salt” batteries.
- Backup systems: To ensure that the plant can provide a certain amount of energy to critical systems during down times, or low-sun conditions, to prevent the freezing of molten salt in thermal storage systems, alternative heat generation systems are installed, such as natural gas burners, diesel generators, or drawing energy from the grid.

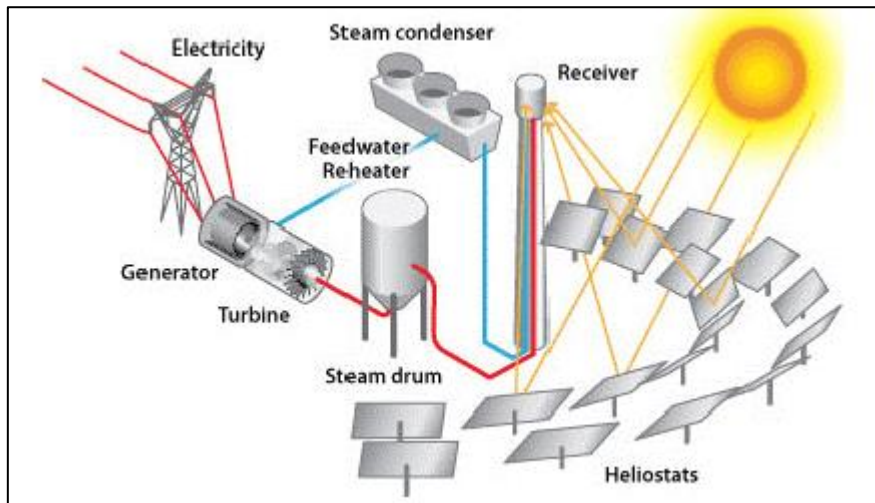


Figure 1.3: An illustration of a basic CST plant system (Hamilton, 2010, Hamilton and Statistics, 2011)

Solar collector or receiver systems, which are largely used as the renewable energy replacement to fossil fuel systems, or indeed as additional power systems for conventional power plants, can be divided into two major categories. These are line-focus and point-focus systems (see Figure 1.4 and Figure 1.5). This dissertation focuses on central receiver or point-focus systems, with specific emphasis on the prediction of solar irradiation distribution on cavity receiver-absorbing surfaces, and the consequent conjugate heat transfer calculation solved with the finite volume method (FVM).



Figure 1.4(a): Linear Fresnel (TUBOSOL PE2, 2011); and (b): parabolic trough line-focus systems (Rajput, 2010)

The two main systems included in the point-focus category are parabolic dish concentrators and CST receivers, as seen in Figure 1.5(a) and Figure 1.5(b), respectively. A parabolic dish receiver consists of a cavity receiver that is situated at the focal point of a circular parabolically curved dish. These systems can be used individually, generating a few kW, to power small turbines or Stirling engines, or in combination with each other for higher energy generation applications at the plant level.



(a)



(b)

*Figure 1.5(a): Parabolic dish (Tessera Solar, 2010) and (b): central solar power (CSP) receiver (Abengoa Solar, 2018) point-focus systems*

Due to the high temperatures that are reached in the receiver, some systems use superheated steam or molten salts to transport and store the collected energy. To operate a standard Rankine cycle, it is possible to generate and feed the turbine directly with superheated steam. Otherwise, if molten salt is the working fluid, steam will need to be generated by means of heat exchangers. The use of molten salt has numerous advantages, including a much higher change of state temperatures, higher heat capacities that allow more controllable flow rates and superior storage capabilities (Kolb et al., 1991).

Receiver systems can also be used in a number of other cycle types, such as in high-pressurised air systems like the Brayton cycle (Korzynietz et al., 2016), or in systems used for the desalination of sea water (Ghazy and Fath, 2016).

There are a number of commercial CSP towers in operation, the largest being the Ivanpah Solar Power Facility in California. It produces 392 MW (BrightSource Energy Inc, 2015). Several other CSP plants are in the planning phase at key high-irradiation areas all over the world. South Africa has an operational CSP plant in Upington (see Figure 1.6(a)). This plant is Abengoa's first attempt at CSP technology in South Africa and is known as !Khe Solar One. It was commissioned in 2016 (Abengoa Solar, 2018). The 110 MW Crescent Dunes facility in the USA is the most recent CST plant to be commissioned. Many more plants are in the construction phase, with even more plants planned for construction in the near future (see Table 1.1).



Figure 1.6: !Khi Solar One (Upington, South Africa) in operation with (a): 1 482 acre heliostat field; and (b): close-up of the 50 MW CST (Abengoa Solar, 2018)

The large number of plants that are planned indicate a global drive towards the implementation of this solar energy technology, which confirms the need for further development and system improvement in this direction. In particular, the Chinese have been attempting to reach a 20 GW CSP output, which resulted in a substantial number of CSP plants being developed.

Table 1.1: Global CSP plants at commercial scale capacity listed in descending output capacity (NREL, 2017)

Name	Location	Capacity (MW)	Year of commission
<b>Operational</b>			
<b>Ivanpah Solar Power Facility</b>	USA	392	2014
<b>Crescent Dunes Solar Energy Project</b>	USA	110	2015
<b>!Khi Solar One</b>	South Africa	50	2016
<b>PS 20</b>	Spain	20	2009
<b>PS 10</b>	Spain	11	2007
<b>Under construction</b>			
<b>Noor III</b>	Morocco	150	2017
<b>Ashalim Power Station 1</b>	Israel	121	2017
<b>Atacama 1</b>	Chile	110	2018
<b>Redstone Solar Thermal Power</b>	South Africa	100	2018
<b>SunCan Dunhuang 100 MW Phase II</b>	China	100	2017
<b>Under development</b>			
<b>Sandstone Solar Energy Project</b>	USA	1 600	2022
<b>Tamarugal Solar Project</b>	Chile	450	2021



<b>Likana Solar Project</b>	Chile	390	2021
<b>Copiapó Solar Project</b>	Chile	260	2019
<b>Golmud</b>	China	200	2018
<b>Aurora Solar Thermal Power Project</b>	Australia	150	2020
<b>Huanghe Qinghai Delingha</b>	China	135	2017
<b>Dubai Electricity and Water Authority CSP Tower Project</b>	Dubai	100	2019
<b>Golden Tower 100 MW Molten Salt project</b>	China	100	-
<b>Yemen 100 MW Molten Salt Tower</b>	China	100	-
<b>Minos</b>	Greece	52	2020
<b>AZ 20</b>	Spain	50	-
<b>Hami</b>	China	50	2018
<b>Qinghai Gonghe</b>	China	50	-
<b>Shangyi</b>	China	50	-
<b>Supcon Solar Project</b>	China	50	-
<b>Yemen 50 MW Molten Salt Tower</b>	China	50	2018

## 1.2 Problem statement

Solar receivers in point-concentration systems are subject to many factors and variable conditions that will determine their performance. The fact that cavity receivers are subject to variations in solar load, and variations in heat flux distribution, makes the design and implementation of a solar cavity intricate. These variations in maximum load and distribution can lead to optical and thermal losses due to convective and re-radiation heat loss in particular, due to temperatures reaching more than 1 000 °C (Korzynietz et al., 2016), or thermal stresses in materials of the receiver due to the formation of hot spots.

The maximum performance of these receivers can be achieved by ensuring that the energy entering the cavity from the concentrating heliostat field or other point-concentration source is absorbed by the heat transfer fluid (HTF) as efficiently as possible. Inefficiencies can be reduced by improving the system's geometries, materials and coatings. Since the receiver is the primary mode of energy conversion into a mechanical form, it is paramount to the overall functioning and efficiency of the system. This study aims to predict the system performance accurately and recommend improvements.

Several numerical and experimental studies on point-concentration receivers, most notably those by Behar et al. (2013), Ávila-Marín (2011) and Ho and Iverson (2014), are available in literature. However, these studies have not reasonably addressed the problem of integration between realistic numerical solar load predictions and conjugate heat transfer such as the FVM. Ideas for combining ray tracing and FVM have been introduced (Cheng et al., 2013), but it is still possible to expand on these concepts, which

allow the accurate prediction of radiation heat transfer and the subsequent evaluation of CST system performance.

Accurately and numerically simulating solar receiver systems with a discretisation method to solve for radiative heat transfer, such as using the FVM to solve for the radiative transport equation (RTE), has proved to be extremely computationally expensive and time-consuming. An investigation of this nature, and the development of a numerical methodology that improves simulation accuracy, while reducing computational expense and time, will help lead to more streamlined designs, reducing costs and improving the efficiency of renewable energy systems as a whole.

### 1.3 Objectives of the study

In order to address the problem statement, the following objectives have been identified:

- Complete a comprehensive literature study that highlights solutions that are currently available
- Develop numerical methods that assist in the reduction of computational time while not sacrificing solution accuracy
- Verify the accuracy of the proposed models
- Validate the methodology when numerical results are compared to experimental data
- Prove the capabilities of the developed methods in an iterative performance analysis of a novel sample geometry

### 1.4 Scope

This dissertation includes the following key components:

- Investigation into technology that is currently available, while highlighting key features of each design, as well as advantages and disadvantages
- Development of a numerical model that incorporates Monte Carlo ray tracing (MCRT) and the FVM
- Investigation of the effect on mesh size, RTE discretisation and number of generated rays in numerical simulations on solution accuracy
- Iterative geometry analysis to prove the efficiency of the developed methodology

Certain aspects that are excluded from this study are recommended for future study, and discussed in detail in Chapter 6 of this dissertation. The most notable of these limitations are the following:

- The effect of removing the glass cover at receiver apertures and, by extension, the effect of natural convective heat loss due to the buoyancy effect on the receiver cavity
- Objective function-driven optimisation using fully parameterised geometry
- The influence of mounting the cavity receiver at an angle on conjugate heat transfer
- Heliostat field optimisation

## 1.5 Dissertation layout

This chapter gives background information on solar energy technology, with comparisons drawn between point- and line-focus systems, to provide a clear understanding of the necessity of this study. Specifically, more in-depth information is given on cavity receivers, since these form the foundation of this study. The necessity of the numerical prediction of solar loads and integration with conjugate heat transfer solutions was given as the problem statement. Objectives were then identified to address the formulated research problems and prove the capabilities of the developed methodology.

In Chapter 2, a general overview of existing cavity receivers is given, including components, materials and geometry layouts used in these systems. More detailed literature concerning ray-tracing methods, and conjugate heat transfer, as well as numerous numerical and experimental case studies on receiver design and performance prediction, is also included.

Chapter 3 discusses the numerical methodology that has been developed to integrate ray-tracing methods with conjugate heat transfer. The validation of this methodology is performed in Chapter 4 by means of comparison with experimental research data, while Chapter 5 goes on to expand on the numerical models that are presented and extended to the execution of iterative geometry performance analysis and improvements.

Chapter 4 is dedicated to the validation of the developed methodology with experimentally acquired data, including studies on required mesh size and number of generated rays to reduce interpolation errors.

Chapter 5 uses an iterative process of geometry assessment to prove that the proposed methodology can provide an efficient, accurate solution to determine candidate design performance.

Chapter 6 is devoted to concluding statements that finalise this dissertation. Proposed future work is included, together with suggested improvements to the evaluated numerical models and the addition of more complex numerical methods.

# Chapter 2: Literature review

## 2.1 Preamble

A vast number of published works is available that cover the topic of solar energy in every aspect. Much of this literature discusses central solar receiver technologies, ranging from a broad, comparative viewpoint to more detailed studies on proposed design and analysis methods. Central receiver system (CRS) technology has been pinned as one of the most feasible options of solar powered systems to replace conventional fossil fuel power plants due to their high efficiency and working temperature when compared to line-focus systems (Behar et al., 2013). More detailed studies have also drawn comparisons between the various existing types of CRSs, which this literature review considers.

Initially, a comprehensive summary is given to highlight the broader aspects of the existing technologies. This is then supported by more specific information regarding receivers that are in use today, as well as innovative designs that have been suggested as improvements to current receiver performance.

An overview of the physical aspects that govern the performance of solar receivers is discussed to gain an understanding of fundamental principles that will need to be implemented in the development of methods, as well as to structure the case studies in the following chapters of this thesis.

System analysis methods are considered, with information given on experimental studies of receivers, as well as the use of numerical tools such as MCRT and computational fluid dynamics (CFD).

## 2.2 Solar receiver design

In a CRS, the solar receiver operates as a heat exchanger by converting solar radiation energy, which has been concentrated towards its absorbing surfaces, into thermal energy. A number of criteria can be used to classify these receivers into categories and subsidiaries, depending on the geometric configurations, materials used, operating conditions and energy transfer to the HTF (Ávila-Marín, 2011, Behar et al., 2013).

### 2.2.1 Conventional solar receiver designs

Point-focus receivers can be divided into several categories, depending on a number of factors. These main categories are the following:

- Open receivers
- Volumetric receivers
- Particle receivers
- Spiky receivers
- Cavity receivers

Each of these receiver types provides certain advantages and drawbacks in their own right, depending on use situations, environmental factors and applications. Receiver performance assessment has, until more recently, shown that volumetric receivers are the more advantageous alternative when compared to cavity or tubular receivers (Ávila-Marín, 2011), as they offer greater functionality and geometric simplicity. A brief overview of each receiver type is included in the following section, highlighting main design operation and features, including strengths and drawbacks.

Modern receiver design, having drawn from various available cavity design strengths, have shown a considerable reduction in thermal losses and an increase in efficiency.

### Open receivers

The open receiver, which is the most popular receiver in point-focus systems, has been implemented in solar plants since the 1980s (Ho and Iverson, 2014), and found in modern high-output plants such as Ivanpah (BrightSource Energy Inc, 2015), and Crescent Dunes (SolarReserve, 2018). These receivers consist of tubular arrays that are typically arranged in a cylindrical configuration to transport the HTF through areas that receive concentrated sunlight. Although these arrangements can either be open or in a cavity (see Figure 2.1), the external tubular arrangement design is implemented more often. This HTF can range from water, which is incorporated into a cycle that directly generates steam for a Rankine cycle application, to a molten salt, such as KCl, which is used to increase the system's thermal efficiency, storing energy for later use. Certain open receivers, such as the HiTRec open volumetric receiver (see Figure 2.2b) uses air as a working fluid with integration into power cycles such as a Brayton cycle (Hoffschmidt et al., 2003).

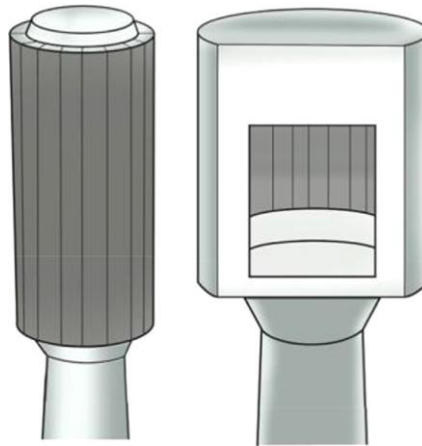


*Figure 2.1: Schematic of open and cavity CSP receivers (Ho and Iverson, 2014)*

Working temperatures are in the range of 600 °C to 750 °C, depending on the design and the working fluid that is used. These receivers can achieve optical efficiencies of up to 90% in some cases. However, due to the receiver surfaces being exposed to the ambient temperature, convective and re-radiation losses can largely affect the performance of these receivers, as they are subject to environmental conditions due to their open nature.

### Volumetric receivers

A volumetric receiver's defining characteristic is the inclusion of a highly conductive porous material, typically ceramic or metal (see examples in Figure 2.2). These receivers are described as volumetric due to the phenomenon that they produce, which is known as the volumetric effect. Since this porous material acts as a convective heat exchanger, the HTF absorbs collected energy due to the absorption of the concentrated solar radiation of the porous body (Behar et al., 2013).

A number of proposed methods assist with the further classification of volumetric receivers. A classification proposed by Ávila-Marín (2011) uses only two factors, namely operation conditions and material, to split receivers into four subgroups, as is shown in Table 2.1. This study also adopts this classification.

Table 2.1: Classification of volumetric absorbers (Ávila-Marín, 2011)

Name	Operating condition	Material
Phoebus Technology Program Solar Air Receiver	Open-loop	Metallic
SOLAIR	Open-loop	Ceramic
Receiver for solar-hybrid gas turbine and CC systems (REFOS)	Closed-loop	Metallic
Directly irradiated annular pressurised receiver (DIAPR)	Closed-loop	Ceramic

Factors that contribute to the volumetric receiver performance include considerations of porous media flow, such as permeability, conductivity and pressure drop between inlet and outlet. A large amount of experimental research has been conducted in this specific field, which helps to gain better understanding and predictions of cavity performance. These include improved pressure drop through porous media correlations, automatic controls to optimise temperature distribution, the inclusion of nanofluids, and the combination of the FVM with MCRT (Behar et al., 2013).

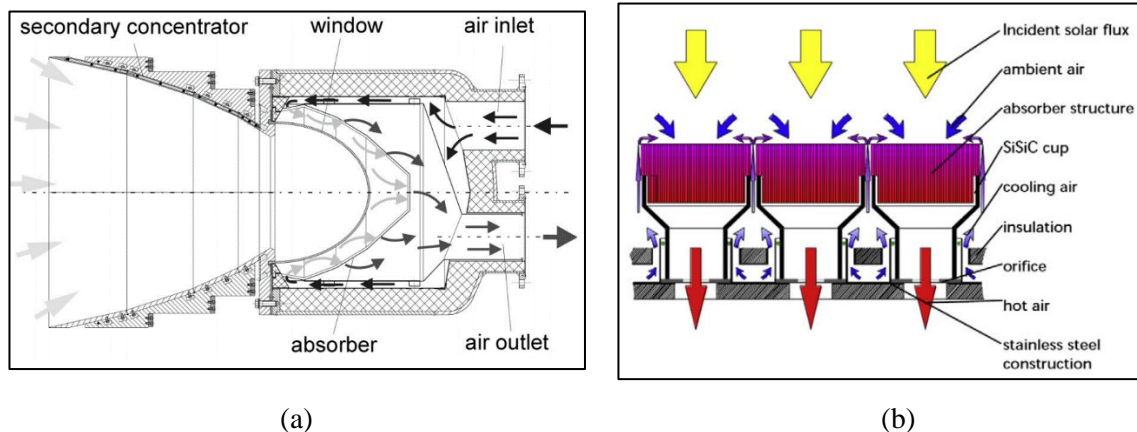


Figure 2.2(a): REFOS receiver module (Buck et al., 2001); and (b): HiTRec receiver (Hoffschmidt et al., 2003)

### Solid particle receivers

The basic concept of a solid particle receiver involves the flow of particles through a concentrated beam of solar irradiation. These particles serve as the HTF and provide thermal storage. From numerous experimental studies and implementations, it has been found that an 80% efficiency can be achieved, with a volumetric average of a 2 000 K outlet temperature of the particles (Behar et al., 2013). Factors that have been determined to affect the performance of such a system would include particle sizes, average thickness of the particle curtain and the protection of the aperture window from wind.

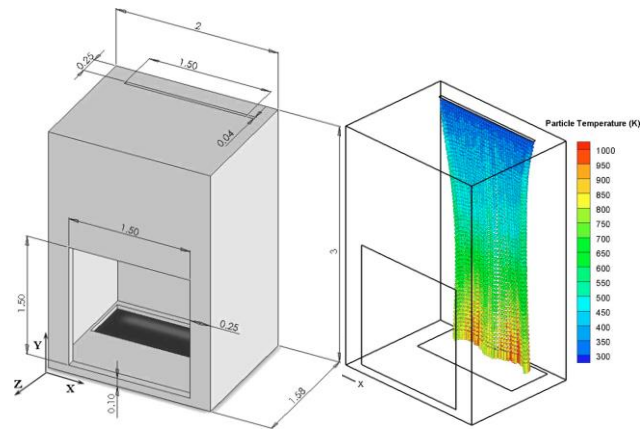


Figure 2.3: Solid particle receiver used in water-splitting thermo-chemical process (Chen et al., 2006)

Particle receivers can be integrated into various point-focus systems. However, even with a large number of laboratory tests having been completed, only a single real-world test case has ever been performed. It achieved only an approximate efficiency of 50%, and a particle temperature increase of  $\sim 250K$  (Ho and Iverson, 2014).

There is clearly still a large potential for this technology to achieve, since it is less affected by material corrosion and other limitations. However, particle movement and distribution throughout the system, particularly through concentrated solar irradiation, needs to be studied further.

### Spiky receiver

Modular-type receivers, which consist of pyramid-shaped cones or spikes, have also been proposed as a new method to capture solar energy, in this case, effectively being an open receiver design (Garbrecht et al., 2013). The cone receives solar radiation (see Figure 2.4(a)), and conducts this absorbed heat flux to a HTF flowing through the inside walls of the cone as in Figure 2.4(b). Even at high temperatures, thermal efficiencies of this system have been shown to be as high as 91.2%.

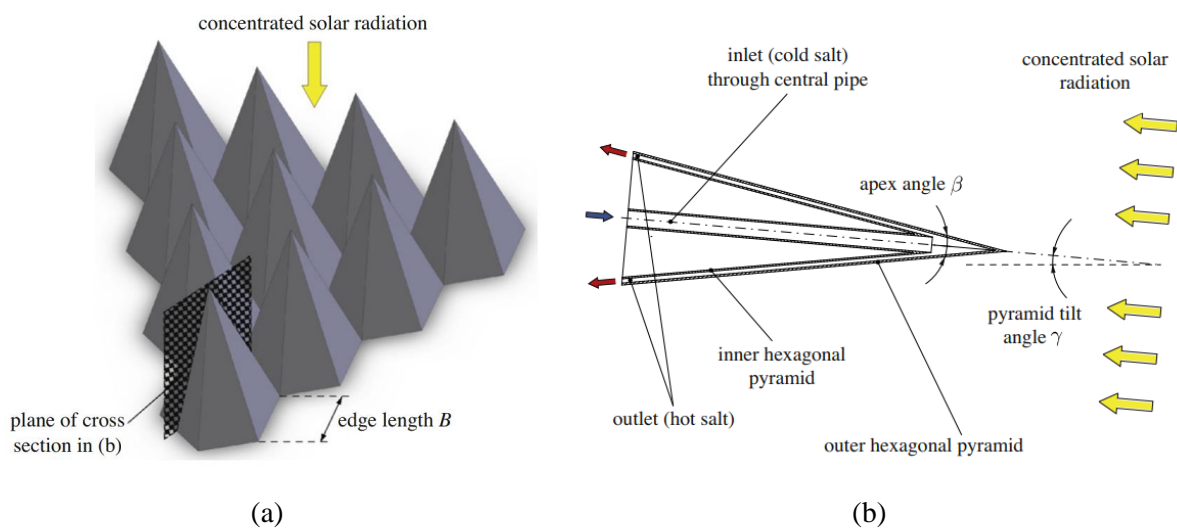


Figure 2.4: Arrangement and cross-section through pyramid geometry (Garbrecht et al., 2013)

This efficiency is largely attributed to the view factors of the pyramid's surfaces that re-radiate any losses directly to neighbouring modules, with reflectivity and emission losses being as little as 1.3% and 2.8%, respectively. This geometry, in its provisional stages, shows a lot of promise in terms of boasting extremely efficient translation from radiation to usable heat. However, the limitations of material temperatures and many unresolved degrees of freedom exist in the design, and will need to be determined before any industrial applications may be implemented. Notably, since only numerical studies have been performed on this design, convective losses due to wind may have a large effect of efficiency, and are yet to be quantified. This design goes a long way in demonstrating the power of utilising the view factor to “trap” heat, which increases system efficiency.

As an extension to this idea, the Spiky Central Receiver Air Pre-heater (SCRAP) receiver (see Figure 2.5) consists of a large array of spikes that project radially outward from the receiver's centre (Lubkoll, 2017). Similar to the spiky receiver geometry described by Garbrecht et al. (2013), each spike consists of two concentric tubes that force air past the outer surface of the spike where it is exposed to the collected solar heat flux.

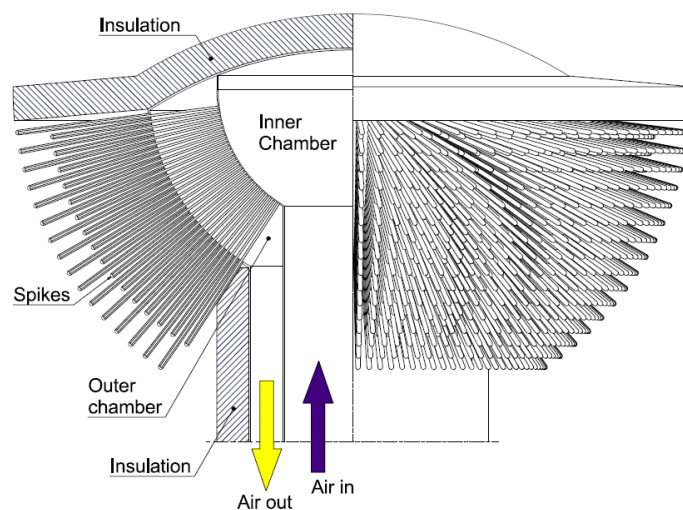


Figure 2.5: Conceptual SCRAP receiver (Lubkoll, 2017)

Numerical simulations revealed that this receiver could achieve an efficiency of 80%. However, due to its large, exposed surface area, it is susceptible to convective heat loss from these surfaces. Before implementation, it is recommended that better prediction and mitigation of convective heat loss is investigated, thereby increasing the heat transfer to the working fluid (Lubkoll, 2017).

### Cavity receivers

As the name implies, a cavity receiver consists of a cavity towards which irradiation is concentrated. Similar to closed-loop volumetric receivers, this irradiation passes through the opening of the cavity, which is known as the aperture, and is absorbed by surfaces within. This energy is transferred to an HTF that is passed through a piping network in the cavity.

In early theoretical models, it was shown that these types of receivers can achieve up to approximately 70% efficiencies when operated in a temperature range of 550 °C to 900 °C (Harris and Lenz, 1985).

More recent experimental and numerical models have achieved HTF outlet temperatures of over 1 000 °C by making use of more complex geometries, secondary concentrators and a variation of operating conditions, an example of which can be seen in Figure 2.6 (Behar et al., 2013, Kribus et al., 1999, Segal and Epstein, 2003). This receiver, a combination of the DIAPR receiver, uses compressed air as the working fluid. Four pre-heaters, including secondary concentrators, and the main, high-temperature, heating stage make up the full cavity receiver. This setup was used as a method of minimising thermal losses and was able to achieve outlet temperatures of up to 1 000 °C.

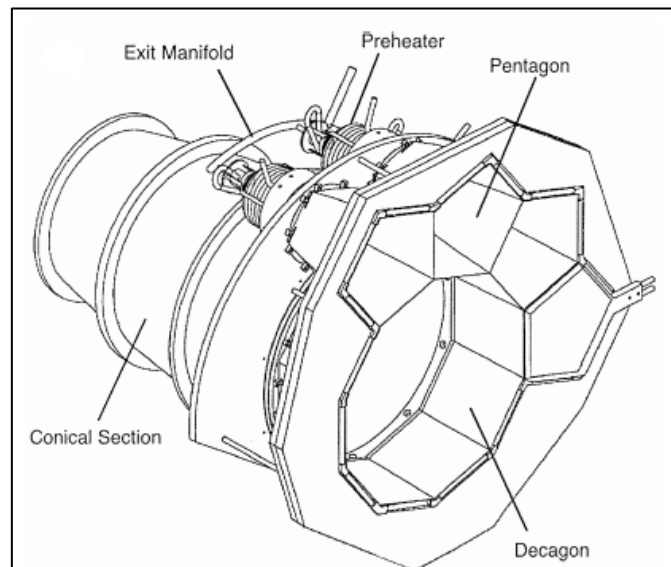


Figure 2.6: Multistage solar receiver (Kribus et al., 1999)

As mentioned previously, cavity receivers can also be made up of tubular walls, much like the open receivers, but which are surrounded by insulation, and have some sort of aperture through which concentrated sunlight can be passed. By inclusion of the insulation, the losses due to convection and re-radiation are decreased, which increases the system thermal efficiency. Two similar, well-known projects that use high-pressure air as the working fluid, are the Solar-hybrid power and cogeneration plants (SOLHYCO) project (Jedamski et al., 2010), and the Solugas project (see Figure 2.7) (Korzynietz et al., 2016).

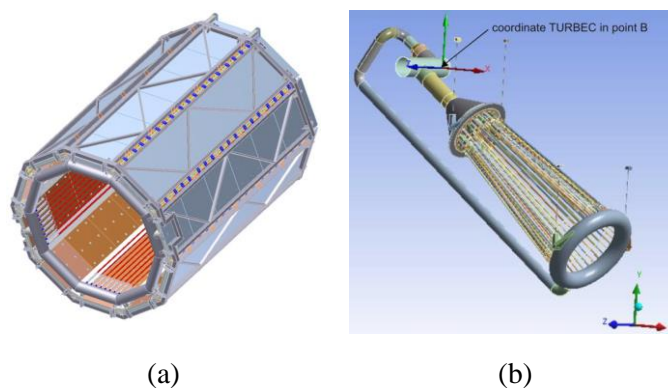
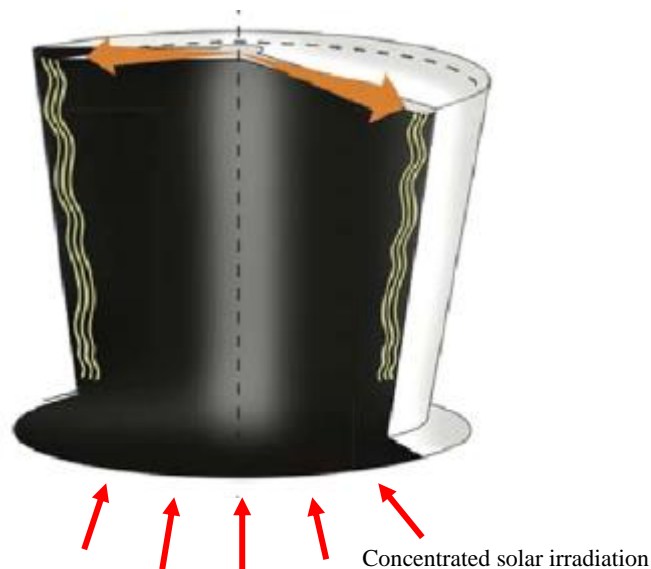


Figure 2.7: Tubular cavity receivers for (a): the Solugas project (Korzynietz et al., 2016); and (b): the SOLHYCO project (Jedamski et al., 2010)

These receivers are used to solarise a gas turbine, with the Solugas project being the first of its kind to achieve this on a large scale. These receivers are proven to achieve efficiencies of 70% to 80%, depending on solar load. Although these efficiencies are lower than those of other types of receivers, the temperatures and pressures that are achieved make them attractive for use in certain cycles, such as the Brayton cycle.

Not limited to cavity receiver, the falling film receiver, which aims to minimise thermal resistance by excluding an additional layer in the form of a pipe for fluid transport, uses a molten salt as an HTF, which is pumped to the top of a receiver and then flows down an inclined surface. The salt can be either directly radiated or indirectly heated through a wall. Early tests on these types of receivers have shown output temperatures in the range of 600 °C, with convective and radiation heat losses estimated at less than 5%. As promising as this technology seems, research is still required to find the optimum film thickness to opacity ratio. Films are also affected by windy conditions, which further complicates the eventual implementation attempt (Ho and Iverson, 2014).



*Figure 2.8: Direct exposure internal falling film receiver for use in surrounding field CST applications (Ho and Iverson, 2014)*

A more recently developed cavity receiver, depicted in Figure 2.9, which consists of an axisymmetric helical tube, is considered as a potential test case (Pye et al., 2015). This receiver, as developed, is currently integrated into parabolic dish concentrators. The intention is for the production of steam directly to drive energy generation on this commercial scale.



*Figure 2.9: Tubular cavity receiver for direct steam generation on a dish concentrator (Pye et al., 2015)*

A number of numerical methods were used in the provisional analysis and optimisation of this receiver, including ray tracing for optical simulations and custom-made codes for thermal analysis. After a large amount of geometry variations were run, results showed that a maximum overall efficiency of  $> 98\%$  could be achieved by optimisation. The optimisation of this cavity under the set parameter revealed the advantage given of using a preheating section at the aperture of the cavity, as well as the cavity shaped to taper outwards and then inwards again. These geometric changes contribute to the lowering of thermal and re-radiation losses, and increase in both outlet temperatures and optical efficiency. Although only used in parabolic dish concentrators at the moment, with the geometry being able to theoretically achieve such high efficiencies, this design is attractive for adaptation into a heliostat field, which can provide a much greater solar concentration input.

### **2.2.2 Suggested concept**

Reviewing the numerous options available for solar receivers, and considering the substantial drive towards receiver development for use in CST applications, this course is attractive for further exploration into the improvement of receiver geometry to increase system efficiencies by decreasing thermal and optical losses, and minimising thermal stress.

Presently, the open tubular receiver is most commonly used on an industrial scale. This type of receiver also currently boasts the highest proven efficiency levels for CSP receivers. However, these receivers can be largely influenced by environmental conditions that cause large thermal losses due to forced convection and re-radiation. To minimise these losses, and in an attempt to increase the thermal efficiency of these receivers, the enclosed or cavity receiver, is proposed as a solution to negate these losses.

Cavity receivers provide a large array of absorber options, which are determined by an array of factors, such as power cycle application, operating temperatures, working fluids and storage capacity. Research into particle receivers has indicated that the technology has the theoretical potential to achieve high efficiencies and operating temperatures. However, there are still many unsolved problems with particle receivers that will need to be solved before these receivers will be seriously considered for large-scale applications.

Tubular cavity receivers provide a large research base, with proven technology being globally implemented in CSP applications, with high possible efficiencies and outlet temperatures. With the versatility of a tubular receiver, it is possible to select from a range of working fluids. This choice will primarily depend on the power cycle of which the receiver will be a part.

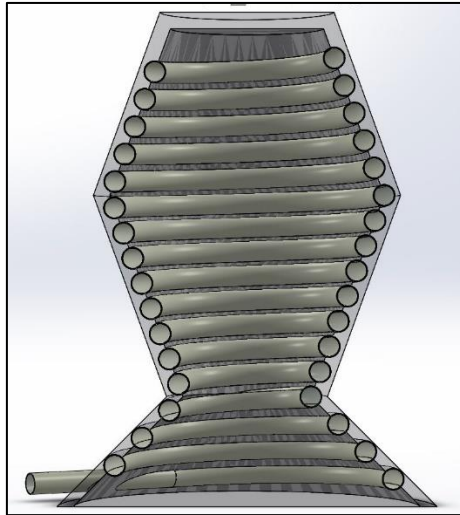


*Figure 2.10: Suggested tubular cavity receiver concept*

The suggested concept for this dissertation (see Figure 2.10), therefore attempts to incorporate these promising geometric aspects to investigate further improvements. Based on the geometry suggested by Pye et al. (2015), this design incorporated a helical tube absorber that will transport a working fluid through the geometry and gradually heat it as it passes through the domain. This tube is shaped in such a way that the multiple tapered helixes attempt to “trap” irradiation, which minimises re-radiation losses. This is all enclosed in an insulating body that further traps energy and protects the hot surfaces from additional convective heat losses.

Additional aspects can be added to the design to investigate the effect of having a preheating section, or inclusion of a quartz glass window at the aperture, which promotes the “greenhouse” effect.

### **2.3 Conjugate heat transfer**

Solar cavity receivers experience all forms of heat transfer mechanisms. Since the performance of a solar receiver is governed by its ability to capture concentrated incident radiation, and subsequently transfer this thermal energy to the flow of HTF, it is important to fully understand these mechanisms in order to manipulate the receivers, materials, geometries, flow rates and coatings to optimise the performance of the solar receiver.

In the case of point-focus concentrated solar collectors, the following heat transfer areas that use a candidate receiver type developed in this study are considered, in Figure 2.11:

- Internal forced convection to HTF
- External convective heat losses
- Internal and external radiation, absorption or reflection and re-radiation effects

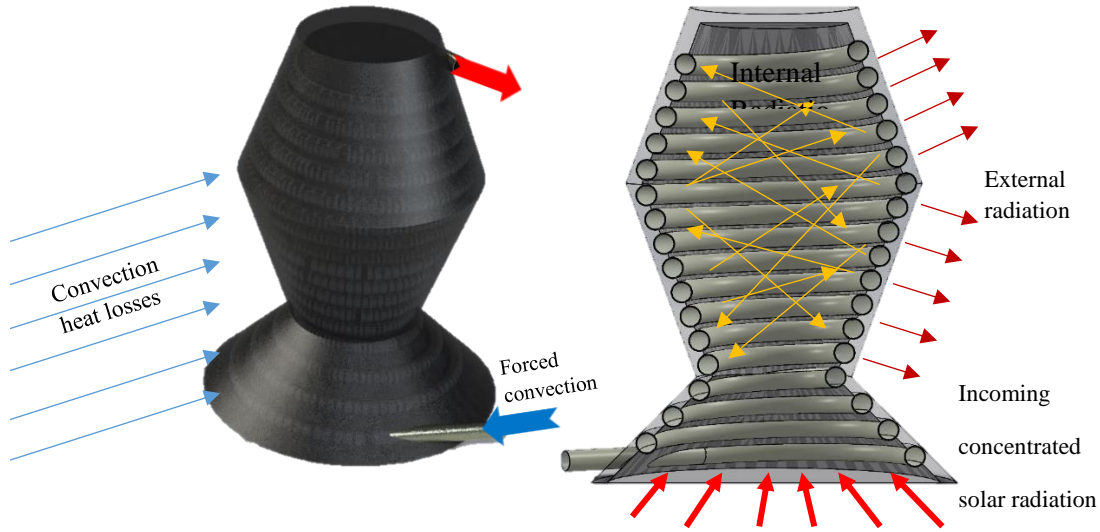


Figure 2.11: Conjugate heat transfer for the conceptual tubular cavity receiver

The physics of transferring heat are well known and thoroughly documented, particularly in terms of the analytical methods that are used in solving heat transfer problems. The application of these laws to a discretised domain and their application to point-focus systems in particular should be well understood to ensure an accurate representation of the physics in the computational environment. In point-focus systems, all three mechanisms can affect the outcome of the solution.

### 2.3.1 Internal forced convection to HTF

A critical aspect to consider in all solar receivers is the transfer of absorbed heat flux to the HTF for use in power generation. In tubular systems, if heat flux is uniformly distributed over the outside surface of the tube, given by  $\dot{Q}_{conv}$  in Figure 2.12(a), the heat transfer to the fluid can be calculated with Newton's Law of Cooling:

$$\dot{Q}_{conv} = hA_{tube,i}(T_e - T_i), \quad 2.1$$

with  $T_i$  and  $T_e$  being the inlet and outlet temperatures respectively,  $A_{tube,i}$  is the surface area of the inside surface of the tube. The heat transfer coefficient ( $h$ ) is derived using the Nusselt number of the inner wall,  $Nu_{wall}$ , as:

$$h = \frac{k_{HTF}Nu_{wall}}{d_i} \quad 2.2$$

At this point, it should be noted that heat flux in solar receivers and, in particular, on the surface absorber tubes is rarely uniformly distributed, as seen in Figure 2.12(b). Methods to analytically account for this non-uniformity have been proposed to account for variations in heat flux on a boundary. However, these methods fall outside the scope of this dissertation. Using FVMs to solve the partial differential equations, a single dimensional example, as shown in Figure 2.12, which can be expanded to the three-dimensional equivalent, can be used to solve the differential equation.

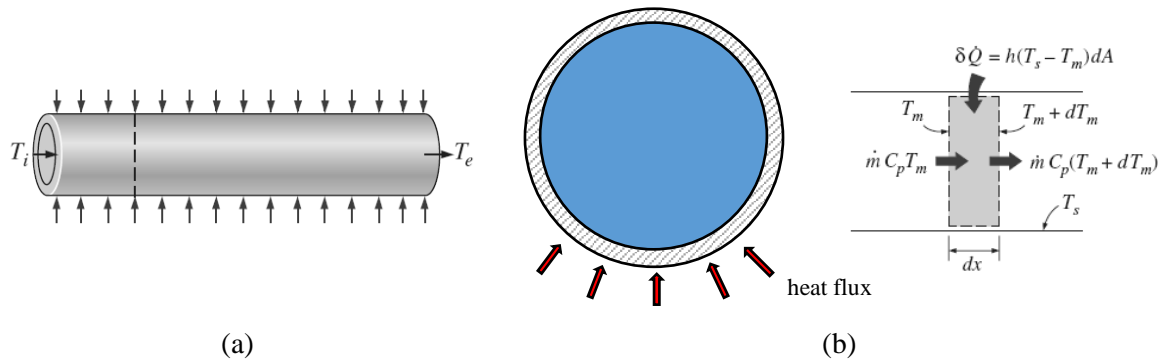


Figure 2.12: (a) Internal forced convection for cylinder (Cengel and Ghajar, 2011); and (b) applied non-uniform heat flux solution using a differential control volume

Additionally, using methods to increase the heat transfer to the working fluid, increasing the turbulence of the flow will proportionally increase the Nusselt number, therefore also the heat transfer coefficient, as deduced from Equation 2.2. These methods are numerous, and some are more application specific. They include the use of irregular inside surfaces of piping, such as introducing dimples (Chen et al., 2001) (see Figure 2.13), or a spiral (Jedamski et al., 2010) along the length. The pathways that tubes follow can also naturally contribute to turbulent or chaotic flows, such as using coiled tubing.

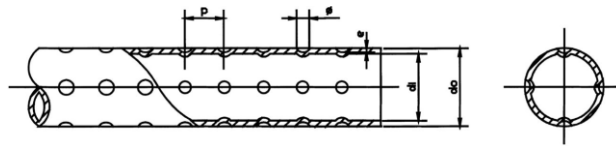


Figure 2.13: Geometry of axisymmetric dimpled tube (Chen et al., 2001)

### 2.3.2 Convective heat losses

Due to the usually high temperatures in the solar receiver system, the cavity is subject to heat losses to the environment, which will significantly influence its performance and overall system efficiency. Convective losses can be made up of forced and natural aspects, depending on material properties, environmental conditions and geometry, for instance.

Cavities lose heat to the environment via external forced convection. Natural convection is the most complex heat transfer mechanism to account for most cavity receivers, when attempted to solve for it analytically or using CFD. This is because the flow domains generally have to be far greater than the size of the receiver. As a simplification, the surface heat transfer coefficients and ambient temperatures on the outer surfaces can be specified. These values are based on other studies that have been performed on materials and known environmental conditions at the site of installation respectively. These values should allow reasonable approximations to be made, especially initial design approximations. Since the heat transfer coefficient depends on many factors, such as cavity height above the ground, cavity surface area and wind speed, the external heat transfer coefficient is estimated to be  $15 \text{ W/m}^2\text{K}$  as a simplification based on the work of Fang et al. (2011), who extensively studied the thermal performance of cavity receivers in windy conditions.

Case studies, which simulate the effect of natural convective heat loss, have demonstrated numerous aspects that contribute to these losses using both experimental and numerical studies. Open cavity receivers are particularly susceptible to natural convective heat loss.

Numerical simulations appear to predict convective losses well, as they show good correlation to experimental work (Li et al., 2015). In these tests, Li et al. (2015) prove the correlation between convective heat loss, with aperture size and position, and cavity angle (Figure 2.14). It is evident from these numerical tests that convective heat loss can be as much as 30% under certain conditions.

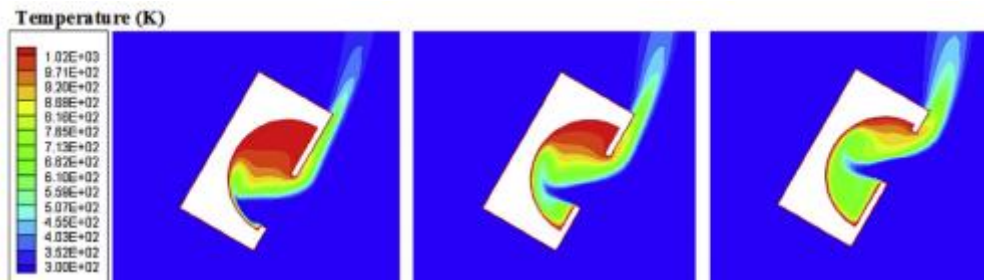


Figure 2.14: Convective heat loss from example cavity at 30° inclination angle with variable size of aperture (Li et al., 2015)

### 2.3.3 Internal and external radiation and re-radiation effects

Radiative heat transfer occurs in all directions from bodies that have a temperature above absolute zero. This heat transfer occurs by means of electromagnetic waves. Thermal radiation occurs at a wavelength between ultraviolet (UV) and infrared (IR) ( $\lambda = 10^{-1}$  to  $\lambda = 10^2 \mu\text{m}$ ) (see Figure 2.15(a)).

A blackbody is an ideal body comprising a surface that is the perfect absorber and emitter of electromagnetic waves. This blackbody absorbs all incident radiation and emits all radiation perfectly diffusively (Figure 2.15(b)). Therefore, it is used as a standard to which real surfaces can be compared.

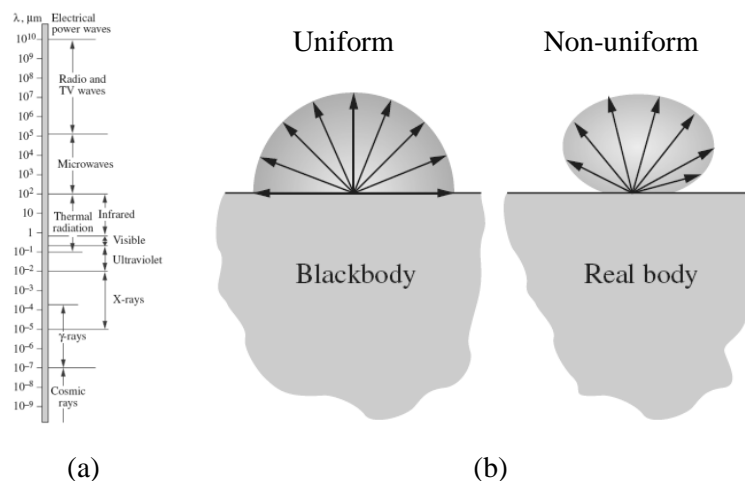


Figure 2.15(a): The electromagnetic spectrum; and (b): diffusivity of a blackbody and real surface (Cengel and Ghajar, 2011)

Furthermore, surfaces that do not perform ideally – known as real surfaces – are specifically analysed and statistically averaged. They are collectively known as grey surfaces. These surfaces typically have

an average emissivity value that is lower than that of a blackbody, and cannot achieve perfect diffusivity, as shown in Figure 2.16 and Figure 2.15(b) respectively.

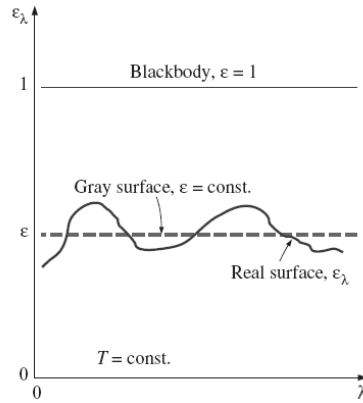


Figure 2.16: Comparison between blackbody, grey surface and real surface emissivity (Cengel and Ghajar, 2011)

Once this incoming electromagnetic wave, known as incident radiation or irradiation, reaches the surface of a body, a certain percentage is absorbed, reflected or transmitted, depending on the properties of the intersected body. The fractions of the aforementioned interactions depend on the absorptivity ( $\alpha$ ), reflectivity ( $\rho$ ) and, if the body is semi-transparent, the transmissivity ( $\tau$ ). This interaction is governed by Equation 2.3.

$$\alpha + \tau + \rho = 1 \quad 2.3$$

The transmission of radiation between two bodies also depends on a view factor. View factors are ratios based on how much of a receiving surface is “visible” from an emitting surface, as the transferring of electromagnetic waves depends on “line-of-sight”. In solar cavity receivers, view factors are utilised to enable the maximisation of absorbed incident radiation, and the decrease of re-radiation from the cavity surfaces.

Certain materials and coatings that can maximise the cavity receiver’s efficiency with the principles discussed in this section have been proposed. The most commonly used methods are the following:

- Increasing the absorptivity of an absorber tube, such as the high-temperature paint, Pyromark 2500.
- Increasing the reflectivity of a cavity’s insulating walls by making use of thin mirrors or polymer films
- Optical coatings that selectively reflect certain wavelengths of electromagnetic waves

These methods are discussed in further detail in numerous case studies in this dissertation.

## 2.4 Determining the performance of solar collectors

A solar collector system’s performance can be quantified as the system’s ability to transfer energy between sources as effectively as possible. In these systems, performance can be separated into optical efficiency and thermal efficiency, with the overall system efficiency being a product of these values,

including conversion ratios between collected energy to electricity production. This, however, falls outside the scope of this research.

### 2.4.1 Optical efficiency

As the first part of the process of collecting solar energy, optical efficiency is determined by the amount of energy available from the sun, compared to how much energy is eventually passed to a solar collector. The optical efficiency can be influenced by a collection of variables. Material as well as environmental factors can have an impact on the final heat value. In all solar systems, the overall principle in determining the optical efficiency is the same. More specifically, in the case of point-focus systems, the optical efficiency is most easily quantified as follows:

CSP towers:

$$\eta_{CSP,op} = \frac{A_{ap} \int \dot{q}_{rad}}{DNI \times \sum A_{heliostats}} \quad 2.4$$

Parabolic dish:

$$\eta_{Dish,op} = \frac{A_p \int \dot{q}_{rad}}{DNI \times A_{dish,proj}} \quad 2.5$$

Factors that negatively affect the amount of irradiation that could be received by the solar cavity depend on material properties, as well as potential environmental conditions. Real reflective surfaces cannot perfectly reflect the incoming solar ray towards the target. Not only is the surface subject to absorbing a partial amount of energy from this ray, the ray path may also be affected by surface microscopic properties and unevenness, causing the reflection to have a slight diffuse nature. The reflectivity may also be decreased by the fouling of the reflective surface or settling of dust or other environmental elements on the surface. This dust reduces the effective reflective area of the mirror, while it also decreases its maximum specularity. It is also possible that the dust may absorb more of the irradiation than the mirror would on its own, causing the abnormal heating of the mirror surface. It is apparent that, to maximise the system's optical efficiency, the mirrors need to be cleaned regularly.

Fortunately, numerical methods can consider this scattering effect, as will be discussed in further detail in section 2.6.

### 2.4.2 Thermal efficiency

Once energy has been collected and concentrated, it is necessary to convert this sun energy into usable heat energy. This conversion process uses the energy collected by the optical portion of the system. Since point-focus systems use a heat transfer fluid for the heat transfer of energy, the thermal efficiency can be calculated by the ratio of energy absorbed and the energy available.

A well-known efficiency ratio for this system is expressed in Equation 2.6, which is considered accurate in most applications. However, since the  $C_p$  value of a material is a function of temperature, this value

can become inaccurate, especially considering the large temperature differences this fluid experiences in a point-focus solar receiver.

$$\eta_{ther} = \frac{\dot{m}C_p(T_e - T_i)}{\dot{q}_{rad}A_{aper}} \quad 2.6$$

A suggested improvement to this calculation is given in Equation 2.7, which rather uses the difference in the energy of the fluid between the inlet and the outlet.

$$\eta_{ther} = \frac{\Delta Q_{HTF}}{Q_{rad,ab}} \quad 2.7$$

### 2.4.3 Overall efficiency

Plant efficiency is the quantification of the overall performance of the solar plant, from solar collection to electricity production. Once the energy has been translated to the HTF, the conversion of this energy into electricity is associated with conversion losses outside the scope of this study. The total or overall efficiency for the scope of this dissertation is therefore defined as the product of optical and thermal efficiencies (see Equation 2.8).

$$\eta_{overall} = \frac{\Delta Q_{HTF}}{DNI \times A_{refl}} \quad 2.8$$

### 2.4.4 Efficiency calculation using FVM

Analytically, it is often challenging to acquire some of the values that make up the quantification of efficiency, and may need to be estimated for experimental cases. However, the FVM makes it possible to extract this information from surfaces and volumes in the domain and more accurately analyse the system's performance. If flow information is not available, it has also been shown that the simplified version of an efficiency calculation, due to the capabilities of the FVM method, can be given as follows:

$$\eta_{thermal} = \frac{Q_{in} - Q_{losses}}{Q_{in}} \text{ and } Q_{HTF} = Q_{abs} - Q_{losses}, \quad 2.9$$

where  $Q_{in}$  is the amount of heat made available for use at the receiver aperture surface;  $Q_{abs}$  is the absorbed heat and  $Q_{losses}$  is the summation of any thermal losses that may occur in the system, such as re-radiation through the cavity window and convective heat loss from the external insulation surface.

### 2.4.5 Efficiency calculation using MCRT

As indicated in section 2.4.4, numerical methods provide tools for the determination of data on interfaces and surfaces in the computational domain. Using MCRT, it is possible to determine optical efficiency by calculating the number of rays that intersect a surface. Since a ray has a certain constant power associated with it, the sum of the rays intersecting the surface multiplied by the power per ray will yield the same result as calculated absorbed and reflected heat flux on a surface. When only absorbed heat flux is of interest, only final ray intersections should be considered. Using this method, Equation 2.10 can perform the calculation of optical efficiency.

$$\eta_{opt} = \frac{rays_{in} - rays_{lost}}{rays_{in}} \quad 2.10$$

## 2.5 Finite volume method

The FVM is a procedure for the evaluation of partial differential equations, at discrete positions in space. In the fluid mechanics application, the positions in space are specified by a meshed geometry, with the partial differential equations being based on a number of physical conservation principles.

### 2.5.1 Governing equations

Conservation principles in fluid mechanics are more commonly known as the governing equations. These equations ensure the conservation of the following:

1. Mass (continuity)

$$\frac{\delta \rho}{\delta t} = \nabla \cdot (\rho \vec{v}) = S_m \quad 2.11$$

2. Momentum

$$\frac{\delta}{\delta t} (\rho \vec{v}) + \nabla \cdot (\rho \vec{v} \vec{v}) = -\nabla p + \nabla \cdot \bar{\tau} + \rho \vec{g} + \vec{F} \quad 2.12$$

3. Energy

$$\frac{\delta E}{\delta t} + \nabla \cdot (\vec{v}(\delta E + p)) = \nabla \cdot \left( k \nabla T - \sum_j h_j \vec{J}_j + (\bar{\tau}_{eff} \cdot \vec{v}) \right) + S_h \quad 2.13$$

Notably,  $S_h$  is the term, with units  $\frac{W}{m^3}$ , which represents the volumetric heat source that may be defined in the domain. A large number of settings may be modified to allow for the satisfaction of the conditions that the discretised domain experiences. With these settings, it is possible to account for laminar or turbulent flow, different inlet and outlet conditions and setting initial starting conditions in the solution.

Since each case requires various settings for convergence to be achieved, the solution-specific requirements are discussed in the case studies following this chapter.

### 2.5.2 Determining convergence

In numerical analysis, data can be analysed with the FVM to determine whether a solution has reached steady state, in numerical or graphic form, to determine whether the critical values that are selected stop changing or “level out”.

Generally, this convergence is monitored by scaled residual values. The residual value is based on the imbalance of the general conservation equation for a specific cell P given by Equation 2.14.

$$a_p \phi_p = \sum_{nb} a_{nb} \phi_{nb} + b, \quad 2.14$$

where  $a_p$  is the centre coefficient,  $a_{nb}$  considers the influence for adjacent cells and  $b$  includes the constant parts of the source terms. Using Equation 2.14, the scaled residual value gives a much clearer indication as to the convergence of the domain, when one considers that all governing equations that

are being solved can be calculated. This scaled residual value, which is calculated with Equation 2.15 for the pressure-based solver, is calculated with a manipulated version of Equation 2.14 to calculate an average for all the cells in the domain.

$$R\phi = \frac{\sum_{cells,p} |\sum_{nb} a_{nb}\phi_{nb} + b - a_p\phi_p|}{\sum_{cells,p} |a_p\phi_p|} \quad 2.15$$

It should, however, be noted that residuals appear to have the characteristic “levelling out” in many cases, which can often be mistaken for conversion, even though a final steady-state solution has not been reached. As a solution to this, various output parameters, such as heat losses from a surface, outlet temperatures and pressure, should be created and graphed in ANSYS Fluent. The simulation should only be deemed as converged when these values have reached a steady-state value.

### 2.5.3 Solving of the radiative transfer equation

If enabled, the energy equation (Equation 2.13) includes a source term for also considering the effects of radiation. The radiation element of the energy equation, which is known as the RTE, is solved by the resolution of the partial differential equation, namely Equation 2.16 (Versteeg and Malalasekera, 2007).

$$\nabla \cdot (I_\lambda(\vec{r} \cdot \vec{s})\vec{s}) + \beta_\lambda I_\lambda(\vec{r} \cdot \vec{s}) = \alpha_\lambda n^2 I_{b\lambda} + \frac{\sigma_{s\lambda}}{4\pi} \int_0^{4\pi} I_\lambda(\vec{r} \cdot \vec{s}') \Phi(\vec{s} \cdot \vec{s}') d\omega', \quad 2.16$$

where a beam of radiative intensity is given by the  $I_\lambda(\vec{r}, \vec{s})$  variable, which is a function of the spectral variable ( $\lambda$ ), position in the domain ( $\vec{r}$ ) and directional vector ( $\vec{s}$ ). This beam moves through the medium that has absorbing, scattering and emission properties. Furthermore, the radiative heat flux for a non-grey medium is given by Equation 2.17.

$$q(\mathbf{r}) = \int_0^\infty \int_0^{4\pi} I_\lambda(\vec{r}, \vec{s}) \vec{s} d\omega' d\lambda \quad 2.17$$

The double integration of the RTE equation, over all solid angles and wavelengths, yields the divergence of heat flux as follows:

$$\nabla \cdot q = \int_0^\infty \alpha_\lambda \left( 4\pi I_{b\lambda} - \int_0^{4\pi} I_\lambda(\vec{s}') d\omega' \right) d\lambda \quad 2.18$$

Beam energy decreases due to the surrounding cells' absorption and scattering effects, which are known as out-scattering, and increases due to surrounding cell emission (re-radiation) and scattering towards the discretised cell, known as in-scattering.

The radiative heat flux is solved in Fluent using the  $S_2$  method, which is a subset of the discrete ordinates (DO) method that uses the  $S_N$  approach, with  $N$  being the number of ordinate directions. Each element that is in a cell zone activated for the solving of the RTE is discretised further into angular space, with  $N_\theta \times N_\phi$  control angles, each of which are also subsequently divided into pixels (see Figure 2.17). The number of RTE equations for each aforementioned element is calculated, depending on the

dimensionality of the domain as  $2 \times N_\theta \times N_\phi$ ,  $4 \times N_\theta \times N_\phi$ ,  $8 \times N_\theta \times N_\phi$  for one-dimensional (1D), two-dimensional (2D) and three-dimensional (3D) domains respectively. The implication of the increased RTE equations to solve both increases the requirement of processing power and memory requirements that are necessary to compute the solution.

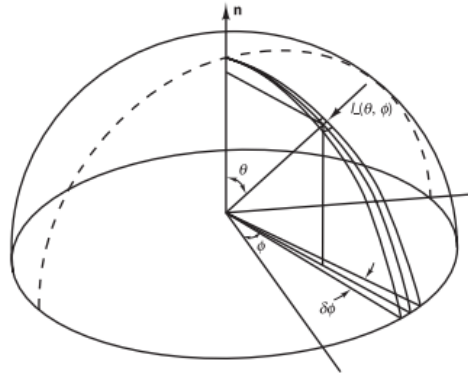


Figure 2.17: Angular discretisation of discrete ordinates method (Versteeg and Malalasekera, 2007)

Due to the discrete nature of the finite volume domain, the implementation of the radiative heat transfer model is susceptible to errors, such as false scattering (numerical diffusion) and ray effects (Versteeg and Malalasekera, 2007). The consequence of these errors is the spreading of propagated beams of radiation energy and the incorrect prediction of the direction of the wave front. Methods to minimise these errors can include increasing the mesh size, angular discretisation and the spatial discretisation of the discrete ordinates model.

## 2.6 Monte Carlo ray tracing

Ray tracing, as it is known, can have many applications. In this instance, ray tracing involves the tracing of a vector through space, analytically calculating its direction based on interactions with surfaces that it intercepts until these interactions are absorbed or lost. By analysing a large quantity of these paths, it is possible to produce a result that quantifies the interaction of surfaces with these produced rays. By applying statistical methods, in this case, the Monte Carlo method (Binder, 1987), random rays can be generated from an emitting surface, and can replicate the interaction of sunlight with a surface. This interaction includes optical and geometrical aspects such as surface absorptivity, diffusivity, transmissivity and a large variety of other possible factors.

A large variety of open-source and commercial software codes is available for ray tracing. For this application, SolTrace, a free software package, (Wendelin et al., 2013) was selected as the means of producing ray-tracing results. It can produce heat flux maps, replicate the sun's intensity and shape, and it has scriptable functions. Its computational cost is also relatively low, while it offers a high degree of accuracy. A SolTrace project that replicates the PS10 heliostat field in Spain demonstrates the possibility of reproducing large systems using this method with very low computational power requirements (see Figure 2.18).

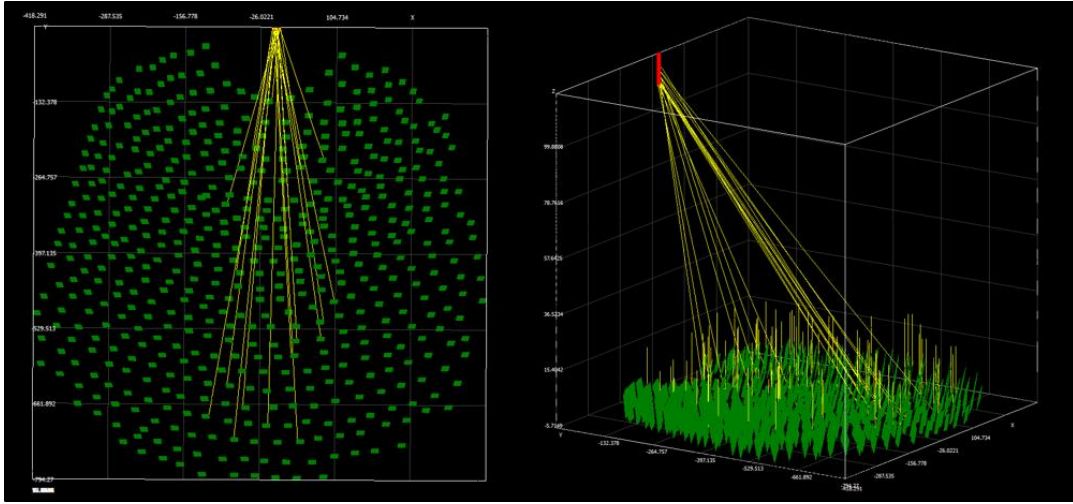


Figure 2.18: Replication of PS10 field in SolTrace

For the definition of elements in the SolTrace environment, the element's position relative to the stage coordinate system, as well as the face normal direction, should be known. The following equations, with variables that relate to those in Figure 2.19, are used to define the element's position in space as well as its aim point:

$$\hat{s} = \langle s_x, s_y, s_z \rangle$$

$$P_1 = (x_1, y_1, z_1)$$

$$P_2 = (x_2, y_2, z_2)$$

$$\hat{t} = \frac{P_1 P_2}{|P_1 P_2|} \quad (2.19)$$

$$\hat{n} = \frac{\hat{t} + \hat{s}}{\sqrt{2(1 + \hat{s} \cdot \hat{t})}} \quad (2.20)$$

$$\hat{A} = P_1 + C \times \hat{n} \quad (2.21)$$

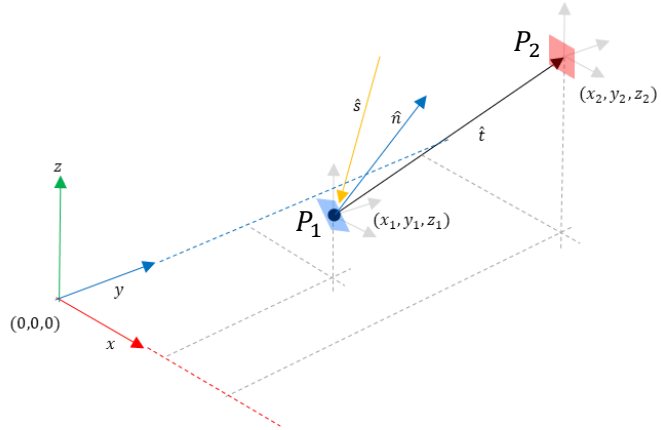


Figure 2.19: Definition of an element in SolTrace

where  $\hat{s}$  is the solar vector,  $\hat{n}$  is the normal unit vector, and  $\hat{t}$  is the target vector determined from  $P_1$  to  $P_2$ .

One shortfall of SolTrace is the limited availability of definable surface and aperture types in its own library. Its inability to replicate complex geometries that may form part of a study such as this limited the easy replication of systems that were under consideration.

Every element, once fully defined in the domain, requires an optical property assigned to its surface. SolTrace can represent reflective or refractive surfaces, or a combination of interactions with rays that intersect the surface. The optical property set also allows SolTrace to consider surface macroscopic and microscopic properties. This ray interaction with the surface will determine how specular the ray interaction with the surface will be. The angle of reflection is calculated in two stages using Monte

Carlo prediction strategies, based on Gaussian, pillbox or customised distributions. Initially, SolTrace will calculate the reflection angle due to the macroscopic properties of the surface (see Figure 2.20(a)). This reflection angle is then further distinguished, with the calculation of the angle being based on the microscopic properties of the surface, as shown in Figure 2.20(b), at which point the ray unit vector has been defined.

With this method, the fouling of mirrors or other reflective surfaces can also be considered, as discussed in section 2.4.1.

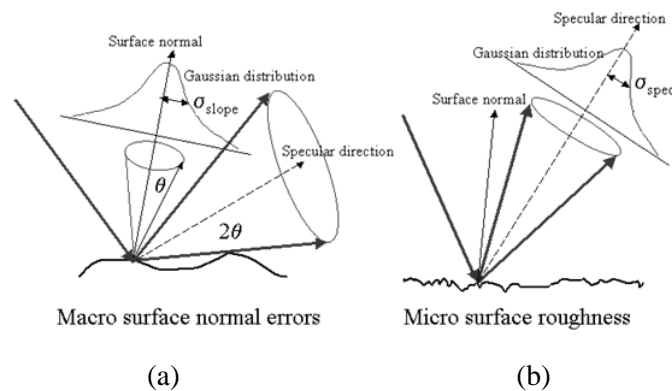


Figure 2.20: Probabilistic outcomes of ray interactions with SolTrace Surfaces  
(Wendelin et al., 2013)

Much like the FVM, ray tracing requires a convergence study of each simulation to ensure that a steady solution state can be reached. This would require the generation of a minimum number of rays, as well as specified ray-surface interactions until the heat flux values on surfaces of interest stabilise. SolTrace is limited as to how many rays can be solved for in a single simulation. However, this can be overcome by performing multiple simulations with different random numbered seeds. These generated results are concatenated together to provide a solution based on a simulation using a much larger sample set of generated rays. This procedure is explained further in section 5.3.6.

## 2.7 Numerical estimation of solar loads

Multiple case studies that have been performed in solar receiver simulations have required solar load estimations of some description to produce accurate, relevant results. The National Renewable Energy Laboratory (NREL) identified the need for optical tools, and developed such tools in the early 1990s to analyse and optimise anything from single-facet systems, such as dish concentrators, to multi-faceted systems, such as heliostat fields (Jorgensen, 1991). Many case studies and projects, including several SUNSPOT and SUNDISC collector studies (S.T.E.R.G., 2017), the SOLHYCO project and the REFOS cavity receiver have all used the numerically acquired heat flux distributions with great success. These predictions have been acquired experimentally and numerically with ray tracing to gain an understanding of the systems' optical properties and thermal capabilities.

The correct estimation of heat flux distribution can have a great effect on the parameters of the collector and receiver or absorber. (Cheng et al., 2013)) have used a REFOS-SOLGATE case study to prove that the misprediction of heat flux distribution can severely affect projected results.

## 2.8 Additional considerations

### 2.8.1 Thermal stress and hot spots

In solar receiver systems, high-energy, non-uniform heat flux distributions are inevitable. It can therefore be expected that high thermal stress and deflections will be induced (Wang et al., 2010). Thermal stress is a large contributor to the high degradation rates of components in the system, since materials are subject to cracking, oxidation and erosion, which causes complications in using materials together to make their properties more suitable for use in a solar receiver. The SOLHYCO project experimented with the use of multi-layer tubes (Jedamski et al., 2010), which attempted to improve the heat distribution throughout the circumference, while maintaining corrosive resistance, among other properties. Although this principle worked as expected, different degrees of thermal expansion between the layers began to degrade the interface between layers after a number of cycles (see Figure 2.21).

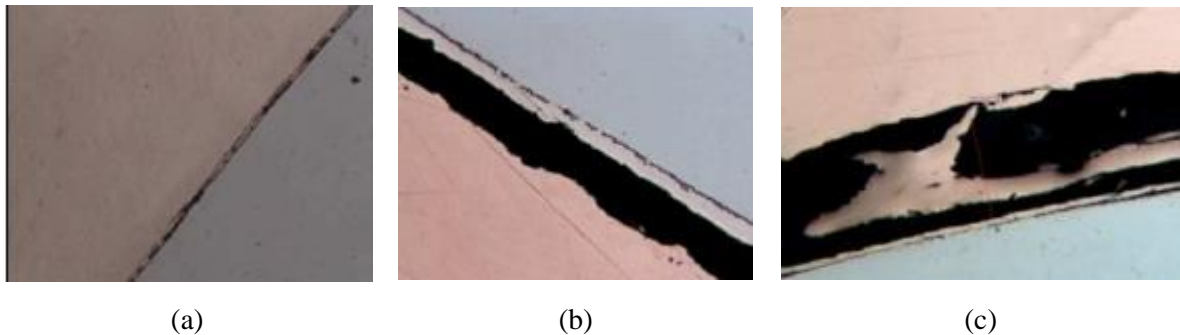


Figure 2.21: The magnified condition of multi-layer tube interface, after (a): 0; (b): 50; and (c): 500 cycles (Buck et al., 2001)

It is therefore a critical consideration for solar receivers to minimise temperature differences throughout the geometry, to reduce maintenance requirements and keep components and coatings performing as efficiently as when first installed.

### 2.8.2 Coatings

As briefly discussed in section 2.3.3, a coating can be used to make the optical properties of a surface more favourable for their application, raising system efficiencies by maximising absorbed radiation on desired surfaces, and minimising re-radiation losses. Coatings are commonly applied to absorber tubes, insulating walls and glass windows in a cavity receiver. This has been done with reasonable success in the past. The SOLHYCO project was one of the projects that applied a coating, known as Pyromark 2500, to its absorber tubes (Ho et al., 2012). This coating increased the absorptivity of the surface to  $\sim 0.95$ . This same project applied reflective coatings to the inside surface of the receiver's insulation.

Perhaps one of the more notable coating interactions is that of a semi-transparent surface that has been coated. The surface changed its interaction with a wave that was dependent on its wavelength. This made it possible to replicate what is commonly known as the “greenhouse” effect in a solar receiver cavity. The coating allowed for the transition of solar irradiation, or the visible light spectrum, to pass through with no interaction. However, it was reflective of wavelengths in the infrared part of the spectrum.

All coatings experience similar drawbacks when used in solar systems due to degradation from use at high temperatures. They crack due to differences in the thermal expansion coefficients between the

coating and base material onto which they are applied. Application is discussed in further detail in following sections of this dissertation.

### 2.8.3 Glass

The inclusion of glass in a cavity receiver design reduces heat losses in the system and increases efficiency. The addition of a glass window at the aperture of a receiver shows a notable increase in performance when considering thermal efficiencies and outlet temperatures.

Furthermore, as discussed in section 2.8.1, the “greenhouse” effect can be created in the cavity receiver with a glass aperture window. With this inclusion, certain bands of re-radiation can be reflected back towards the cavity, which decreases the total amount of energy loss through an aperture window. According to Figure 2.15(a), thermal radiation occurs predominately in the wavelength range of 0.1  $\mu\text{m}$  to 1 000  $\mu\text{m}$ . Glass window materials and coatings should be selected so that their properties reflect as much of this bandwidth as possible.

Efficiency is improved by minimising convective heat loss due to wind and buoyancy effects, as well as by reflection of re-radiation from absorber surfaces in the cavity.

However, it should be noted that the inclusion of a glass aperture vastly increases both the complexity of the system and the cost, which will need novel approaches to integrate it into the system more seamlessly.

A large amount of effort has gone into the development of this material for this application. Since the glass absorbs electromagnetic energy, it is bound to heat up, which induces stress and potential losses. Coatings have been developed and tested based on a number of sample geometries (Roger et al., 2009). Tests performed on a REFOS geometry showed a reduction in this absorption by approximately 78 K, which translates into a decrease of ~8%.

As yet, only short-term tests have been conducted on fully pressurised windows (Hofmann et al., 2009). However, the full-scale implementation of this technology has yet to be proven.

## 2.9 Conclusion

The literature study primarily dealt with previous research and case studies regarding CSP systems. It particularly focused on the available point-focus systems and receivers that will absorb this concentrated energy. The literature review highlighted the fact that many different design options, with many factors that can affect system performance, are available. The survey revealed many experimental or numerical studies that lay a strong foundation on which to proceed with further case studies. The literature study also revealed the following:

- There is a global drive towards CSP, with large developments underway for CST plants, with a need for further research into improving efficiency, materials and working fluids.
- High concentrations of energy and flux non-uniformity lead to thermal stress, inefficiencies, and the degradation of materials and coatings.
- Numerical methods that attempt to integrate MCRT and FVM have been introduced.
- More research into the more accurate prediction of heat flux and temperature peaks receivers is critical to improve overall efficiency and minimise material degradation.
- A tubular cavity receiver is a proposed concept that aims to allow for further research into the effects of geometry, heat flux distributions and materials of system efficiency.

# Chapter 3: Numerical methods

## 3.1 Preamble

This chapter discusses the investigation process, which starts with understanding the functionality of the FVM and MCRT, including the quantification of their benefits and limitations. Methodology is introduced as different case studies are presented, which offers novel numerical approaches that were used to improve simulation accuracy, as well as reduce the computational power necessary to achieve acceptable, comparable results.

## 3.2 Radiation modelling using RTE

To implement the use of the RTE equation in ANSYS Fluent, it is essential to understand the level of domain discretisation that is necessary to minimise the effect of numerical errors such as false scattering and ray effects.

### 3.2.1 Finite volume solution of RTE using discrete ordinates

A test case (Craig et al., 2016a, Moghimi et al., 2015) presents a 2D domain with a semi-transparent wall, as a specular source of radiation heat flux with perfectly absorbing walls and negligible re-radiation effects, as in Figure 3.1. This test case aims to understand the settings required to achieve specular transmission of radiation through a domain, with isotropic scattering.

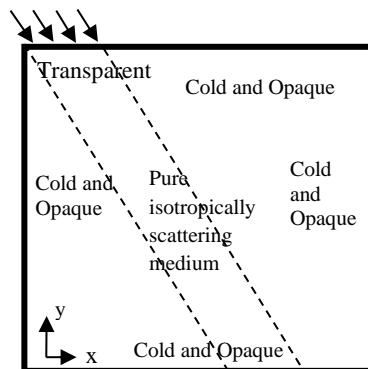


Figure 3.1: Theoretical 2D radiation test case (Moghimi et al., 2015)

In these studies (Craig et al., 2016a, Moghimi et al., 2015), a large variety of settings and discretisations are attempted, with the results compared to an equivalent, accurate MCRT simulation. This test case observes that it is necessary to improve the discretisation of the mesh and the DO angular discretisations to achieve the optimal result (see Figure 3.2), which matches the MCRT result to within a small discrepancy, when using a  $100 \times 100$  mesh and  $N_\theta \times N_\phi$  of  $3 \times 40$ .

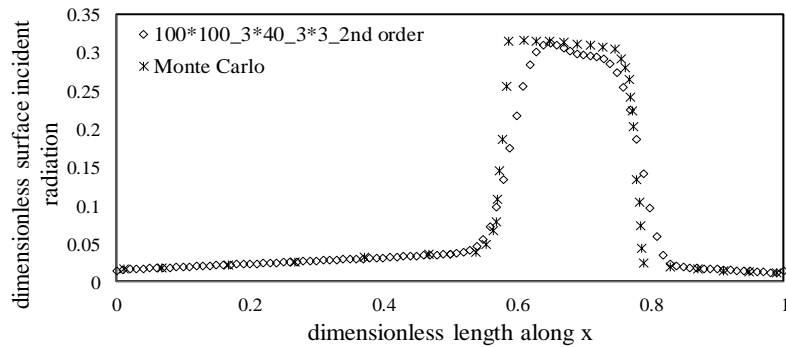


Figure 3.2: The test case result comparison with MCRT using second-order DO settings  $100 \times 100$  mesh and  $N_\theta \times N_\phi$  of  $3 \times 40$  (Moghimi et al., 2015)

### 3.2.2 Biomass cavity receiver

A test case (Martinek and Weimer, 2013) that aimed to use conclusions from the previous case, was conducted on a biomass cavity receiver (Lichty et al., 2010) (see Figure 3.3). This geometry was utilised as a means of comparison between a pure FVM to solve for incident radiation using the RTE equation and MCRT.

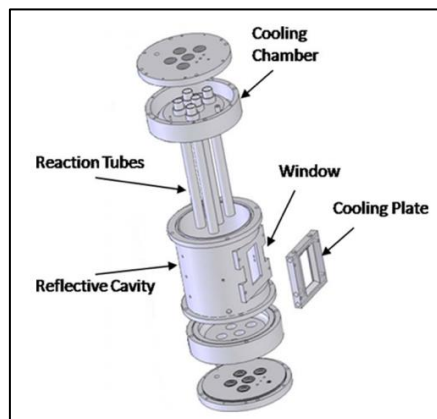


Figure 3.3: A reflective cavity multi-tube solar reactor (Lichty et al., 2010)

The geometry that was used by Martinek and Weimer (2013) in a 2D domain was replicated in the finite volume domain. Two variations of the geometry were simulated: a single-pipe (see Figure 3.4a), and a five-pipe (see Figure 3.4b) cavity receiver. The boundary condition of the cavity wall was also varied between perfectly reflecting and perfectly absorbing to highlight the limitations of the RTE equation and FVM in prediction of interactions with specular and diffuse ray interactions with the respective surfaces.

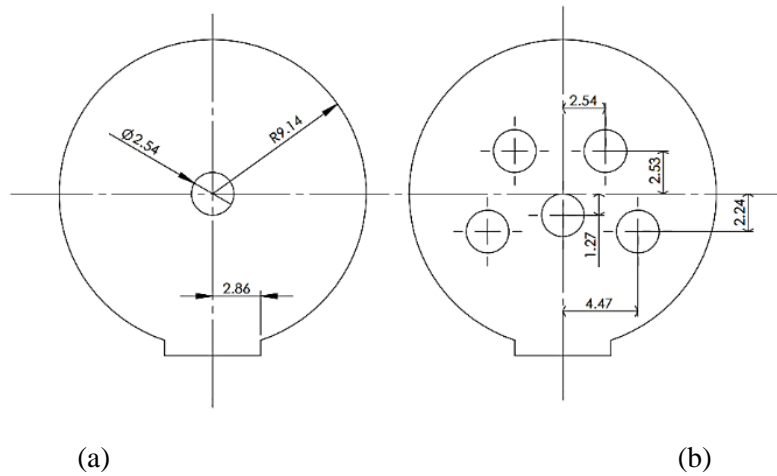


Figure 3.4: The biogas receiver configuration for: (a) one pipe; and (b): five pipes (Martinek and Weimer, 2013)

Using the conclusions drawn from the aforementioned test case in section 3.2.1, simulations were performed on these four cases. As predicted, the convergence of results depended on both the discretisation of the mesh and the angular discretisation settings when using FVM. Since MCRT is accepted as the most accurate answer, values determined with FVM were compared with these values.

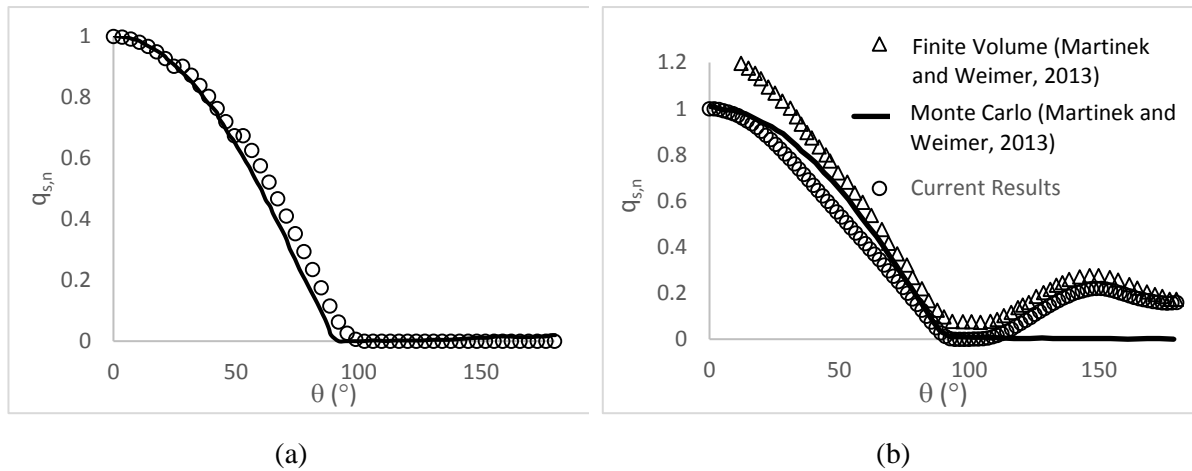


Figure 3.5: The normalised heat flux  $q_{s,n}$  on pipe surface for (a): a single-pipe absorbing cavity; and (b): a reflecting cavity

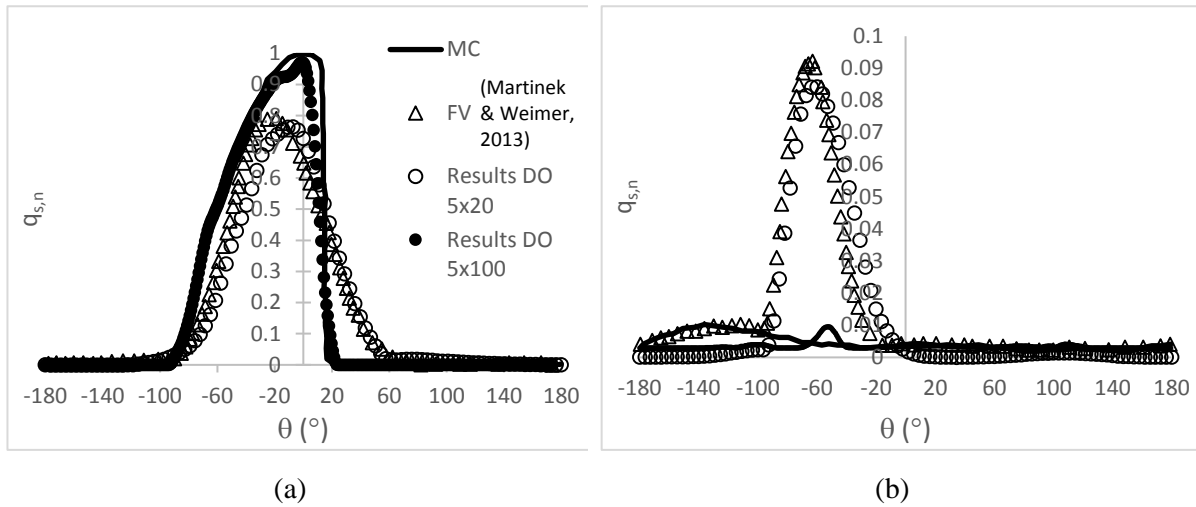


Figure 3.6: The normalised heat flux values  $q_{s,n}$  for (a): the front pipe; and (b): the back pipe in a five-pipe reflective cavity receiver

From the results represented in Figure 3.5 and Figure 3.6, a number of conclusions can be drawn that should be applied in future simulations with similar parameters. There is a noticeable discrepancy between the results acquired when surfaces in the simulation are reflective. This deviation is largely due to the increase in numerical errors due to the dual combination of false scattering and ray effects. In the single-pipe simulation, the difference between the accepted answer and the simulation result is relatively small, but as the simulation complexity increases, the results diverge from the actual answer, particularly if the result depends on accurate specular beam directions. To improve the accuracy of the acquired solutions, the discretisation of the mesh, and, in particular, the RTE equation has to be increased. From the case study discussed in section 3.2.1, it should be noted that the  $N_\phi$  used by Martinek and Weimer (2013) was unnecessarily high, and can be lowered to 3, which does not lead to any loss in computational accuracy, while reducing simulation time and required computational memory.

### 3.2.3 Multi-tube solar reactor case study

In an attempt to investigate the utilisation of MCRT and FVM in the current study, as well as the effect of various heat flux profiles at an aperture on the conjugate heat transfer, the 2D Martinek and Weimer case discussed in section 3.2.2 was expanded to a 3D biomass cavity (Marsberg et al., 2015). Based on results and conclusions drawn from the previous case studies included in preceding sections of this document, it was decided that a connection method should be developed between SolTrace and ANSYS Fluent. This would solve the drawback of the computational resources required for the ray-tracing part of the simulation, with only reasonable accuracy using FVM, and the conjugate heat transfer calculation, which SolTrace cannot perform.

Using both built-in and scriptable functions in SolTrace, it is possible to export trace data from single or multiple surfaces to text files. For this study, the initial testing of exporting data used the trace intersections with an aperture surface (see Figure 2.18) and exported these results to a .profile file, which was compatible with ANSYS Fluent. This was performed by means of the SolTrace scripting capabilities. Profile files were created to match the format stipulated by the ANSYS User Manual (Ansys, 2011). This file can then be interpolated and patched to a semi-transparent surface in the ANSYS Fluent software.

The heat flux profiles that were used are depicted in Figure 3.7, using a Gaussian distribution (Figure 3.7(a)) to be compared with a flux map generated from the SolTrace replication (Figure 3.7(b)) of the PS10 field (see Figure 2.18). Even when accounting for the fact that the solar position used resulted in a rotated distribution when compared to the Gaussian distribution, it is clear that the heat flux predicted by using MCRT is significantly different from the Gaussian distribution such as to validate further investigation of “real” heat flux distributions.

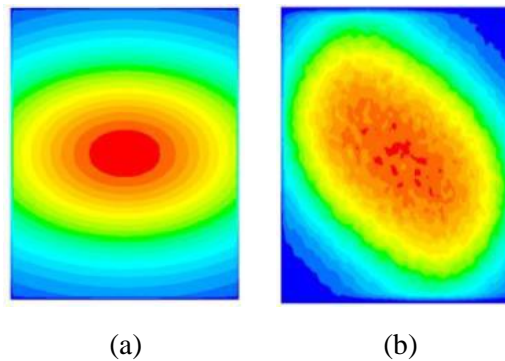
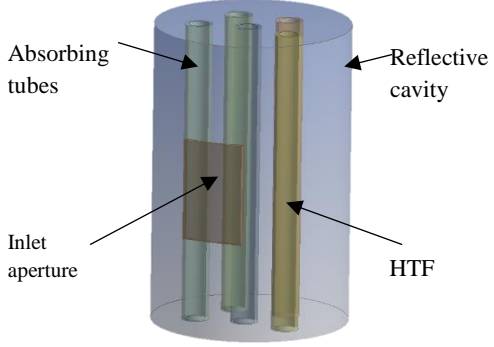


Figure 3.7(a): Gaussian; and (b) MCRT solution heat flux maps

Table 3.1 contains the boundary conditions and properties that were allocated to the biomass receiver. The DO discretisation used was  $15 \times 15$ . Notably, this geometry is used as a test case to demonstrate the possibility of using MCRT as a method to solve the large computational power issues that were experienced in the case study by Craig et al. (2015), initially discussed in Chapter 2.

The distributions shown in Figure 3.7 were applied as a boundary condition at the inlet aperture, which implies that the full domain that would contain the heliostat field is not required.

Table 3.1: Biomass cavity simulation properties

Geometry	Description
	Semi-transparent wall, with the profiles of Figure 3.7 mapped to surface.
	Cavity walls are perfectly reflective with $q = 0W$ .
	Absorber tubes, $\epsilon = 0$ , <i>Cu</i> material properties
	HTF is set with $H_2O$ fluid material properties and $\bar{v}_{in} = 0.005 \text{ m/s}$ .

Results showed promising trends using these patchable heat sources. Figure 3.8(a) shows a good translation when compared with a SolTrace run, which was used as a comparison and used the patching surface in the finite volume domain. This method also highlights the advantages of having a more

realistic heat source applied to solar receiver surfaces, for instance the identification of thermal hot spots and areas of high re-radiation losses.

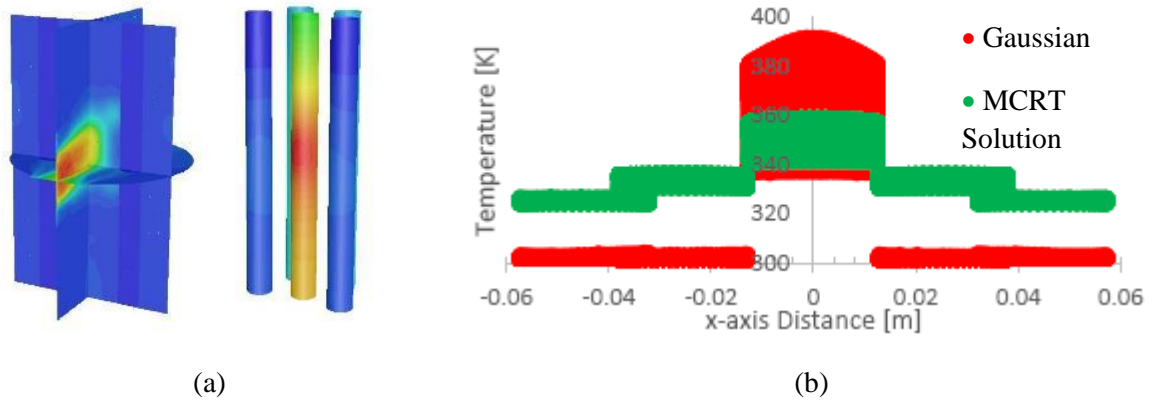


Figure 3.8(a): The incident radiation distribution for MCRT solution solar load; and (b): temperature on the surface of the middle tubes

### 3.3 Modelling complex geometry

Patching ray information to an inlet aperture in section 3.2.3 proved to be reasonably successful. It improved the overall accuracy and decreased the required computational resources significantly to perform the simulation. Even with the reduced domain in the CFD environment, which would need to be discretised, the DO discretisation level necessary to capture the specularly of incident radiation from the aperture still limited the size and complexity of the geometry that could be analysed. Since it is known that re-radiation from the receiver surfaces is diffused in nature, it was hypothesised that the mesh and DO discretisation could be significantly reduced if heat flux values could be patched to the surfaces of final intersection.

#### 3.3.1 Parabolic tubular cavity receiver case

To showcase the necessity for a numerical method that can use MCRT to predict heat flux absorption in a cavity receiver, the case study on an experimental HPAR cavity integrated into a Brayton cycle performed by Craig et al. (2015) is presented.

In an attempt to move towards a 3D simulation of a cavity receiver with the solving of the RTE, a tubular cavity receiver (see Figure 3.9(a)) is situated at the focal point of a parabolic dish (see Figure 3.9(b)), is simulated using FVM (Craig et al., 2015). Two strategies were employed in this case study, and the accuracy of results compared in the conclusion.

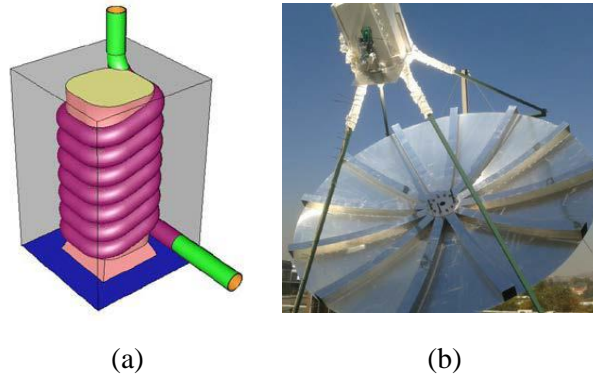


Figure 3.9(a): Tubular receiver geometry of test case; and (b): experimental setup of parabolic dish and tubular receiver (Craig et al., 2015)

The first strategy was an attempt to use axisymmetric modelling on the computational domain. The smaller discretised domain is an advantage, which means that fewer solved RTE equations are necessary. However, the geometry is not replicated accurately because it is not a symmetrical shape. Therefore, it leads to results being inaccurate.

For the second strategy, a purely 3D model was used as the next test case. Since the meshed domain was so much larger, the RTE discretisation had to be reduced to maintain reasonable use of computational resources. This method considers the actual shape of the domain. However, inaccuracies due to the smaller domain and DO discretisation will occur.

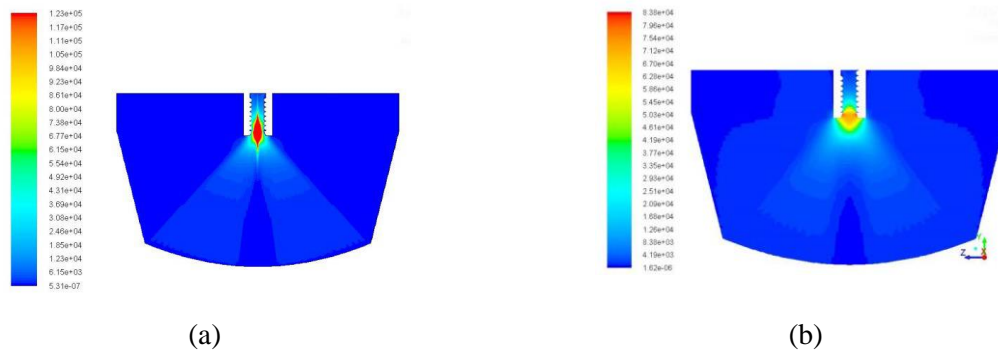


Figure 3.10: Incident radiation contours  $[W/m^2]$ , for (a): axisymmetric (DO 80 x 80); and (b): full 3D model (DO 25 x 25) (Craig et al., 2015)

Distributions of the absorbed radiation heat flux are similar in shape and the maximum values attained for both cases (Figure 3.10). However, there are discrepancies between the two distributions, most notably that the axisymmetric case results are not as continuous as those of the 3D case. The 3D results are also more spread out in the vicinity of the receiver, which is more likely due to the insufficient discretisation of the RTE equation causing false scattering as well as ray effects. These distributions were interpolated to a surface as a volumetric heat source in a finite volume conjugate heat transfer model (see Figure 3.9(a)). The interpolation errors that may occur using these methods should be noted at this point. Even though the accuracy of the axisymmetric model is significantly higher than that of the 3D model, Craig et al. (2015) concluded that this accuracy reduces due to the differences between an axisymmetric assumption of the geometry, as well as the discontinuous distribution of data points along the height of the receiver.

Using the methods above, simulations for the full 3D case were already using large amounts of computational power. To realistically reach the converged discretisation values would require more computational power than that which was available. For instance, even the coarsest 3D model already used 120 GB of memory with no sign of convergence being achieved (see Figure 3.11).

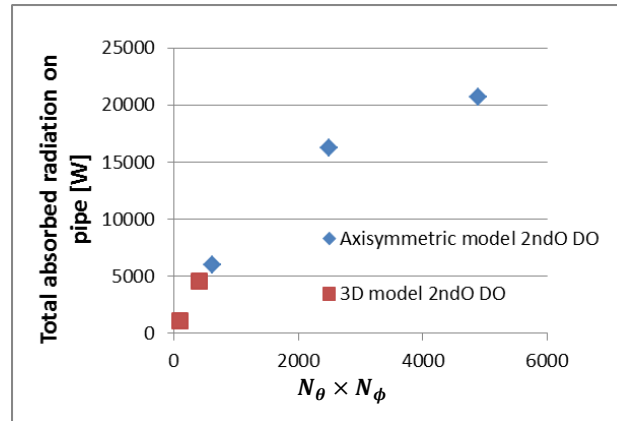


Figure 3.11: Total absorbed radiation [W] on receiver tube for the 2<sup>nd</sup> order (2ndO) Discrete Ordinates axisymmetric and 3D case (Craig et al., 2015)

### 3.3.2 Complex geometry modelling methodology

To reduce the interpolation and simulation errors encountered by Craig et al. (2015), it was determined that, to increase simulation accuracy, a method of predicting heat flux up to a final intersection surface of the cavity receiver would need to be developed.

Since SolTrace does not include the possibility of complex surface definition, scripts were written so that complex surfaces could be represented by multiple simple surfaces, such as circles.

In a simulation, the workflow, depicted in Figure 3.12, was used as a method of extracting the heat flux distribution over a complex absorbing surface.

This method would use a mesh file that was generated with the ANSYS meshing software, and Python scripting to identify surfaces of interest and reinterpret this data into values that would be required to fully define this surface in the SolTrace software. The principle of surface replication in SolTrace was to use a circular surface as a representation of each mesh element in the meshed surface from the generated file. If these circles were correctly sized and positioned, they would overlap and replicate a good approximation of the meshed surface (see Figure 3.13(a)). From the element definition in SolTrace's requirements, as mentioned in section 2.6, the Python script would need to identify all the nodes in each element of the surface in question and extract each node's coordinates in space (see Figure 3.13(b)) to correctly align it in the SolTrace stage coordinate system.

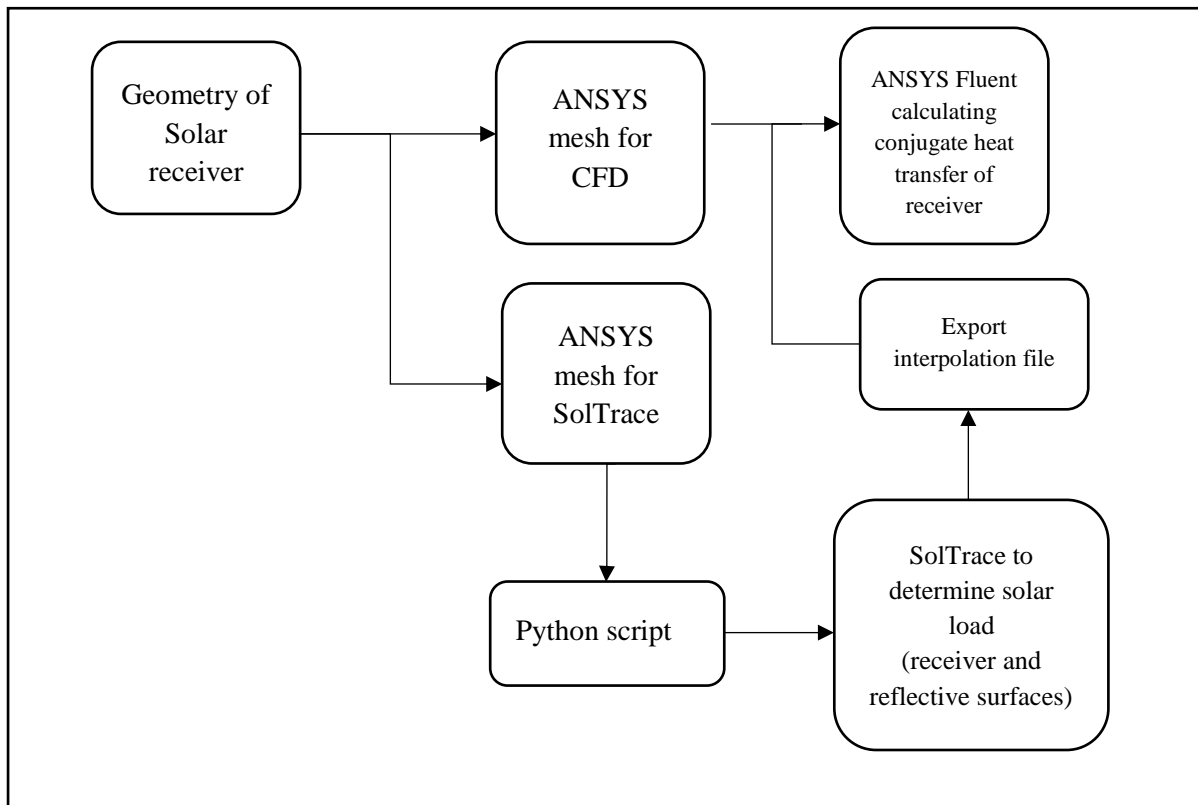


Figure 3.12: Flow diagram depicting the process of producing a heat flux distribution over a complex geometry surface

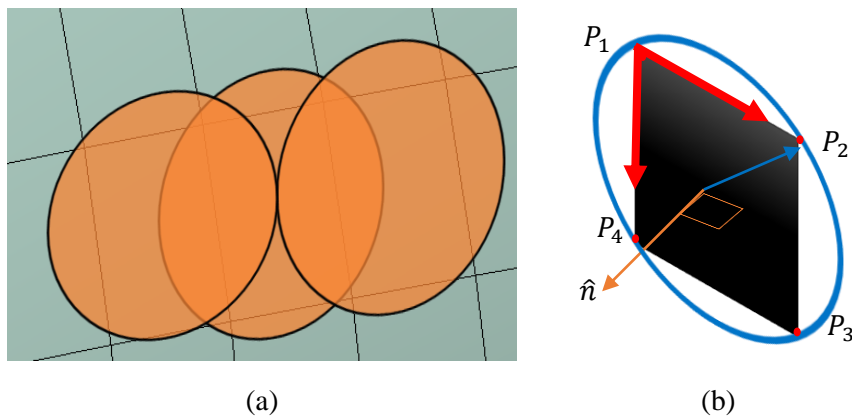


Figure 3.13(a): A replication of meshed surface using circles in SolTrace; and (b): points used in Python script to calculate the properties of the element

This information was then used to calculate the centroid of the element so that the element could be correctly positioned in the SolTrace domain. The direction in which the face would need to point would then be calculated using any three nodes in the element to find the unit vector. Since SolTrace direction definitions use aim points or coordinates rather than unit vectors, the unit vector would need to be added to the centroid coordinates as a simple solution to determine the aim point.

The surface area of the element would need to be calculated so that once the final SolTrace simulation was completed, the total flux that was absorbed by the surface could be calculated.

Finally, the diameter of the circle enclosing the mesh element would need to be calculated. To ensure that there was no possibility of “leaked rays” through the surface by having gaps between circular elements in the SolTrace simulation, the circle was sized by determining the maximum distance between the centroid of the element and any of its nodes. This value would then be used as the radius of the circle. However, this step requires careful consideration. Using this technique, the mesh that is originally produced needs to have good cell aspect ratios as close as possible to 1. The further the aspect ratio trends away from this, the larger the circular disc would be to represent that element in SolTrace.

Once all the elements were processed, the Python script allowed the user to enter optical properties from an inbuilt library of materials, and to define if surfaces were refractive or reflective. All this information, to be interpreted by the SolTrace script, was written to a number of text files. The full Python script, showing complete detail of how information was extracted and determined, as well as all other importable modules, is included in Appendix A.

After the mesh processing by the Python code is complete, a SolTrace script is run through all the generated text files, extracting the data so that each of the elements could be extracted and imported. Optical property sets are also automatically defined in this process, based on inputs that were previously given during the Python process. Once all the elements are successfully imported, the script would run the simulation.

With traces complete and surface ray interaction information available, a separate SolTrace script is used to extract this data into a text document that has a format that can be interpreted by ANSYS Fluent. A number of formats can be used, but the most successful method was found to be an interpolation file, or.ip file. The interpolation process requires the information to be exported as a volumetric heat source. With this being the case, the data would need to be re-scaled from  $W/m^2$  to  $W/m^3$ . Equation 3.1 is used to calculate the volumetric heat source for each element.

$$Q_{element,i} = \frac{PPR \times rays_i}{A_{element,i} \times t} \quad 3.1$$

The SolTrace scripts that were used to achieve element data import and trace information export are included in Appendix A.

To patch the.ip file to a solid body in ANSYS Fluent as a volumetric heat source, a combination of two user-defined functions would need to be used (Moghimi et al., 2015). The method entails initially defining a user-defined scalar (UDS) location, as well as a user-defined memory (UDM) location. The.ip file could then be interpolated into the UDS memory location by means of the inbuilt functionality of ANSYS Fluent. The user-defined function (UDF) is then used to copy the UDS to the UDM. Finally, the UDM information becomes accessible by accessing the new, user-defined source terms in the cell zone condition menu of ANSYS Fluent. The UDF script that was used to perform these operations in ANSYS Fluent can be found in Appendix A: (Craig et al., 2010).

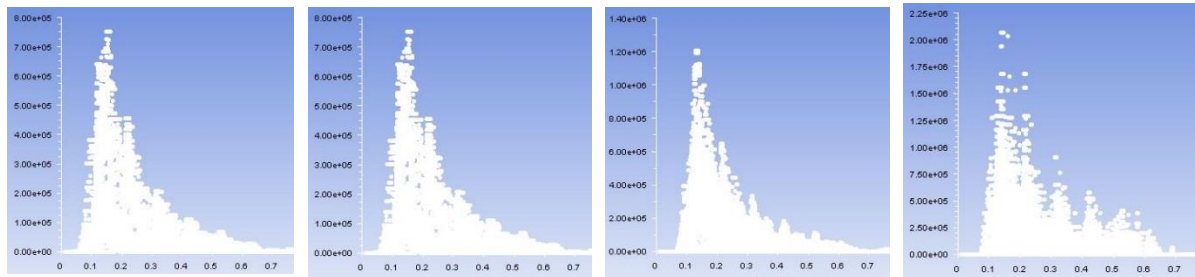
### 3.3.3 Heat source patching with Brayton cycle test case

As discussed earlier in this chapter, the tubular cavity receiver is reintroduced as the test case for patching heat flux directly to the absorbing surface (Craig et al., 2016b). The computational expense



Table 3.2: Comparison of the absorbed radiation flux on tubular walls in SolTrace and integrated volumetric heat sources in ANSYS Fluent, using  $DNI = 1000 \text{ W/m}^2$

Mesh type	Power absorbed by tubes [W]	Power reflected by dish [W]	Integrated surface absorbed flux [W]	Integrated volumetric source [W]
Very coarse	53 263	56 367	52 910	53 633
Coarse	53 269	56 388	52 467	53 268
Medium	53 289	56 408	51 911	52 526
Fine	53 223	56 385	52 343	52 938



(a) Very coarse mesh

(b) Coarse mesh

(c) Medium mesh

(d) Fine mesh

Figure 3.15: Absorbed radiation flux [ $\text{W/m}^2$ ] on tubular cavity walls plotted as a function of cavity vertical position [m] for different mesh sizes used and 1 million SolTrace ray intersections

Using this success, a trial case is considered using the same geometry, but varying the tubular solar absorptance. Using the same conditions as from the previous case study (Craig et al., 2015), the methodology was able to show its true improvement in the process efficiency by generating these two flux distributions in a matter of hours.

The conjugate heat transfer results, which are portrayed graphically in Figure 3.16, display the various aspects of the simulation that may be used to determine design performance, identify potential problems, such as hot spot formation, and recommend improvements if necessary. Figure 3.16(c) shows how the interpolated data appears visually on the surface of the absorber surface. Full results from this comparative simulation can be found in the published paper of Craig et al. (2016b), of which the author of this dissertation is a co-author.

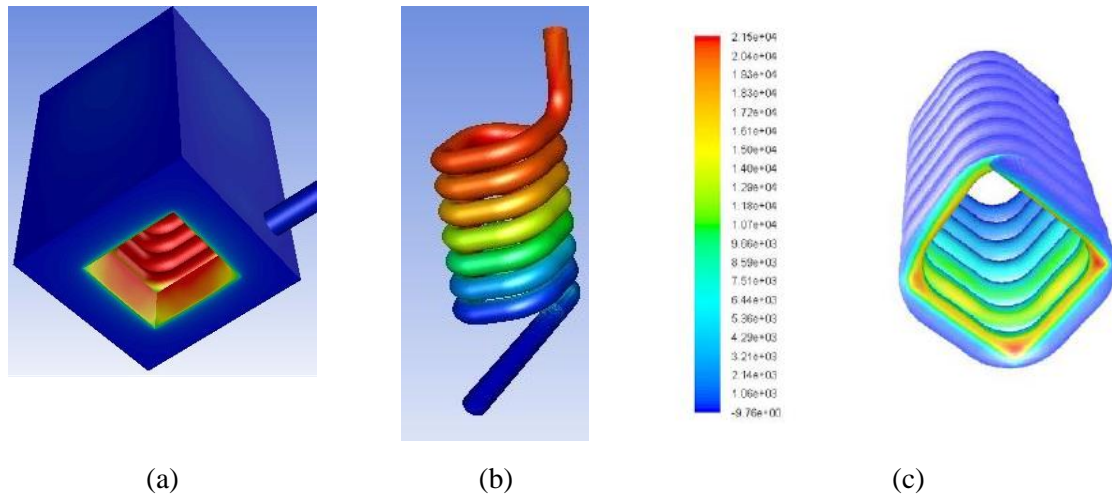


Figure 3.16: The CFD simulation of heating of HTF (a): surface temperature; (b): tube temperature distribution (Craig et al., 2016b); and (c) as a result of applied solar absorbed radiation (Craig et al., 2015)

### 3.4 Conclusion

This chapter primarily dealt with numerical methods regarding the prediction of heat flux distributions and the conjugate heat transfer in computational domains when considering radiative heat transfer. The case studies that were researched and carried out in some cases led to the following revelations:

- To achieve accurate results when solving the RTE, a large amount of computational power is required due to the discretisation of the domain, as well as the DO method in an effort to reduce false scattering and ray effects.
- MCRT provides highly accurate results in terms of the interaction of rays with surfaces and the prediction of incident radiation and the resultant heat flux distribution. It proves to be a useful tool, provided that a sufficient number of rays are generated by the MCRT method.
- Using SolTrace scripting, complex geometric surfaces can be replicated in the SolTrace simulation. Heat flux distributions can be extracted from these intersected surfaces to be interpolated onto surfaces in ANSYS Fluent.
- Accurate results, when compared to experimental data, can be generated by means of combining MCRT with FVM to predict the performance of solar power plants, for both point- and line-focus systems providing that absorbing surfaces are solid, relatively stationary surfaces.
- The proposed method provides an effective variable heat flux distribution to a solid surface. As a result, it can therefore be used in both laminar and turbulent flow regime problems.

# Chapter 4: Verification and validation

## 4.1 Preamble

The main design goal for a receiver cavity is to absorb solar energy that has been concentrated towards its absorbing surfaces as effectively as possible. This efficiency is achieved by minimising thermal losses from the system by developing new designs and configurations. Through the use of numerical methods, the engineer is able to simulate a large number of cases in a relatively short period of time. For these results to be relevant, they have to be proved to be accurate when compared to results that would be achieved using experimental methods.

In this chapter, the numerical methods are validated by comparing them with a suitable experimental result. The confirmation of these two methods comprises two main sections:

1. MCRT model validation
2. CFD model validation

## 4.2 Experimental case for validation

An experimental case (Maharaj, 2015), which is attractive for validation purposes due to the number of aspects contained in the report, is used to determine the overall accuracy of the numerical methodology developed in Chapter 3.

This technical report contains several aspects that allow for the full validation of the methodology:

1. Specular reflections
2. CFD
3. Combination of ray absorption and numerical heat transfer

This research attempted to use a tubular cavity collector in conjunction with a parabolic dish reflector to study heat transfer mechanisms in the complex tubular receiver. The experimental setup, as seen in Figure 4.1, has four main components that are replicated in the computational domain. The components include the following:

1. Parabolic dish receiver – 1.5 m diameter, positioned 0.587 m away from the focal point
2. Cavity support structure
3. Cavity receiver (see Figure 4.2 for more detail)
  - a. Insulation
  - b. Tubular cavity receiver

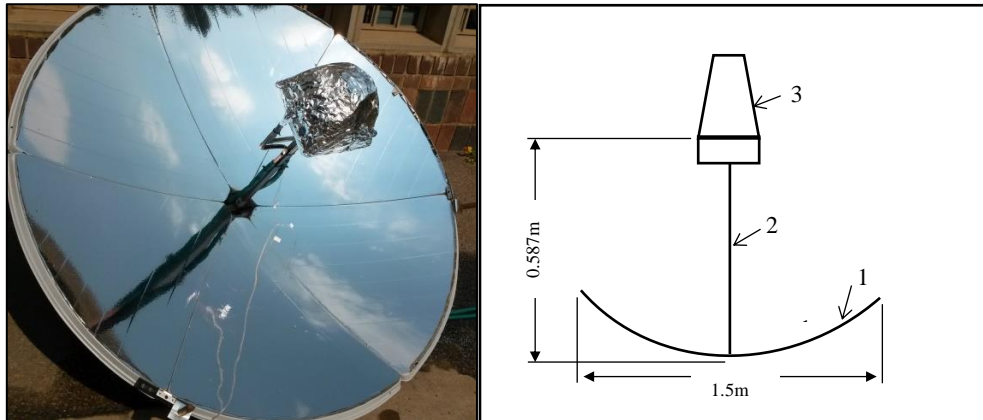


Figure 4.1: Parabolic dish and helical absorber experimental setup (Maharaj, 2015)

The geometry representation, as seen in Figure 4.2, is created using the workflow ANSYS package Workbench R18.1. This allows the creation of geometry, subsequent meshing and simulation of the FVM using ANSYS Fluent to be solved in a single workflow.

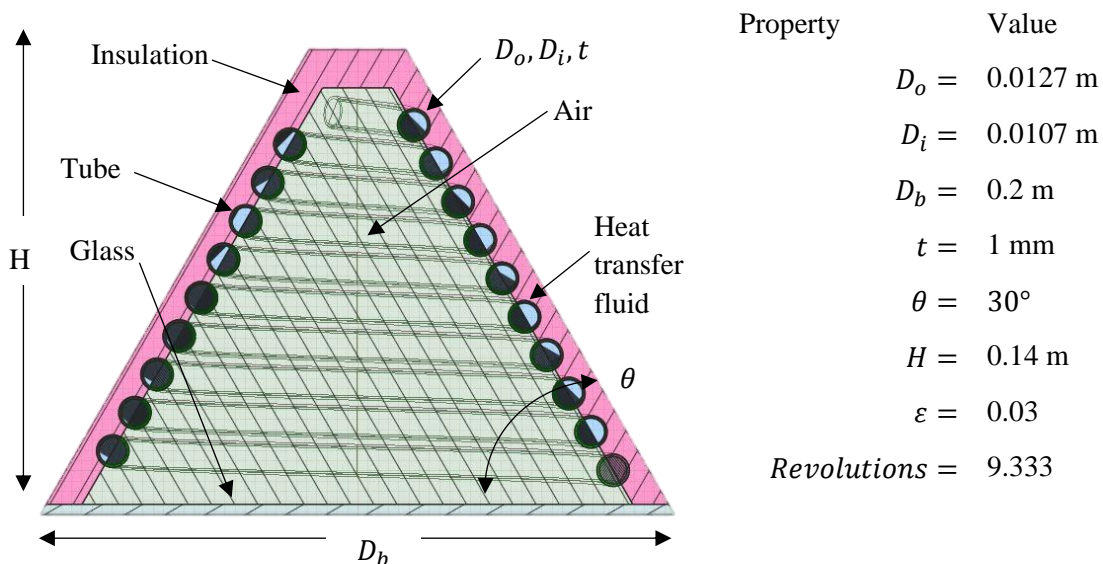
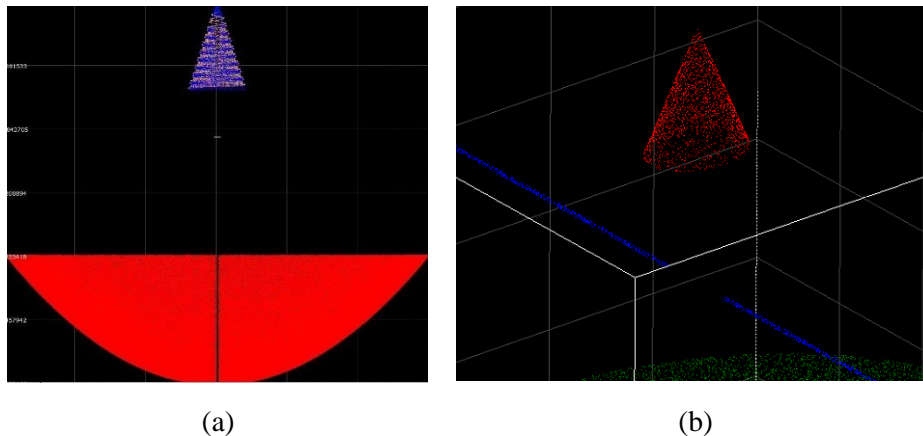


Figure 4.2: Numerical representation of experimental geometry in ANSYS SpaceClaim

To predict the insolation this cavity experiences, the methods described in section 3.3 are utilised here. A mesh simulation is generated for the SolTrace and imported into the SolTrace domain with a scale that is automatically set (see Figure 4.3(a)), which makes the parabolic dish appear more pronounced than it is in reality. Figure 4.3(b) shows that the inclusion of additional elements, such as the parabolic dish and a conical surface that replicates the effect of the insulation surrounding the absorber tube in the SolTrace simulation, are also included. A flat, rectangular strip is also included, which serves to replicate the effect of the shadowing caused by the support structure holding the cavity in place. This effect is observed in Figure 4.4(a), where elements towards the middle of the cavity experience fewer ray interactions, and will effectively lessen the total amount of radiation that is made available at the aperture, therefore decreasing the system's optical efficiency.



*Figure 4.3(a): Representation of geometry in SolTrace computational domain; and (b): zoomed view of insulation cone and sting shadow*

For validation of MCRT as a method of replicating the real-world reflection and absorption of surfaces to quantify the accuracy of this portion of the final methodology, a number of verification studies are used to determine critical parameters that should be in place to achieve an acceptable accuracy of results.

As the literature study has indicated, it is necessary to perform a convergence study on this simulation. Due to the numerically defined surfaces and statistical probability of the generated rays and surface interactions, both the discretisation of the geometric surfaces and the number of generated rays are required to reach convergence.

To represent a complex geometry such as the helical absorber, this surface is derived from a meshed surface. It is processed using scripting in SolTrace to produce the representation of the helix in this computational domain (Figure 4.4(a)). Additionally, an adequate number of rays should be generated to accurately predict the final intersection points or heat distribution on the surface of interest, as discussed in section 3.3.3. Simulations were run to determine whether convergence has been reached in the ray tracer and the amount of heat flux absorbed by the elements of the tubular receiver. The number of rays used in the simulation was increased until the results remained consistent. The heat flux was then normalised to 1, and the results were compared (see Figure 4.4(b)). It is apparent that once simulations use approximately 300 000 or more rays, the results converge. This value is therefore specified as the minimum value allowed in any SolTrace run that is performed for this test case.

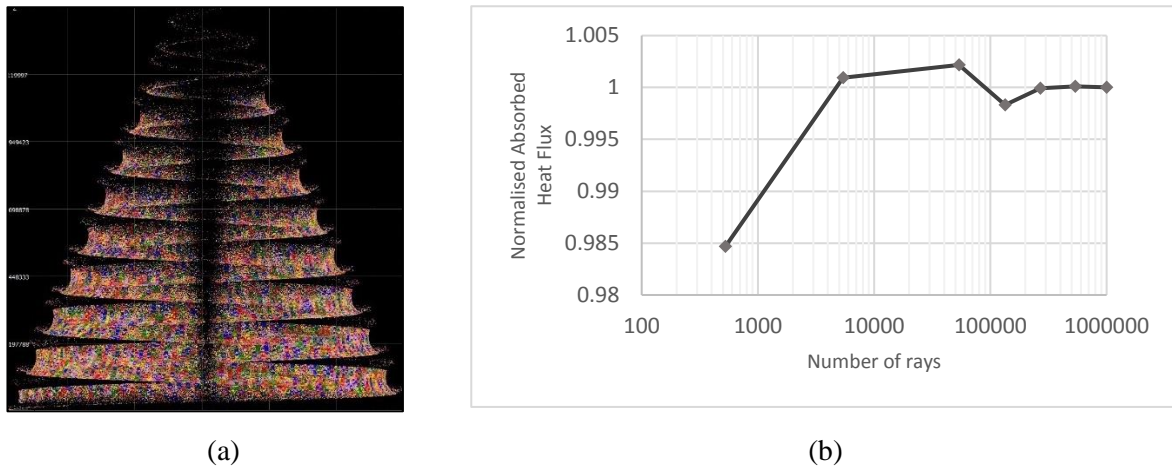


Figure 4.4: A numerical representation of helical absorber tube in the SolTrace computational domain using 1.9 M plotted rays

The number of rays used in the simulation is not the only parameter that requires consideration in the MCRT steps. The number of mesh elements that is required to accurately represent a surface is an essential consideration. Figure 4.5 shows two sample mesh sizes that were generated for use in this section of the validation procedure. These mesh sizes were 24 000 and 100 000 elements respectively, and can be considered as the coarse and the fine mesh for this numerical study.

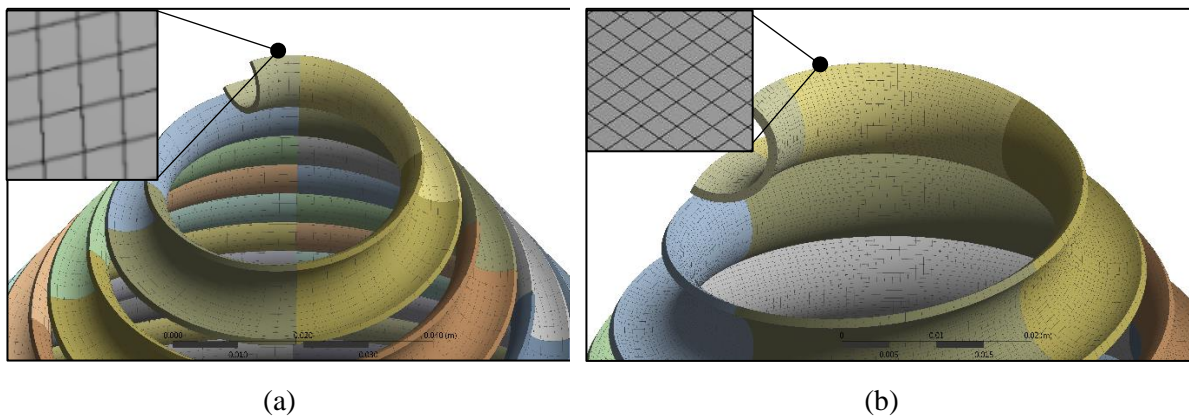


Figure 4.5(a): Coarse mesh; and (b): fine mesh using 24 K and 100 K elements, respectively

A similar procedure to the one followed previously is carried out to determine the minimum number of elements that is required to accurately capture distribution and heat flux magnitude captured by the helical surface. Simulations on five different mesh sizes were run, ranging from a very coarse mesh (16 223 elements) to a very fine mesh (142 239 elements), using a range of generated rays from 1 000 to 100 000 rays. Figure 4.6 shows the normalised results of the integral absorbed heat flux on the element surfaces. From these results, it is evident that relatively fine mesh densities would be required, with only a 2% relative error between the two finest mesh densities to comprehensively capture distribution and magnitude of heat flux. The minimum cell density of  $230/cm^2$  is calculated as that which would be required with the 300 000 ray minimum. This once again accurately captured the ray intersection data.

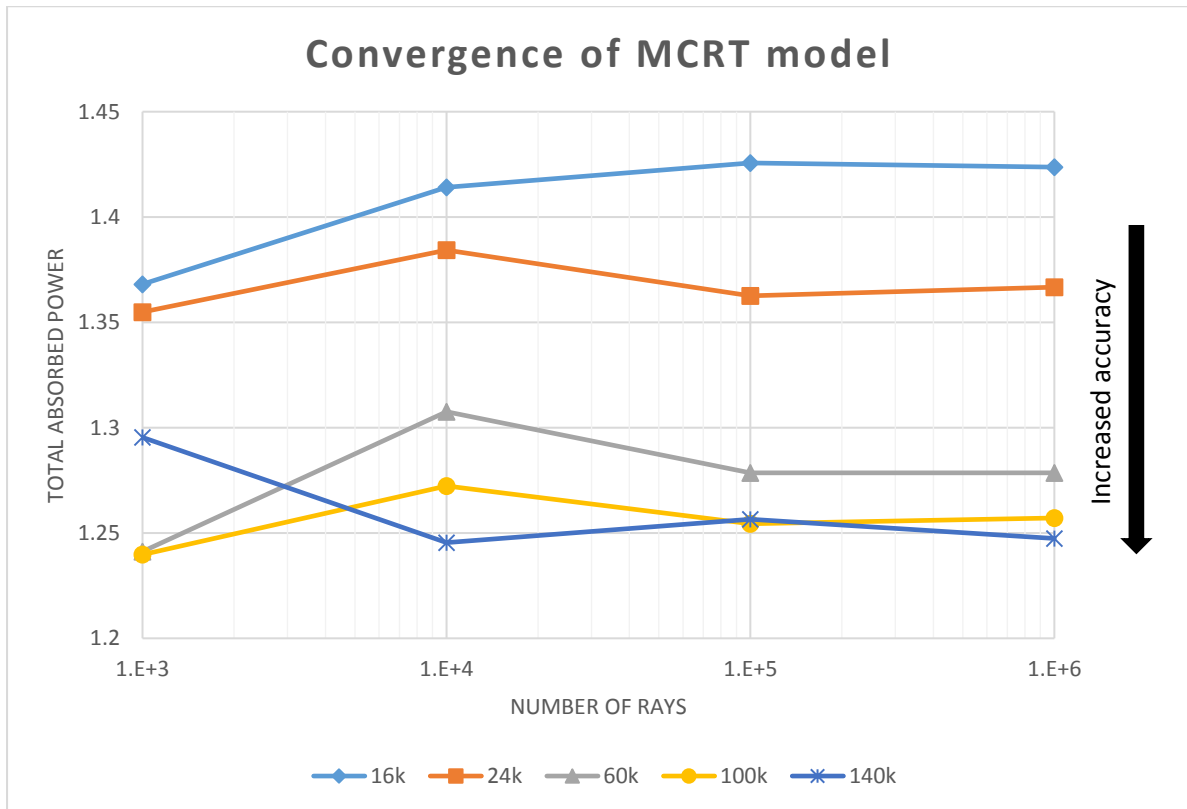


Figure 4.6: Convergence study indicating the element number versus the number of generated rays

### 4.3 CFD model validation

Results for this experimental setup were acquired by Maharaj (2015) over a few days, using various parameters as input. In this validation case, the experimental setup for the closed cavity case, performed on 16 October 2015 is used. These results were captured on a day and time where the direct normal irradiation (DNI) was recorded to be  $845 \text{ W/m}^2$  with an ambient temperature of  $32 \text{ }^\circ\text{C}$ .

#### 4.3.1 Computational domain setup

The computational domain was set up to accurately simulate the physics of the tubular cavity receiver, as well as to make the setup simple enough not to introduce any unnecessary complications. Assumptions that were made to maintain simplicity were contained in the relevant following subparagraphs of this section.

To ensure an accurate solution and development of flow throughout the domain, the mesh of the domain, which is likely to experience high gradients during the solution, received particular attention during the meshing process. Flow through a tube with the assumption of non-slip walls will form a boundary layer in a fully developed flow condition. To account for these changes in velocity close to the wall throughout the whole HTF domain, an inflation layer is used with a particularly fine, structured mesh that grows as it moves away from the wall and gradients become less steep (see Figure 4.7). Since only conduction is solved through the tube solid, only two elements are included throughout the thickness.

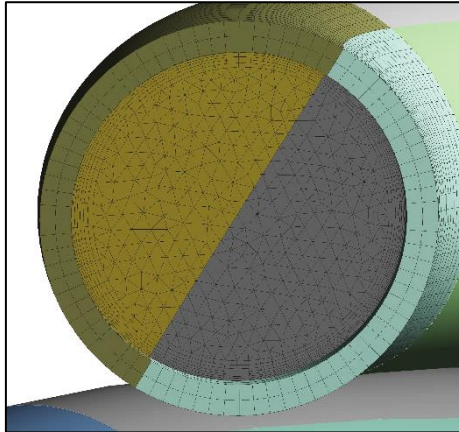


*Figure 4.7: Validation case pipe mesh and HTF inflation layer*

Figure 4.8 shows the geometry of the validation study represented in the numerical domain. To accurately represent the solution to this simulation, the correct boundary conditions and cell zone properties are required to match those of the experimental setup. These will be discussed in further detail in section 4.3.2. Assumptions that were made in an attempt to simplify solutions, with a minimal effect on the solution, are discussed here.

The cavity air in the simulation is assumed to be a semi-transparent solid. With this assumption, buoyancy effects, such as natural convection in the cavity, are neglected, but still allow the radiation heat transfer to pass through it. Since the temperatures of this system are assumed to be low, buoyancy effects can be assumed to be negligible.

The HTF inlet and outlet in this domain originate from inside the cavity, which means that the ends of the pipe do not propagate through the insulation, as can be deduced from Figure 4.8. Without the correct boundary conditions and domain setup, this geometry violates the physical laws of ANSYS Fluent. However, by separating the coincident zones between the inlet and the insulation or cavity air, it is possible to force the assumption from Fluent that these walls are not coincident with each other. Using this technique, mesh sizes are reduced significantly, with the consideration that the piping lengths that are not included add little value. The piping that is needed to pass through various zones is also simplified.

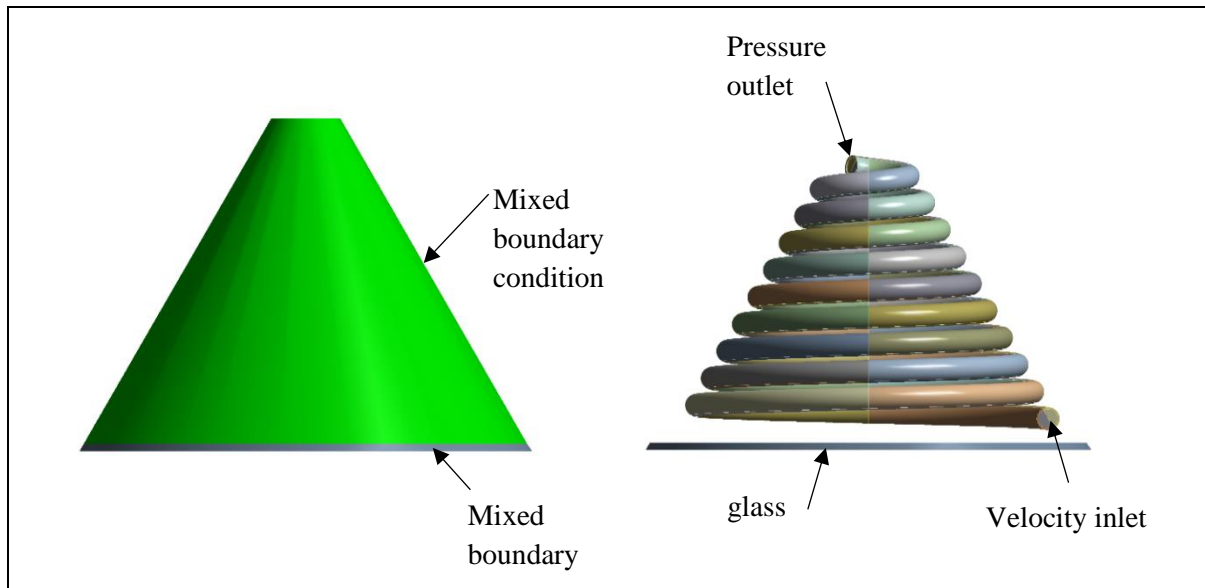


Figure 4.8: A numerical model of receiver cavity and boundary conditions

## Materials

Material properties for this validation study were assumed to be constant (see Table 4.1) (Maharaj, 2015). Since temperature changes within the domain would be low, flow would be steady state, laminar and without phase change. Properties are based on those documented in the experimental case report (Maharaj, 2015).

Table 4.1: Validation case material properties (Maharaj, 2015)

Zone	Type	Material	Properties			
			$\rho$ kg/m <sup>3</sup>	$C_p$ J/kgK	$k$ W/mK	$\alpha_c$
<b>Cavity</b>	Solid	Air	1.225	1 006.43	0.0242	N/A
<b>Insulation</b>	Solid	Glass wool	12	871	0.039	N/A
<b>Tubing</b>	Solid	Copper	8 978	381	387.6	N/A
<b>HTF</b>	Fluid	Water	998.2	4 182	0.6	N/A
<b>Glass</b>	Solid	Glass	2 650	200	1	18.15

Heat flux data that was acquired from the SolTrace simulation is written to an .ip file and interpolated into the UDS location in ANSYS Fluent. This data is then copied to the UDM with a UDF, which becomes accessible to the user through a variable that is now selectable as a source term in the ANSYS Fluent user interface. To ensure that accuracy is maintained, a comparison between the total absorbed heat flux value and the integral of the interpolated heat flux in Fluent are compared. Initially, using 1 M ray simulations for smaller mesh sizes up to 60 000 yielded substantial differences between the two aforementioned values, approaching 10% correlation differences, as can be seen from the graph in Figure 4.9.

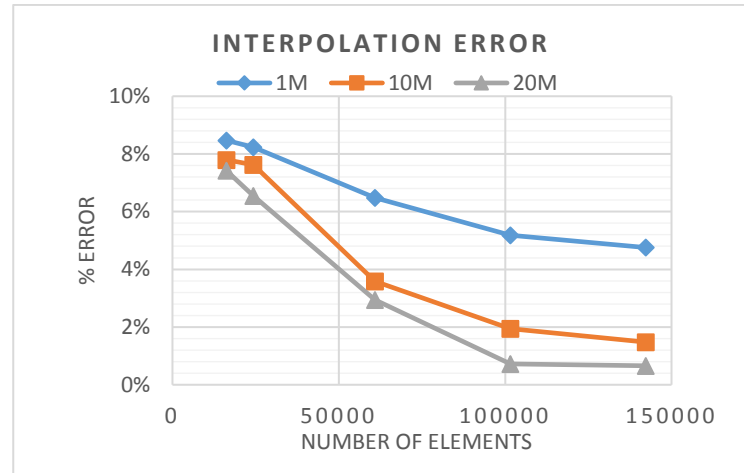
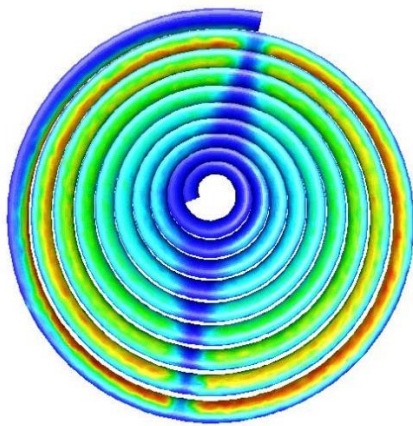


Figure 4.9: An example of SolTrace data patched to the equivalent volume in ANSYS Fluent with corresponding percentage errors of interpolated values

To improve this correlation, meshes that are more refined were used due to their proven convergence from previous tests, as well as the guaranteed minimisation of errors. Much larger traces were run on these meshes to test whether this would eliminate the numerical differences caused by ANSYS Fluent's interpolation methods. Since SolTrace has limited memory for its simulations and to achieve a 2 000 000 ray result, these simulations were broken into 100 000 generated ray simulations and linked together using post-processing scripts or Microsoft Excel spreadsheets. This method required random seed values for each trace to be done to ensure that ray data was not replicated.

This method had the desired effect on the interpolation error, dropping it from almost 10% to below a 1% error when in use. From the raw data analysis, elements that were shadowed in some traces were intersected in others, allowing for a more continuous heat flux distribution. This more continuous distribution of data allows for a reduction in interpolation errors. By using random seed values to generate different ray distributions in a number of simulations, and concentrating these trace results, a refined heat flux distribution is achieved. This method is now preferred for all simulations that require highly accurate performance estimations.

#### 4.3.2 Boundary conditions

To determine all boundary conditions, the atmospheric conditions at the time of the test should be determined. Most importantly, the DNI, wind conditions and ambient temperature are necessary. Using the Southern African Universities Radiometric Network (SAURAN), data recorded on 16 October 2015 from 13:00 showed a DNI value of  $845 \text{ W/m}^2$ , ambient temperature of  $32 \text{ }^\circ\text{C}$  and a variable wind speed of approximately  $5 \text{ ms}^{-1} - 9 \text{ ms}^{-1}$  (Brooks et al., 2015). As a result, heat transfer coefficients are set as an approximation of  $15 \text{ W/m}^2\text{K}$  for external forced convective heat loss in windy conditions (Fang et al., 2011).

All boundary conditions are set to match those measured and documented in the experimental work (Maharaj, 2015). Table 4.2 lists the boundary conditions that were implemented in the numerical validation case.

Table 4.2: Boundary conditions used for the validation case based on Maharaj (2015)

Boundary	Boundary condition type	Conditions
Inlet	Velocity inlet	$v_{in} = 0.32 \text{ m/s}$ $T_{in} = 293 \text{ K}$
Outlet	Pressure outlet	$p_{out} = 0 \text{ Pa gauge}$
Insulation outside wall	Mixed boundary condition	$h_{ins} = 15 \text{ W/m}^2\text{K}$ $T_{sky} = 273.15 \text{ K}$ $T_{amb} = 305.14 \text{ K}$ $\varepsilon = 0.3$
Glass aperture	Mixed boundary condition Semi-transparent wall	$h_{glass} = 15 \text{ W/m}^2\text{K}$ $T_{dish} = 330 \text{ K}$ $T_{amb} = 305.14 \text{ K}$ $\varepsilon = 0.93$

#### 4.4 Comparison of model validation results

The results for the FVM simulations are recorded in Table 4.3 and Table 4.4. Table 4.3 includes the numerical energy transfer as calculated using ANSYS Fluent's inbuilt functions, as well as the calculated thermal efficiency of the cavity receiver. Table 4.4 includes comparative values between experimentally measured and numerically acquired values.

Table 4.3: Radiation and total heat transfer rates at validation case boundaries

Boundary	Radiation heat transfer[W]	Total heat transfer[W]
Insulation wall	0	(6.75)
Glass aperture	(3 693.97)	(3 741.82)
$\Delta Q_{HTF}$	0	1 546.87
Patchable pipe	0	2 206.31
$\eta_{ther}$ (Equation 2.7)	-	70.1%

The results recorded in Table 4.3 are used to calculate the thermal efficiency of 70.1%, with radiation through the aperture window being the major source of heat loss for this receiver cavity. This is most likely due to the large view factor between hot absorber tubes, and the aperture window, as is visualised in Figure 4.10. The temperature of the HTF, as well as that of the cavity, increases as the energy propagates deeper into the receiver. As previously mentioned, due to this large view factor, the effect will be further intensified as the temperature in the receiver increases. Heat loss due to convection from the insulation, as well as from the glass cover, is practically negligible when compared to the radiative heat loss.

Table 4.4: Comparison of the experimental and numerical results

Parameter	Unit	Experimental	Numerical validation	Percentage error
$\bar{T}_{out}$	K	306.35	307.24	0.3

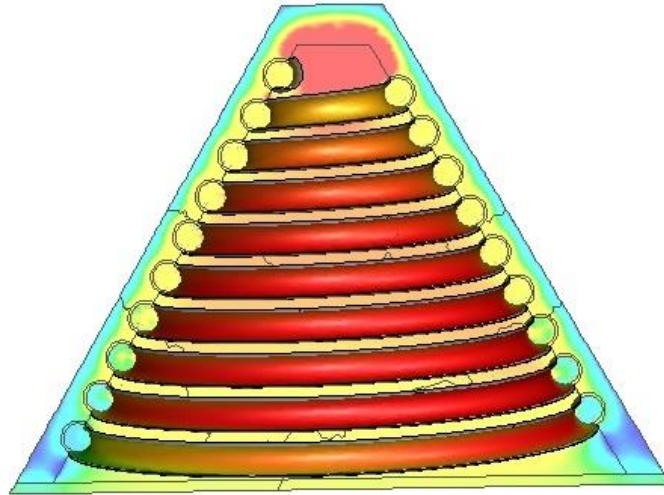
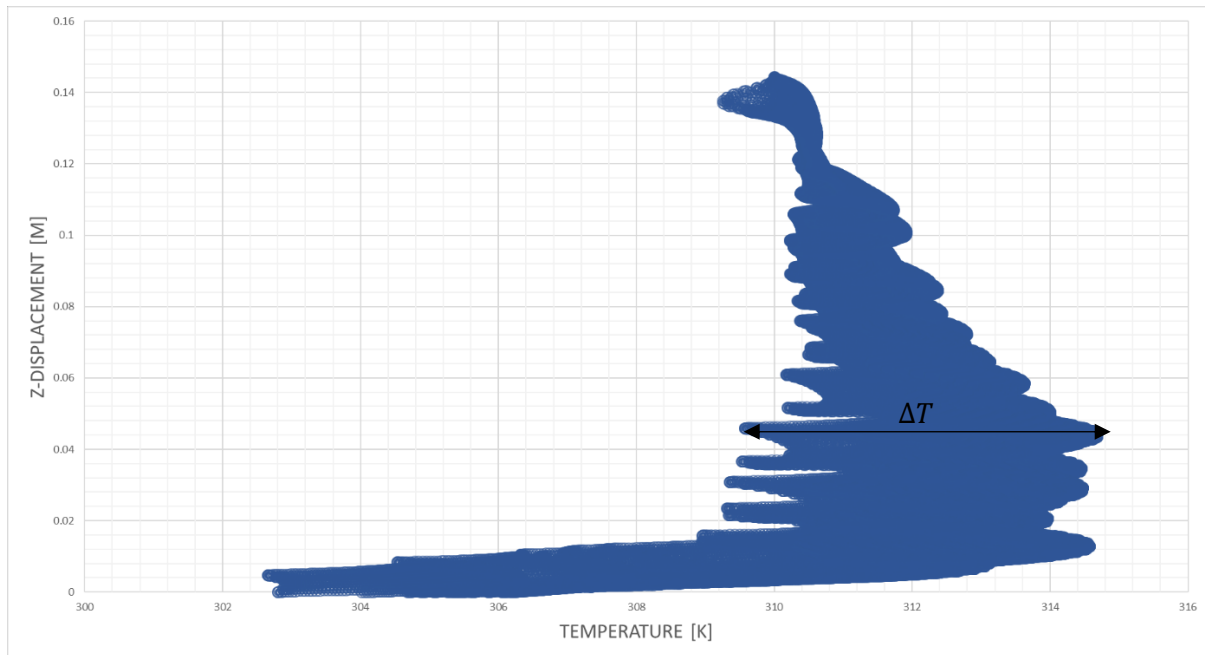


Figure 4.10: Temperature contours for the plane and inner absorber tube for the validation case

Furthermore, from Figure 4.11, it becomes apparent that the absorber tube is prone to having large temperature variations in a section of its wall, as indicated on the graph. This variation will cause undesirable effects such as the formation of hot spots, as well as elevated thermal stress of the absorber tube. As discussed in previous chapters, this will lead to the respective decrease in material performance, and the lifespan of the cavity receiver in long-term operation, particularly when higher temperatures are considered.



*Figure 4.11: The temperature distribution on the tubular absorber surface*

The comparison of outlet temperatures between the experimental case and this validation study (see Table 4.4) indicates a small discrepancy between the measured temperature and numerically determined, area-weighted average of static temperature at the pressure outlet using the FVM. Considering the significant agreement between results, it is possible to use the developed methodology to efficiently analyse the performance of future candidate geometries and drive the designs in directions that are determined by the geometry parameterisation and defined constraints.

## 4.5 Conclusion

In order for a numerical method or model to be considered accurate and used to collect quantitative data, while maintaining the quality of the simulation result, it must first be validated against the experimental results. This validation case has shown that using the methodology discussed, valuable results of reasonable accuracy can be yielded, which allows for decisions on project design and direction.

Reasons for discrepancies between numerical and experimental data can be attributed to a number of factors. Numerous simulations were run to understand and quantify the effect of the mesh sizes and ray numbers that were generated to reduce the interpolation of ray data errors. It is possible to minimise these errors by increasing the discretisation of the domain and increasing incident rays and elements in the MCRT procedure. The accuracy of measurement in the experimental setup may also lead to a discrepancy between the numerical and the experimental results. As discussed in section 3.2.1, discretising the DO method, while solving the RTE equation, can also lead to errors due to false scattering and ray effects. The amount of re-radiation effects in this validation case were low due to the low temperatures in the experimental case being significantly lower than the operating temperatures of the receivers that have been discussed throughout this dissertation. With an increase in temperature, it should be noted that the errors due to false scattering and ray effects may increase. More acceptable results can be achieved through further discretisation of the DO method for errors to be minimised.

It was also deduced that an element density of  $230/\text{cm}^2$  is required to reach MCRT convergence. Even considering the convergence of the MCRT simulation, which requires only 100 000 produced rays, this still produced unacceptable interpolation discrepancies when patching to ANSYS Fluent surfaces. To minimise interpolation errors, 130 elements were required. In this case, 2 000 000 produced rays were required to achieve an interpolation error of  $< 1\%$ .

This validation study exposed the strengths and weaknesses of the methodology and numerical aspects, which are imperative to performing large-scale simulations. With high-accuracy results becoming available, it is possible to begin analysing cavity receiver performance and to use key parameters and constraints to drive a candidate design forward.

# Chapter 5: An iterative analysis of cavity receiver performance

## 5.1 Preamble

In chapters 2 and 3 of this dissertation, concepts aimed at the efficient numerical replication of cavity receivers and their performance were discussed. One such case study that was performed was that of the steam helical tubular cavity receiver by John Pye (Pye et al., 2015), where various iterations of the geometry were investigated and evaluated using their own numerical models and codes.

A similar iterative process has been used through the methodology utilised in the validation case documented in Chapter 4. The process has a similar geometry to that proposed by Pye et al. (2015). This chapter illustrates the method's ability to efficiently evaluate various cases, and find the model that adheres to the requirements that will be explicitly defined in following sections of this chapter.

## 5.2 Problem definition

To quantify the performance of a cavity receiver, it is necessary for the implementation of this receiver to have some realistic heat flux input, as well as to apply the collected energy. Many options are available that include sufficient variables to perform a numerical analysis of cavity performance.

### 5.2.1 Power source

A proposed application is the Helio100 heliostat field (Figure 5.1) in Stellenbosch, South Africa, which is run by the Solar Thermal Energy Research Group (STERG). This facility has a number of solar-collecting resources, all of which are well documented (S.T.E.R.G., 2017). This heliostat facility can produce approximately 100 kW of energy, and was designed so that a power cycle, known as SUNSPOT, can be connected to this receiver. This cycle includes a number of subsystems, such as a Brayton cycle gas turbine and energy storage in the form of a packed rock bed.



*Figure 5.1: Helio100 (S.T.E.R.G., 2017)*

As the scope of this dissertation does not include field optimisation, the actual layout of the heliostat field is not considered, and only the power output of a field such as this is considered. As a simplification of the heliostat field, it is assumed that a parabolic dish receiver is used in the MCRT simulations, with an aperture diameter that is determined by the total amount of energy required by the system.

It is also assumed that the cavity is not inclined and has a glass window at the aperture as a convective loss minimisation tool. For future work, the effect of the discrete nature of the heliostat field and the additional convective losses due to the cavity being inclined can be considered (Pye et al., 2015).

### 5.2.2 Thermal cycle

A number of receiver systems have been implemented for utilisation in point-focus receiver plants. The proposed thermal cycle and receiver cavity for this numerical study is a Brayton cycle with a high-pressure air receiver (HPAR) cavity, as discussed in Chapter 2. Specifically, a tubular absorber arrangement will be used.

The working fluid in this system is high-temperature, pressurised air. The typical Brayton cycle, which is graphically represented in Figure 5.2, utilises the working fluid at this state most efficiently. The temperatures for the heating phase ( $2 \rightarrow 3$  in Figure 5.2) range from approximately  $330\text{ }^{\circ}\text{C}$  to  $800\text{ }^{\circ}\text{C}$  (Korzynietz et al., 2016), at which point the pre-heated air is passed into a combustion chamber ( $3 \rightarrow 4$  in Figure 5.2) and heated further to  $1\ 150\text{ }^{\circ}\text{C}$ , which is the required inlet temperature for the gas turbine. These values are used as a benchmark for determining the absorbed radiation heat flux in the cavity, with the assumption that air is the ideal gas. The outlet high-temperature air is used in a number of applications, including the preheating of the compressor air, thermal storage or routed to additional components, such as steam generators to improve overall system efficiency.

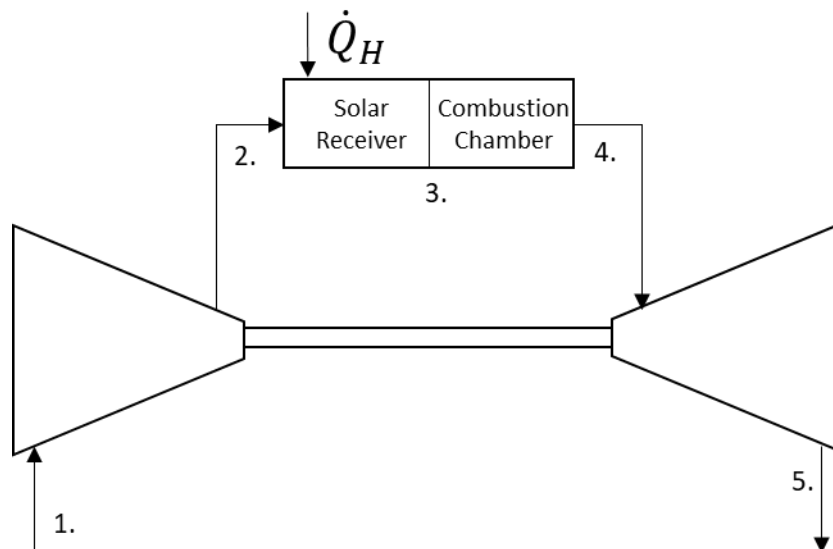


Figure 5.2: The Brayton cycle

Table 5.1: The variable states of a typical Brayton cycle (Korzynietz et al., 2016)

Location (Figure 5.2)	Temperature (°C)	Static pressure (bar)
1.	25	1
2.	330	10
3.	800	10
4.	1 150	10
5.	650	1

The family of geometries to be used is based on the optimised cavity that was previously presented (Pye et al., 2015). To have comparative results, this receiver is scaled so that it has the capacity to have similar performance characteristics to that of the pre-heater section of the HPAR system proposed by Heller for the SUNDISC Cycle (Heller et al., 2017).

To heat the HTF from 330 °C to 800 °C, from stage 2 to stage 3 (Figure 5.2), the flow rate of the working fluid is required. To ensure that the small-scale facility can provide sufficient energy to the proposed cavity, a surface area of 40 m<sup>2</sup> of mirrors is used to provide the concentrated energy at the receiver aperture. Using a DNI value of 1 000W/m<sup>2</sup>, the total amount of available energy from this area of the field is calculated to be 40 kW. Equation 5.1 is used to calculate the maximum mass flow rate required to transfer this energy as 0.08 kg/s, with  $T_i$  and  $T_o$  being the temperatures of stages 2 and 3, respectively, and the specific heat of air ( $C_{p,air}$ ) calculated at the average temperature between the stages.

$$Q_{HTF} = \dot{m}_{HTF} C_{p,air} (T_o - T_i), \quad 5.1$$

where:

$$T_i = 330 \text{ °C}$$

$$T_o = 800 \text{ °C}$$

$$C_{p,air} = 1\,061.03 \text{ J/kgK}$$

The above mass flow rate is calculated assuming that the overall system efficiency is 100%. Realistically, fully optimised systems achieve overall efficiencies closer to 70% and 80% (Behar et al., 2013). As this is the case, to achieve the correct outlet temperatures required for the correct operation of the Brayton cycle, an initial assumption of 70% efficiency, a mass flow rate of  $0.7 \times 0.08 \text{ kg/s} = 0.056 \text{ kg/s}$  will be specified. As overall efficiency is improved from the initial design, the flow rate of the HTF can be increased.

For implementation into full-scale Brayton cycle systems, mass flow rates that are far greater than the rate achieved in the proposed receiver would be required, depending on which turbine is selected and the requirements of the system (Korzynietz et al., 2016). The option exists of using multiple candidate receivers in parallel, which would then accumulatively provide the necessary mass flow rates.

The geometry used in this iterative performance investigation encompasses a number of design features seen in the case studies leading up to this chapter. This cavity shares similarities with the tubular cavity

receiver proposed in the SOLHYCO project (Ho and Iverson, 2014), as well as aspects from the helical cavity receiver proposed by John Pye (Pye et al., 2015). These similarities will be highlighted and discussed in the following paragraphs of this section.

The cavity, as seen in Figure 5.3, consists of a number of features that should be noted. As a method to limit the number of parameters that are the driving dimensions of this geometry, it is proposed that the cavity should always touch the sides of a bounding box, which is 1 m × 1 m in height and diameter. Since this makes the total height and maximum diameter constants, variables that will determine the parameters in Figure 5.3 are introduced, with equation 5.2 and 5.3 driving the pitch and inner diameter ( $D_i$ ) dimensions respectively.

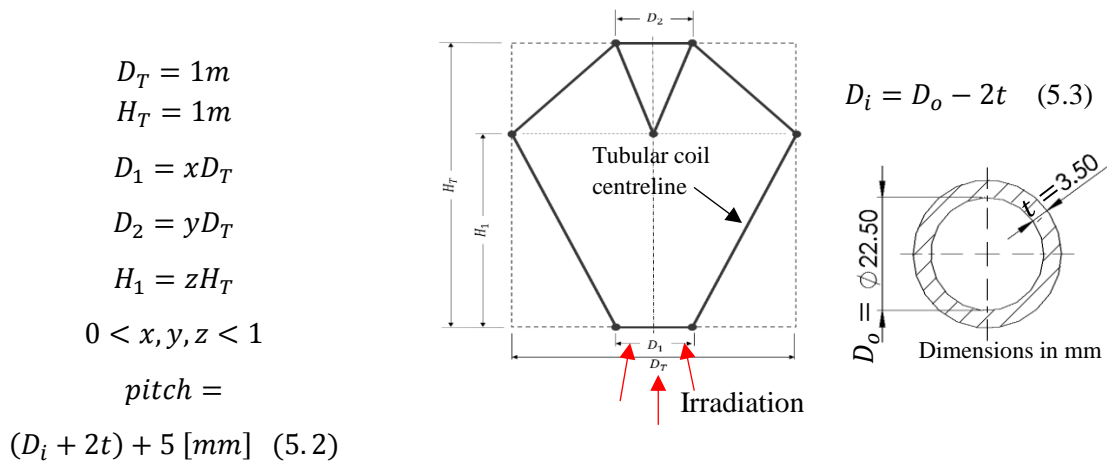


Figure 5.3: Parameterised cavity

The principle of this cavity is that it is made of two joined, tapered helices that form the top and bottom half of the receiving surfaces, tapering outwards and inwards, respectively. These tapers are based on the work of Pye (Pye et al., 2015) and attempt to enhance the amount of captured insulation while reducing the view factor of the inside absorber tubes to the aperture window. The absorber tube is also coiled as in the validation and Pye cases. The absorber tube surface area that is exposed to the incident radiation attempts to proportionally match that of the SOLHYCO tubular cavity receiver (Jedamski et al., 2010). This geometry also shares similarities with the SOLHYCO geometry, by potentially having the full surface area of the pipe exposed to radiation, as opposed to being partially covered by the insulation as in the validation case. By using reflective walls adjacent to the tube (Figure 5.4), it is possible to improve the uniformity of the heat flux distribution on the surface of the absorber tube, while also increasing the total amount of specular flux absorbed on the tube surface. The minimisation of temperature differences in the tubular wall will consequently reduce thermal stress.

From section 2.3.2, it became apparent that use of a glass aperture greatly increases the efficiency of the cavity receiver by minimising convective heat losses, and by enabling the greenhouse effect. In turn, this provides a simplification to the computational domain, as the unpressurised air in the cavity can be assumed as a solid for initial calculations. Buoyancy effects are neglected. The pane of glass is assumed to be 20 mm thick and will always be 40 mm below the origin of the geometry, the most negative coordinate the helical tube will reach. This can be more clearly visualised in the cross-sectional view of a sample geometry of the cavity receiver in Figure 5.4.

A conical section of the insulation with a reflective cover is placed in the cavity in such a way that incoming rays from the solar field are redirected towards the absorbing tubes rather than potentially striking the roof of the receiver. Its dimensions are governed by the diameter and height of the top helix. This implies that its vertical extent is linked to the vertical extent of the top helix. It was decided that this feature is a necessary addition to the geometry as initial testing without this surface showed energy losses of  $\sim 33\%$  back through the aperture window. With this addition, surface losses were decreased to less than  $2\%$  of incoming radiation, which is considered much more acceptable. Of course, in real-world applications, the design may be limited by the surface of this body becoming hotter than the material may be able to handle, but theoretically, since it will need to be highly reflective, this should not be the case. If this were to occur, it would be noted, but it is assumed that future designs will be able to overcome these potential drawbacks.

The insulation covering the tubular absorber is always set to be  $40\text{ mm}$  thick, as well as  $40\text{ mm}$  away from the absorber tube centreline at all points in the cavity. As can be seen by the final representation of a candidate geometry in Figure 5.4, this will cause the insulation covering to be  $160\text{ mm}$  in diameter larger than that of the widest part of the spiralled tube centreline.

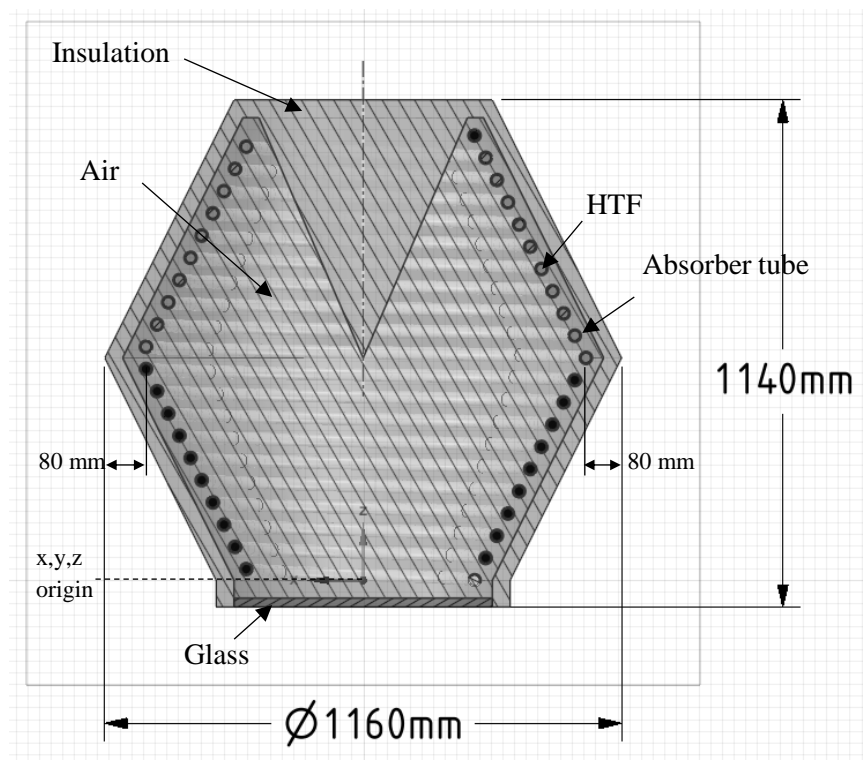


Figure 5.4: The candidate tubular high-pressure air receiver geometry with bounding box dimensions

### 5.2.3 Objective function

To determine which version of the geometry has the superior performance, a number of methods to measure the efficiency of each proposed geometry is required. The performance criteria are based on the methodology discussed in section 2.4, and therefore include the quantification of optical and thermal efficiency, as well as the evaluation of the outlet temperature value.

Figure 5.5 depicts the process followed to determine performance with the geometry defined using specific parameters as shown in Figure 5.3. Once the parameters have been set and the geometry

adjusted, it is meshed and processed to be interpreted by SolTrace to perform the optical simulation and ANSYS Fluent to perform the numerical conjugate heat transfer analysis. The depicted process is not automated. Performance is assessed through inspection to decide on a new set of geometries for each successive iteration.

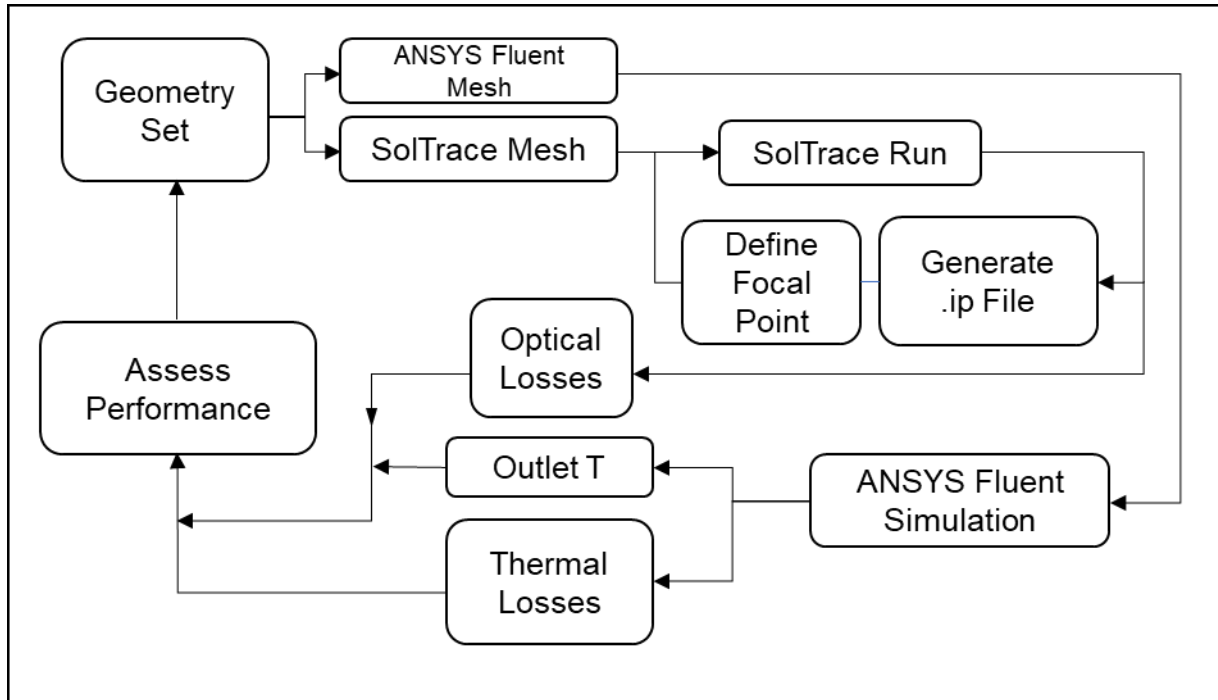


Figure 5.5: The iterative determination of the performance flow diagram

The optical efficiency of each geometry set, with variations in focal point, will be determined by the ratio between the number of rays absorbed by the absorber tube and the number of rays made available at the aperture window. The simplest method of calculating this is given by Equation 5.4.

$$\eta_{opt} = \frac{rays_{aperture} - (rays_{ins} + rays_{lost})}{rays_{aperture}} \quad 5.4$$

Similarly, the thermal efficiency is calculated using the methods stipulated in sections 2.4.2 and 2.4.4 using ANSYS Fluent to quantify heat transfer at each boundary. These methods include the integral of total heat transfer on the surfaces of interest, such as the semi-transparent glass aperture, the outside wall of the insulation, and of course, the inlet and outlet of the pressurised HTF.

The temperature of the HTF at the outlet is also assessed. Although this value is included in the thermal efficiency considerations, it is necessary to determine if the required temperature is sufficient for use in the Brayton cycle. Since the HTF is considered an ideal gas, it is possible to determine the outlet temperature by calculating the mass-weighted average at the boundary of the outlet wall using ANSYS Fluent, since the flow is compressible.

Finally, the overall performance is assessed using the system efficiency that is calculated using Equation 5.5. Decisions made on which parameters drive the geometry to a more optimum solution are selected based on this method.

$$\eta_{sys} = \eta_{th} \times \eta_{opt} \quad 5.5$$

#### 5.2.4 Constraints

The determination of system performance cannot only be based on a few specified values, such as the temperature of the heat transfer fluid leaving the receiver after being exposed to the concentrated solar energy. In some cases, there may be negative aspects in the receiver geometry that should not be overlooked when moving forward with the design decisions. In a solar system, some critical aspects to consider are dictated by material limitations that will exist in the physical system. If temperatures exceed these values due to hot spots or the general absorption of energy, it may cause problems such as decreased lifespan, a decrease in performance, cracking or other thermal stress-related issues.

These aspects will need to be considered in geometry performance when advancing to the new parameter set in an attempt to produce a geometry that not only has the highest efficiency, but that will also require the least maintenance and sustain high performance.

### 5.3 Numerical setup

#### 5.3.1 Initial conditions

The specification of initial conditions is not always strictly necessary, assuming that there is a single solution point to which the simulation should converge. Since this is the case, it is valuable to specify initial conditions only to decrease potential solution time, as the solution begins closer to the convergence state of the simulation. For this set of simulations, the initial conditions are specified for the temperature and pressure in the high-pressure heat transfer fluid tube, 603 K and 10 bar =  $10^6$  Pa, respectively.

#### 5.3.2 Materials and properties

Material properties and geometric characteristics that will be used in the numerical geometry definitions are included in the following section. Properties are given so that they can be interpolated at different temperatures or as close to the temperature design point of approximately 330 °C to 800 °C. It is expected that internal temperatures in the receiver may be higher than this. Therefore, properties of air at this design pressure for temperatures of up to 1300K are included in the data. Geometric characteristics are also discussed in detail, particularly where industry has attempted to use performance-enhancing material combinations.

## Air

It has been assumed that air obeys the ideal gas law, which means that density is a function of both pressure and temperature. The data in Table 5.2 considers air at a design pressure of 10 bar. This pressure is introduced to the simulation by setting the operating pressure at  $10^6$  bar.

Table 5.2: Ideal gas properties of air at 10 bar (Sonntag et al., 1998)

$T$ (K)	$\mu$ $10^{-6}$ (kg/m · s)	$C_p$ (kJ/kg · K)	$k$ $10^{-3}$ (W/m · K)
<b>300</b>	18.6844	1.02184	26.654
<b>400</b>	23.1648	1.02162	33.542
<b>500</b>	27.1652	1.03513	39.8743
<b>600</b>	30.8523	1.05494	45.8968
<b>700</b>	34.2802	1.07721	51.6855
<b>800</b>	37.4943	1.10021	57.2923
<b>900</b>	40.5438	1.1224	62.731
<b>1000</b>	43.4514	1.14213	67.9689
<b>1 100</b>	46.2417	1.16032	72.9606
<b>1 200</b>	48.9274	1.17578	77.6461
<b>1 300</b>	50.7472	1.18234	82.3931

## Insulation

Insulation in a solar cavity receiver is subject to a range of requirements based on material requirements, such as the minimisation of thermal losses and costing. An insulation, tested in a number of solar receiver cavities, including the SOLHYCO receiver, can perform efficiently when used at temperatures such as those desired by the Brayton cycle proposed in this case study (Ebert et al., 2015). The proposed material does not come without limitations, as thermal cycling does lead to degradation due to thermal expansion and other thermal stress effects. It is assumed that this material can be sufficiently developed so that it overcomes the aforementioned shortfalls for this case study. The properties for insulation at design point in the documented testing (Ebert et al., 2015) are for a cavity receiver with an HTF inlet temperature and pressure of 600 °C and 10 bar respectively. Outlet temperatures range up to 800 °C. These operating conditions are similar to those that are expected in the candidate receivers of this case study, which are a good approximation. These properties are listed in Table 5.3. Notably, these values are for uncoated insulation surfaces only, and are therefore only applied to the outside wall of the cavity.

Table 5.3: Insulation material properties for use in high-flux receivers (Ebert et al., 2015)

Property	Value	Unit
$k$	0.1	W/m · K
$\alpha$	0.3	-
$\epsilon$	0.3	-
$C_p$	2 300	J/kg · K

### Tubing

Absorber tubes used in HPAR systems vary both in material and complexity. A recommendation for a new type of tube for use on the SOLHYCO project was a “profiled multi-layer tube” or profiled multi-layer (PML) tube (Jedamski et al., 2010) (see Figure 5.6). The tube consists of a high-temperature-resistant, nickel-based alloy as the outer layer, copper tubing as the intermediate layer and another chemical-resistant layer as the inner tube. Notably, the thickness of the materials used in this arrangement were 1 mm, 2 mm and 0.5 mm respectively. It was found that this concept greatly reduced the temperature variations in the tube wall, therefore reducing the thermal stress of the system. In the design of Jedamski et al. (2010), the inner pipe walls included spiralled surfaces to increase the turbulence of flow, therefore also increasing heat transfer rates between the absorber tube and the HTF.

However, the manufacture and use of this type of multi-layer pipe proved to be difficult and unreliable due to the variations of thermal expansion coefficients of the material (Jedamski et al., 2010). As a result, the implementation of this technology has been slowed, and application in a helical geometry will more than likely prove to be even more challenging.

With the results of this technology being considered, the material used in the numerical study will be unspiralled copper due to its high thermal conductivity and it will approximate the ideal performance of the PML tube.

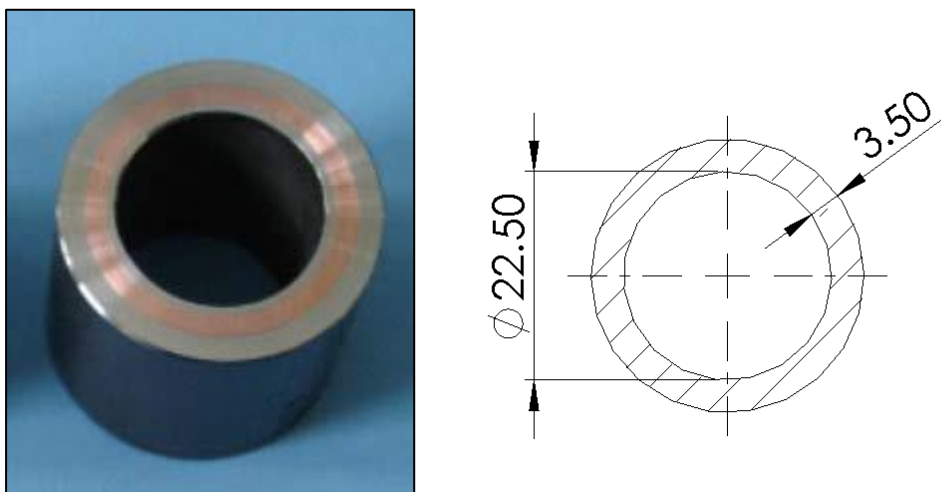


Figure 5.6: The PML tube with corresponding dimensions (Jedamski et al., 2010)

To account for the variance of resistance throughout the multi-layered tube wall while maintaining the use of a single homogenous tube, the effective heat conduction ( $k_{eff}$ ) through the wall is calculated as

245.93 W/mK with Equation 5.6. The conductivity values for copper and steel are 387.6 W/mK and 16.27 W/mK respectively.

$$\frac{\ln\left(\frac{r_o}{r_i}\right)}{2\pi L k_{eff}} = \sum_2^{x=n} \frac{\ln\left(\frac{r_x}{r_{x-1}}\right)}{2\pi L k_x} \quad 5.6$$

### Glass aperture

A widely used material as a glass aperture is manufactured from silica and commonly known as quartz glass. Its use is so wide due to its desirable optical and thermal properties at conditions that are experienced in a solar receiver system. These properties include almost negligible thermal expansion, thermal shock resistance and, of course, high transmissivity properties. Table 5.4 lists the properties of this glass at the design point parameter, where available. However, many properties are available as a function of their governing parameter, which is implemented in the numerical model. These properties can be found in the available documentation.

*Table 5.4: Properties of Heraeus's fused silica (Heraeus, 2017)*

Property	Value	Unit
Density	2 200	kg/m <sup>3</sup>
Transmissivity	0.92	-
Absorptivity	0.054	-
Emissivity	0.95	-
Specific heat	1 052	J/kg · K
Heat conductivity	2.68	W/m · K
Refractive index	1.52	-

In practice, the maintenance and cost of windows such as this can become costly and cannot be neglected from an economic viewpoint.

## Coatings

The application of a thin film to the surface of a material in a solar cavity makes it possible to change the material's optical properties with a negligible effect to the thermal properties. Coatings are not without their complications, which include high rates of degradation, maintenance and economic aspects. It is assumed that these aspects can be solved, and are not considered in this study.

A number of highly absorptive coatings are available or in development for use in solar applications. A coating used by the SOLHYCO project (Jedamski et al., 2010), known commercially as Pyromark 2500, is rated for use up to 1 000 °C. Under ideal conditions, this coating has shown absorptive levels of 0.96 to 0.97. Ho et al. (2012) experimentally determined emittance levels of 0.80 to 0.89 between 100 °C and 1 000 °C. By means of curve fitting, they determined the emittance dependency on temperature for Pyromark 2500 (Figure 5.7).

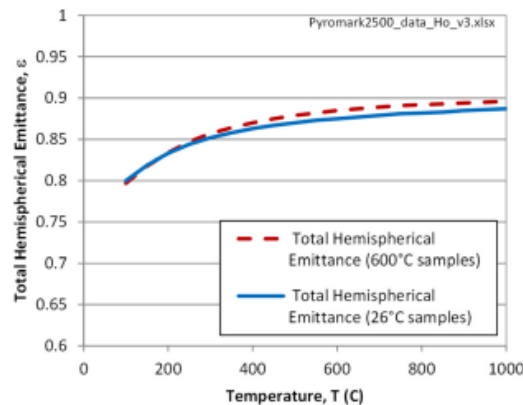


Figure 5.7: The total hemispherical emittance as a function of temperature for Pyromark 2500 (Ho et al., 2012)

Although performance varies slightly due to temperature, and is known to decrease if temperatures exceed 650 °C, it is assumed that there is no degradation in the material performance. As a conservative estimate, the total hemispherical emittance is modelled as the constant value of 0.85.

Additionally, a highly reflective coating on the inside wall of the insulation is proposed. According to a study by NREL (Jorgensen, 1993), a number of methods or materials that can be used to add a reflective property to a cavity wall include polymerised metallic paint and, in some cases, thin glass mirrors. Some coated surfaces were able to achieve a reflectivity of more than 95%. The addition of this coating will increase the system's overall efficiency by allowing the distribution of heat flux over the full surface area of the absorber tube, thereby minimising thermal stresses due to the formation of hot spots or large temperature gradients between the front and back sides of the tube.

### 5.3.3 Boundary conditions

For all surfaces that are included in this simulation, if the boundary is not considered a coupled wall, it may be subject to additional physics that may need to be accounted for. The following section discusses these specific boundaries in more detail. However, the following standard conditions in

Table 5.5 are used where appropriate.

Table 5.5: General atmospheric properties

Parameter	Value	Unit
$T_{amb}$	298.15	K
$P_{atm}$	1	bar
$T_{sky}$ (Equation 5.7)	270	K

### Inlet and outlet

As discussed in section 5.2.2, the goal is a mass flow rate of 0.056 kg/s. The flow of high-pressure air, specified as a mass flow rate inlet boundary condition, will have an initial temperature of 603 K, and a gauge pressure of 0 Pa. An outlet pressure boundary condition is used to set the downstream gauge pressure at 0 Pa.

To ensure the correct definition of density, the operating pressure is specified as  $10^6$  Pa, as discussed in section 5.3.2. Pressure drop is measured at the outlet of the tube, and as an evaluation, compared with the experimentally determined pressure drop of approximately 0.25 bar measured by Jedamski et al. (2010) in the SOLHYCO project.

### Insulation of the outside wall

The boundary condition on the outside surface of the cavity has mixed heat transfer mechanisms applied to it. This surface experiences convective and re-radiation heat losses that need to be accounted for. It is assumed that the ambient conditions are at 25 °C and that an approaching wind effect, which causes external forced convection heat transfer, is represented by a constant heat transfer coefficient for all simulations, which allows for the prediction of performance on a typical summer's day. As a simplification, the heat transfer coefficient is estimated as  $15 \frac{W}{m^2K}$ , as discussed in section 2.3.2 (Fang et al., 2011).

A number of methods have been used in the prediction of the radiative temperature of the sky. These models consist of predictions that depend on various, factors including cloudiness, dew point temperature, ambient temperature and cloud emissivity. For this case, the calculation of  $T_{sky}$  is simplified as given in Equation 5.7 (Moghimi et al., 2015).

$$T_{sky} = 0.0522 \times T_{amb}^{1.5} \quad 5.7$$

### Glass aperture

As in previous simulations, the glass aperture will be modelled as a semi-transparent wall. Consequently, it will be a significant avenue for re-radiation losses. The convective heat transfer coefficient, as well as the absorption coefficient, is based on values acquired from the quartz glass manufacturer catalogue (Heraeus, 2017) that can be found in Table 5.4. As discussed in section 2.8.3, to account for various wavelengths of electromagnetic waves due to re-radiation effects, non-grey material approximations are introduced using the DO method. This allows for variation in the absorption coefficient, absorptivity and emissivity of a material and the respective surfaces to vary

depending on the wavelength of radiation intersecting the body. In the two bands, the cut-off wavelength is implemented as  $2.7 \mu\text{m}$  from the approximation depicted in Figure 5.8. The absorption coefficient is determined to be  $30 \text{ m}^{-1}$  and  $450 \text{ m}^{-1}$  respectively, also depicted in Figure 5.8. The glass definition is therefore almost opaque at wavelengths above  $2.7 \mu\text{m}$  and is nearly fully transparent at a lower wavelength band.

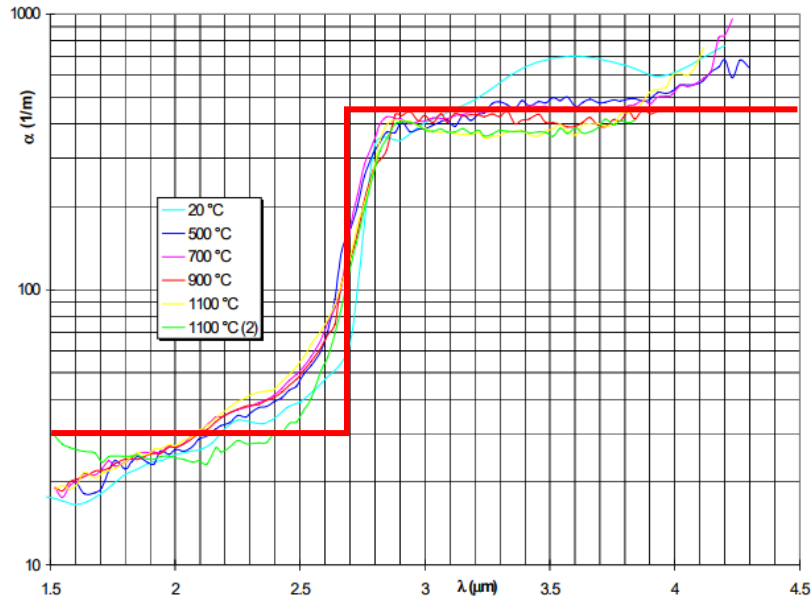


Figure 5.8: Absorption spectra of Philips 441 glass (Loenen and Van der Tempel, 1996)

From this, it is possible to calculate surface absorptivity as defined in Equation 5.8 (Modest, 2013):

$$\alpha = 1 - \tau = 1 - e^{-\kappa s} \quad 5.8$$

For a window with a thickness of 20 mm this will correspond to absorptivity values of 0.45 and 0.9998 for each band, respectively.

### 5.3.4 Solver setup

Flow rates in the cavity are specified so that the minimum flow rate of high pressure through the tubular receiver achieves Reynolds numbers far above the minimum requirement of 10 000 for the definition of turbulent flow. As such, a turbulent flow solution model is used. In this case, the  $k - \omega$  Shear Stress Transport (SST) model is used because it has proven to provide consistent solutions from previous cases (Craig et al., 2016b). In an attempt to stabilise solution outputs, a coupled solver is used with the pseudo-transient feature enabled. To speed up the solutions being solved, the Simple Solver is used first. It is then swapped for the coupled solver to enhance stability.

### 5.3.5 Convergence criteria

Convergence of the solution is determined by the residual output, which can be read from a graphic output in the ANSYS Fluent solver. These values are required to be as small as possible, determining the accuracy at which the solution has been solved. Levelling out these lines is indicative of the solution reaching its best possible accuracy.

The steady state of outlet temperature is also monitored in an attempt to determine the state of convergence in the model. For a solution to be considered converged, this value needs to remain unchanged or to level out for a number of iterations in a row.

### 5.3.6 SolTrace

The SolTrace setup used for this set of simulations differs slightly from the validation case of Chapter 4, which was used to prove certain parameters of the numerical simulation that will need to be matched or bettered to ensure the accuracy of the simulation. The number of elements needed to accurately represent the simulation and number of rays generated to reach SolTrace simulation convergence are consistent with the conclusions from section 4.5. This is at a minimum of 300 000 rays, with a cell density of 230/cm<sup>2</sup>. However, it was determined that the generation of 2 000 000 rays is required to ensure the interpolation convergence. To achieve this, a large number of simulations were run using different random number seeds due to SolTrace's memory limitations. Results from a number of different runs are acquired and concentrated together.

Since heliostat field power generation is being replicated, it is not necessary to incorporate the shadowing effect caused by the actual cavity and mounting systems, which would usually lead to a decrease in the optical efficiency of a solar dish concentrator. In SolTrace, the following two methods circumvent the shadowing effect of a cavity receiver at the focal point:

- Increase dish size to increase captured radiation, which replaces the aperture area covered by shadow
- Have multiple stages that are intersected in chronological order

Due to the limited library of geometry options in the SolTrace environment, it is necessary to use various stages to simulate the cavity receiver accurately, (see Figure 5.9). The multiple stage descriptions are given in Table 5.6.

Table 5.6: Stage descriptions used in SolTrace simulations

Stage	Description
1.	7.13 m diameter reflective parabolic dish, focal point = 20 m
2.	Two refractive circular plates 20 mm apart, representing the glass aperture top and bottom surfaces
3.1	Insulation cones and internal cone
3.2	Bottom flat plate, $\alpha = 1.0$ , simulating the glass aperture
3.3	Multiple circular elements representing the absorber tube

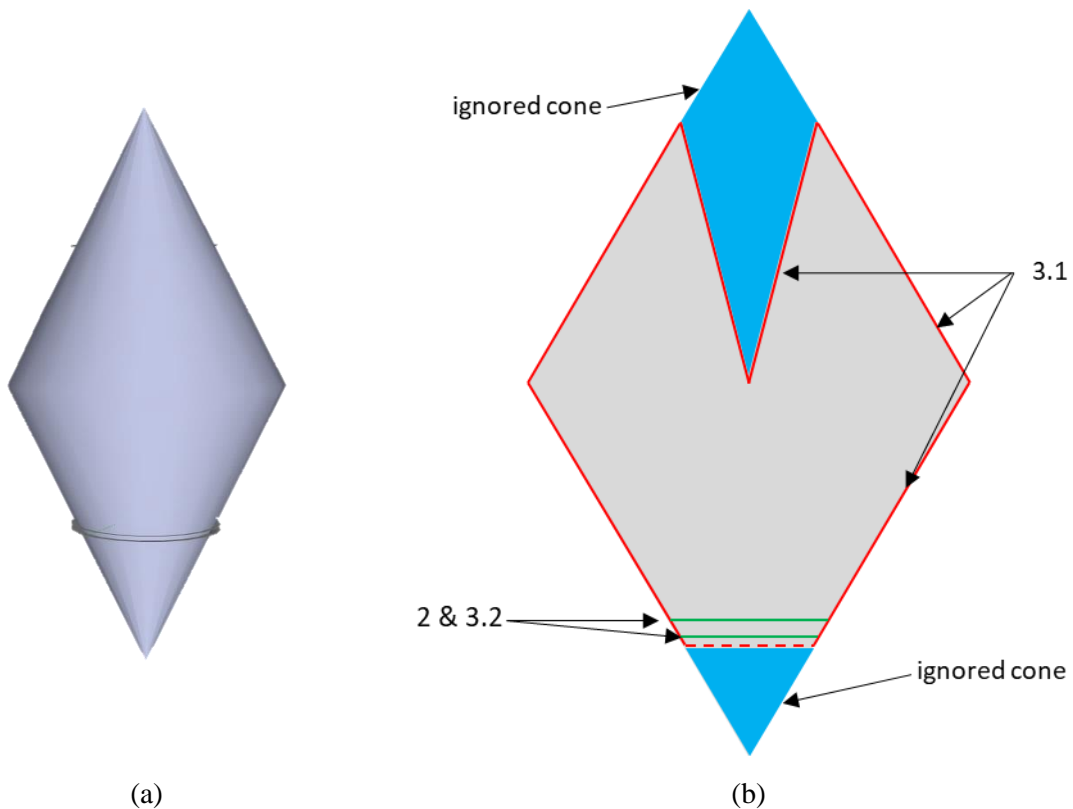
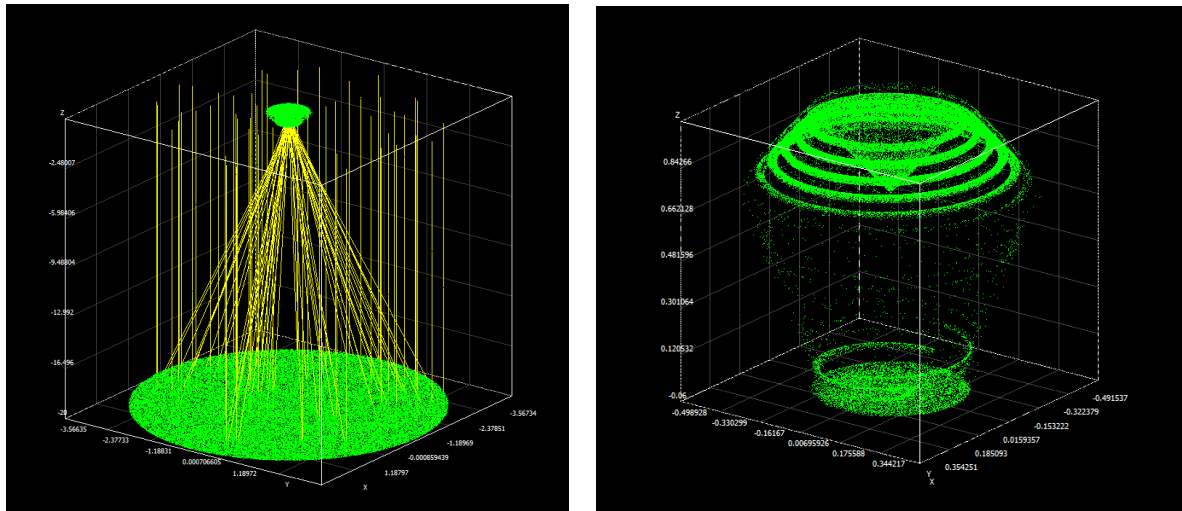


Figure 5.9(a): SolTrace receiver geometry; and (b): detailed sectional view used for iterative cases

It is possible to reproduce the desired shape of the candidate receiver by multiple stages to represent the geometry. The primitive shapes that are used to create this geometry are represented in Figure 5.9(a). To guarantee that the rays will not intersect the top and bottom of these respective cones, an aperture surface is created in the second stage. This stage allows rays to pass to the interior of the receiver, and only rays that have intersected this stage can progress to Stage 3. In Stage 3, two more surfaces are introduced to force the desired intersections in the receiver. These are the internal cone and the aperture surface, which lie coincident to the aperture surfaces created in Stage 2.



(a)

(b)

Figure 5.10: A candidate cavity receiver with: (a) a full system view; and (b): a detailed cavity view

At this point, it should be noted that the rays that have a final intersection with the insulation are disregarded in this simulation. Since the insulation walls are highly reflective, this value is minimised to a large extent, with absorbed energy making up less than 5% in the test cases run, as in Figure 5.10. To achieve more accurate results, these values can be patched to the insulation boundary in the subsequent CFD heat transfer simulation, using the profile patching methods described in section 3.2.2. The inclusion of this effectively lost energy will allow for a more accurate analysis of the formation of hot spots and re-radiation losses to the atmosphere.

### Focal point location

Shifting the focal point is a well-known technique used in point-focus, as well as line-focus systems to attempt to improve the overall efficiency of a solar receiver system. In this case study, by shifting the focal point to before the aperture and beyond it, as shown in Figure 5.11, variations in heat flux distribution will be achieved. These variations may result in decreased radiation and convective losses due to a shift in the temperature profile and improved heat flux distribution over the absorber surface area.

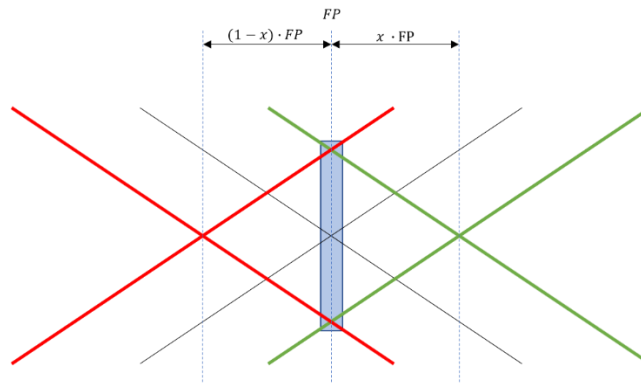


Figure 5.11: Variation of the focal point

The variation in focal point is governed by the aperture diameter and the rim angle ( $\theta_D$ ) of the dish, which is used to replicate the heliostat field. Equation 5.9 calculates this maximum variation.

$$\Delta FP = \frac{1}{2} D_1 \tan \theta_D \quad 5.9$$

For each geometry, three cases are run to determine at which point the focal point helps to improve the overall efficiency of the system. These three cases are run at the maximum offset allowed in both the positive and negative z-direction and at the 0-offset position.

## 5.4 Simulation implementation and results

For the iterative investigation, the parameterised geometry, as illustrated in Figure 5.3, is implemented in a number of simulations that are split into generations. These generations sequentially change certain parameters of the geometry in an attempt to investigate which arrangement provides the best overall performance according to criteria specified in sections 5.2.3 and 5.2.4.

Each ANSYS SpaceClaim-created geometry is passed through the workflow, as specified in Figure 5.5. This process is summarised as follows:

- The SolTrace-meshed surface is created from the absorber tubes and the MCRT is performed using 2 000 000 rays for each geometry and for each position of the focal point.
- A patchable heat flux distribution file is created using SolTrace scripting capabilities.
- A meshed 3D geometry is created and imported into ANSYS Fluent.
- Journal files are used to import all initial conditions, boundary conditions and material properties into the simulation.
- Interpolated UDFs are used to patch the SolTrace data to a UDM location in ANSYS Fluent.
- Residuals and outlet flow temperature are monitored to determine simulation convergence.
- Parameters of interest are extracted from the simulation data for post-analysis and comparison.

From the performance evaluation, the most promising design parameters are selected as the candidate parameters moving forward into the next generation of geometries.

### 5.4.1 First generation

For the first generation, the height of the helical coil  $H_1$  (Figure 5.3) was varied as a percentage of the total height of the cavity receiver. This parameter will effectively vary the view factor of the absorber tubes towards the aperture window, thereby increasing thermal efficiency by minimising re-radiation losses. Table 5.7 and Table 5.8 list all geometry variations and performances for the three changes in the position of the focal point.

Table 5.7: The first-generation geometry parameters and graphical representation

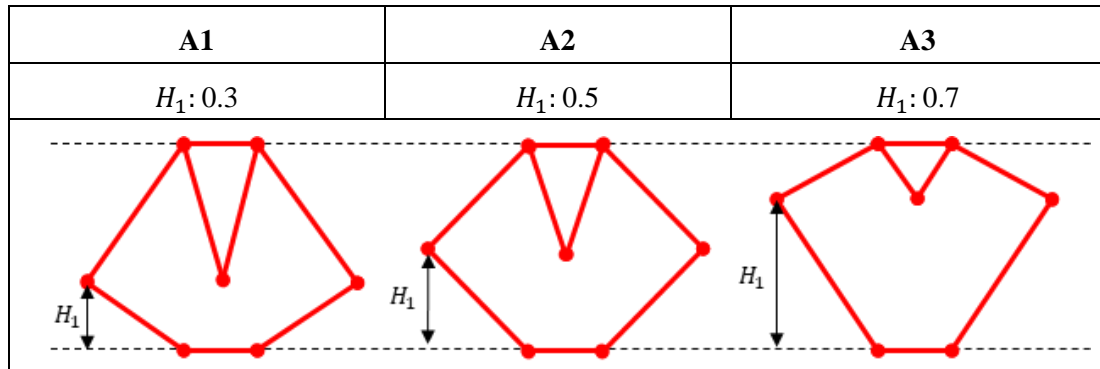


Table 5.8: The first-generation outlet temperature and efficiencies

Geometry	Focal point (FP)	$H_1$	$D_1$	$D_2$	$\Delta Q_{HTF}$ (W)	$\eta_{ther}$	$\eta_{op}$	$\eta_{overall}$
A1	Negative	$0.3H_T$	$0.5D_T$	$0.5D_T$	28 719	0.80	0.94	0.75
	Zero				29 402	0.80	0.88	0.70
	Positive				28 471	0.79	0.93	0.74
A2	Negative	$0.5H_T$	$0.5D_T$	$0.5D_T$	27 914	0.80	0.96	0.76
	Zero				28 493	0.79	0.91	0.72
	Positive				26 412	0.78	0.87	0.68
A3	Negative	$0.7H_T$	$0.5D_T$	$0.5D_T$	27 628	0.79	0.92	0.72
	Zero				28 691	0.79	0.84	0.67
	Positive				27 618	0.79	0.88	0.70

The geometry in Table 5.8 and the focal-point combinations that performed relatively better than their competitors are highlighted as potential candidates for promotion to second-generation candidate geometries. Most notably, two out of the three highest performers were achieved using a focal point that was shifted below the aperture window of the cavity. This effect is further illustrated upon reviewing the relative optical and thermal performance of the candidate geometries (see Figure 5.12(a) and 5.12(b) respectively). Change in performance between candidate geometries, particularly between A1 and A2, are relatively consistent when compared. This indicates that even with a change in geometry, the performance of this receiver strongly depends on the position of the focal point.

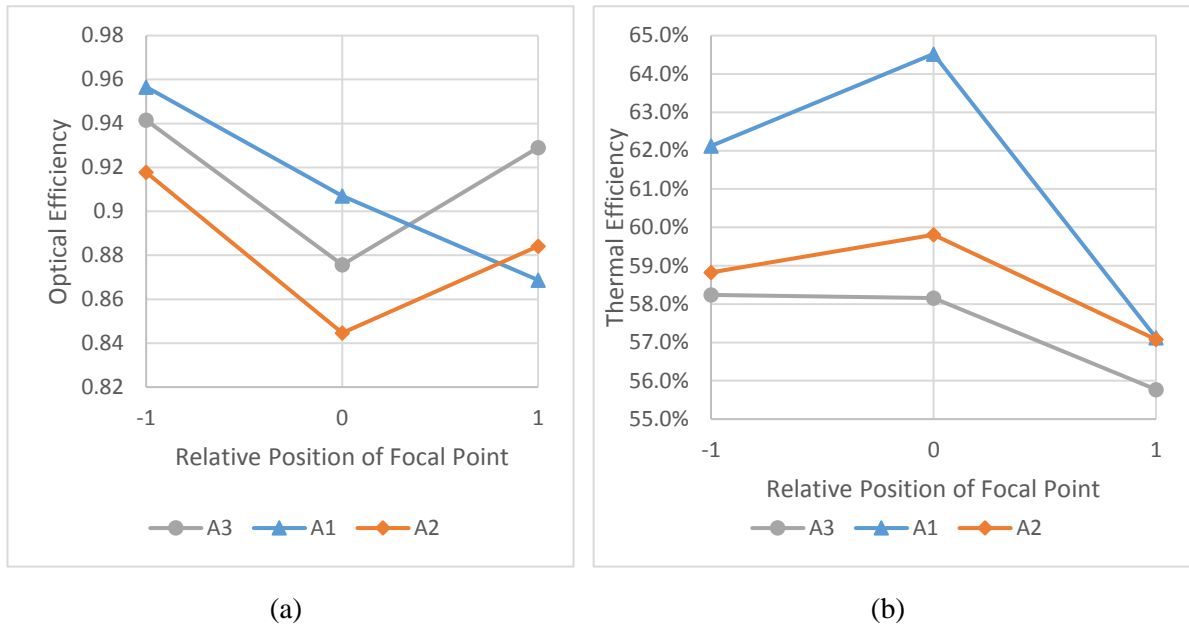
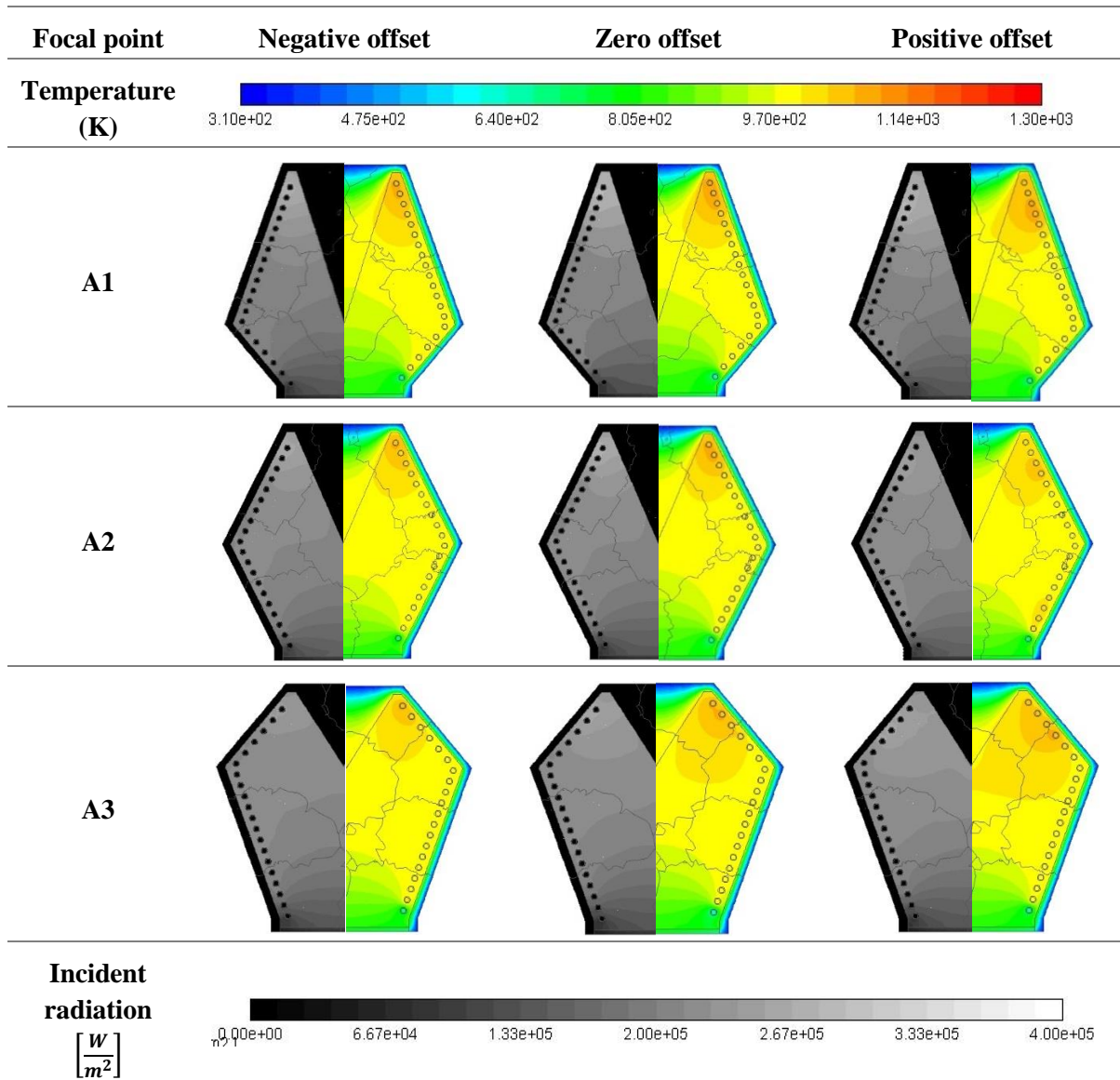


Figure 5.12(a): Optical efficiencies; and (b): thermal efficiencies for a first-generation receiver with variation in the focal point

To further investigate these performance variations, attention is shifted to the temperature and incident radiation contour distributions summarised in Table 5.9 for all simulations performed for first-generation receivers. From these results and the corresponding temperature distribution plots in Figure 5.13, the following observations are made:

- A3's hottest surfaces have a larger view factor than other candidates, as illustrated by the higher temperatures at these surfaces, hence lower operating temperatures due to re-radiation heat losses.
- The view factor of the top helix and focal point has a significant effect on optical and thermal efficiency.
- The length of the included inner reflective cone for ray redirection affects the distribution of heat flux in the cavity. It appears that the longer spike tends to spread heat more evenly, particularly over the top helix absorber surfaces. An effect that may lead to lessened re-radiation losses from a decrease in hot spots will additionally decrease thermal stress in the material.

Table 5.9: Contour maps for temperature and incident radiation distribution for a first-generation receiver with variation in the focal point



What is further illustrated upon observing the temperature distribution data on the absorbing tube surface is the common trend between all geometries and focal-point simulations and the gradual increase in tube surface temperature, until a section approximately 0.3 m to 0.7 m of the cavity height. Here the temperature effectively remains unchanged, at which point there is a sharp rise in the temperature of the tube as the highest flux distribution is concentrated in this vicinity. This effect should be minimised in future geometry simulations if possible due to the inefficient heat transfer and increased losses that will result. Candidate A1 is slightly less inclined to this sharp rise in temperature, and could perhaps be minimised further with some parameter adjustment.

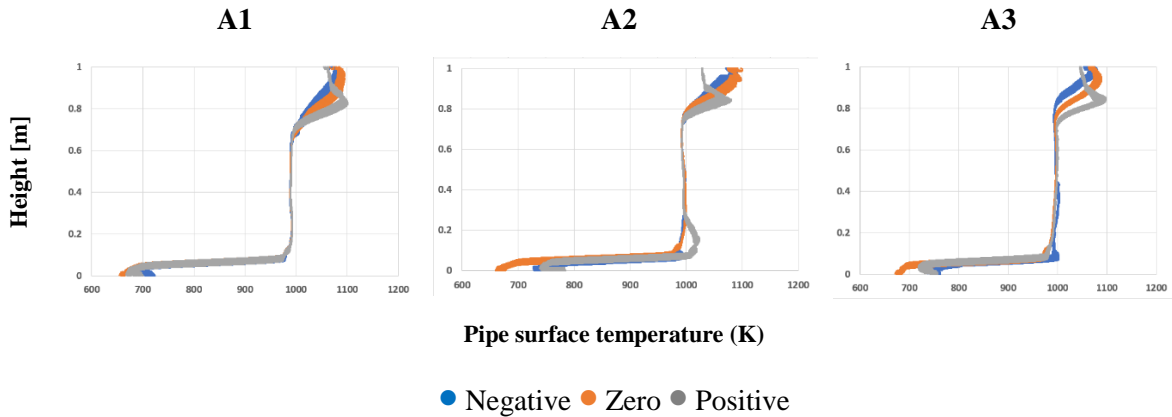


Figure 5.13: Variation of absorber tube surface temperature vs cavity height with a variation in focal point

From previous discussions, the two candidate geometries that hold the most potential for being identified as the most efficient are A1 and A2. Further investigation can be conducted into heat transfer mechanisms experienced by the geometry, as well as how this translates to the outlet temperature of the HTF (see Figure 5.14). The following is deduced from these results:

- The poor performance of A3 is verified and the view factor hypothesis strengthened by the relatively large radiation losses through the aperture window when compared to other candidates.
- Geometry A1 and A2 dominate as the two best-performing geometries, with the lowest thermal losses and highest heat transfer to the HTF.

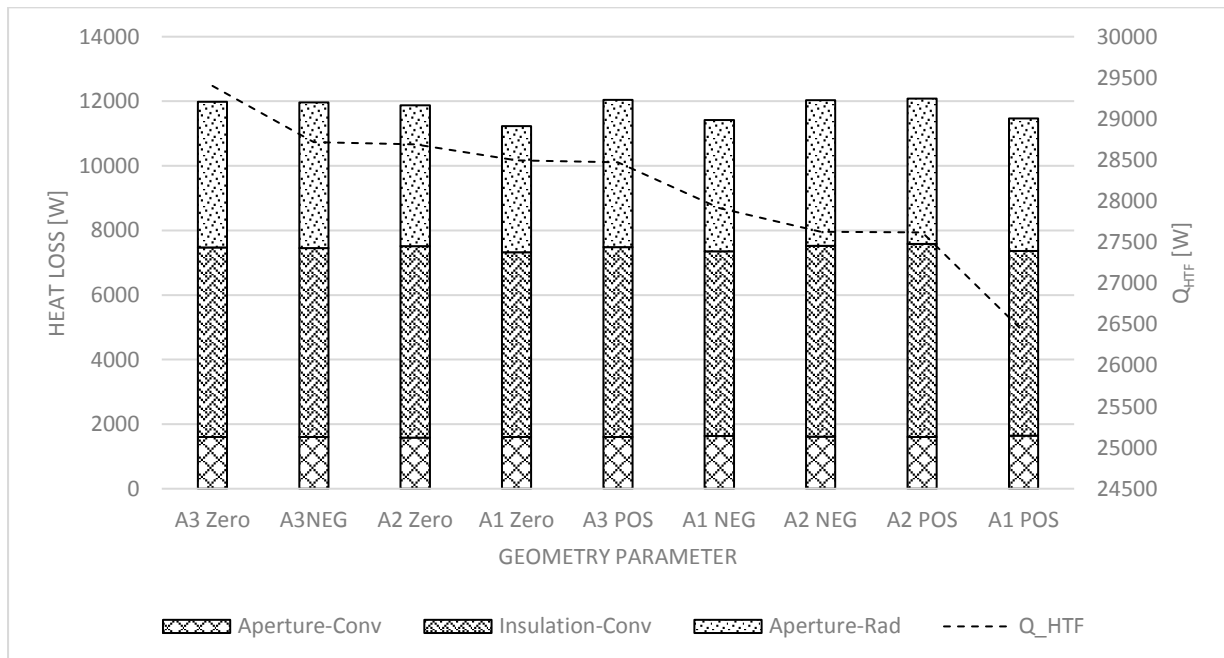


Figure 5.14: Heat loss with corresponding heat transfer to the HTF for first-generation receivers

As a final check on candidate geometry performance, the maximum temperature of components in the receiver is plotted in Figure 5.15. Since A1 and A2 are identified as the top-performing candidates,

these results are highlighted to further narrow the variation in candidate points. Notably, the A2 geometry has the highest maximum temperatures, highlighted in red and orange, with all other candidates being approximately equal or substantially below the highest temperatures seen.

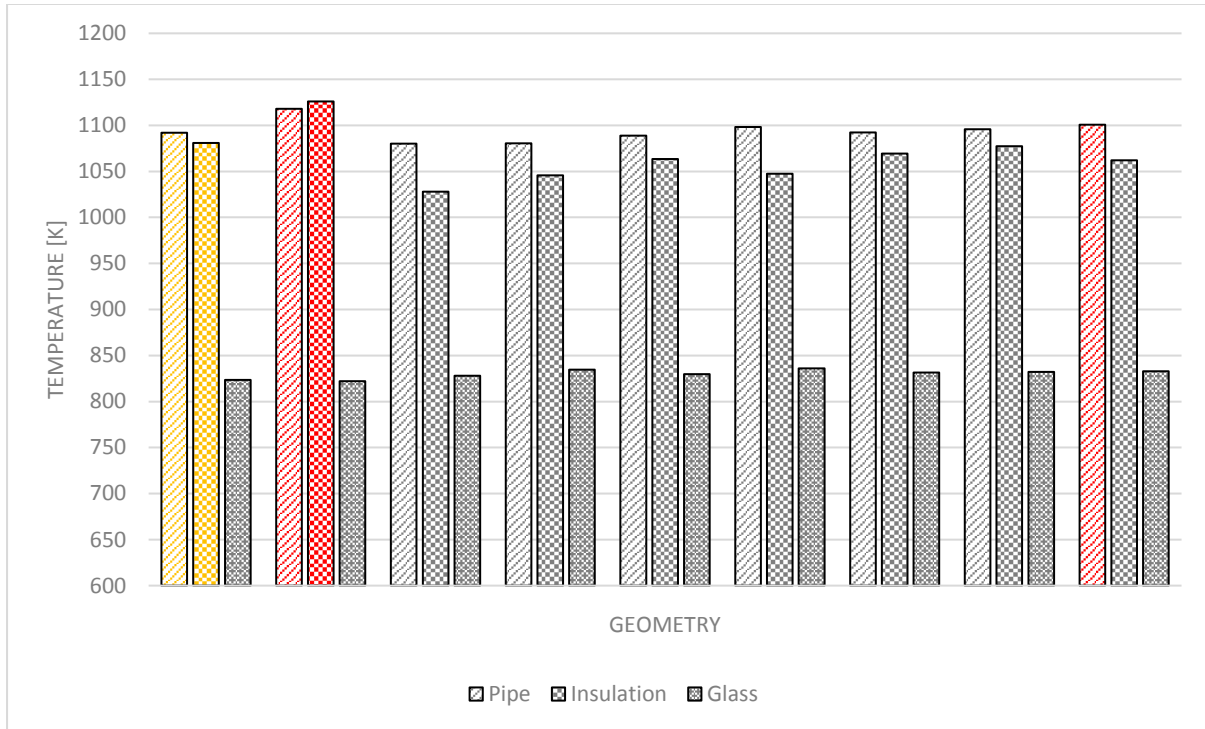


Figure 5.15: The maximum recorded temperatures for key components in first-generation receiver geometry

As a result, due to the lowest heat losses, and highest HTF heat transfer and efficiency values, the geometry candidate A1 is selected to advance to the second generation of simulations.

#### 5.4.2 Second generation

In this generation, the values of  $D_1$  and  $D_2$  are varied according to the values recorded in Table 5.10 and Table 5.11. These variations will change the size of the aperture window, as well as the taper angles of the two helixes that make the geometry.

Table 5.10: Second-generation geometry parameters and graphic representation

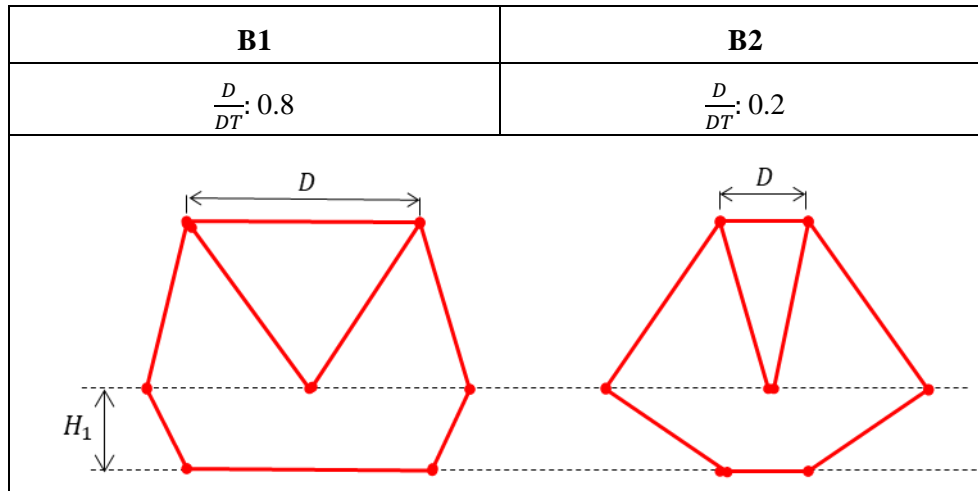


Table 5.11: Second-generation outlet temperature and efficiencies

Geometry	Focal point	$H_1$	$D_1$	$D_2$	$\Delta Q_{HTF} (W)$	$\eta_{ther}$	$\eta_{op}$	$\eta_{overall}$
B1	Negative	$0.3H_T$	$0.8D_T$	$0.8D_T$	27 478	0.36	0.88	0.31
	Zero				28 487	0.40	0.91	0.36
	Positive				28 343	0.38	0.76	0.29
B2	Negative	$0.3H_T$	$0.2D_T$	$0.2D_T$	32 092	0.65	0.95	0.62
	Zero				34 340	0.76	0.93	0.71
	Positive				36 100	0.66	0.92	0.60

From the results recorded in Table 5.11, as well as the corresponding optical and thermal efficiency graphs shown in Figure 5.16(a) and 5.16(b) respectively, the following initial observations are made:

- A large aperture window, candidate geometry (B1), allows for greater variation in performance when changing the focal point.
- A large aperture window, candidate geometry (B1), is susceptible to larger optical losses.
- The optical performance of a relatively small aperture window, candidate geometry B2, is more consistent with a change in focal point. This is due to the focal point's small relative change, according to the parameters of Equation 5.9.

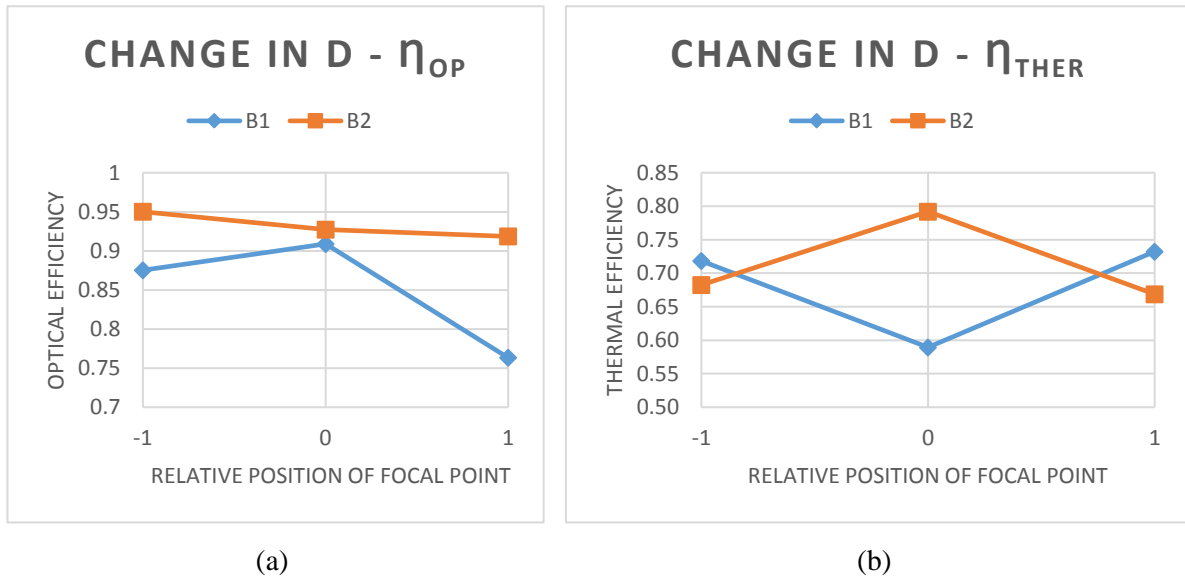


Figure 5.16(a): The optical efficiencies; and (b): the thermal efficiencies for the second generation with variation in the focal point

It is apparent from these initial results that changing  $D_1$  and  $D_2$  improves optical efficiency, while decreasing thermal efficiency, or it decreases optical efficiency, while improving thermal efficiency. As in the previous generation analysis, contour maps for both incident radiation and temperature are introduced in Table 5.12, and the corresponding temperature distribution on the absorber surface plots are introduced in Figure 5.17 to further understand the mechanisms that lead to the acquired efficiencies in Table 5.11. From this set of results, the following was observed:

- Candidate geometry B2 experiences large temperatures at the top of the receiver due to the high amount of incident radiation on surrounding surfaces.
- Large temperature differences between the top and bottom half of the receiver still exist in both candidates, but it is far more pronounced in B2, which increases experienced thermal stress.
- With a smaller aperture window, temperature distributions become more independent of focal point position.
- With a larger aperture window, the distribution of heat throughout the receiver is far more ideal, with a gradual increase in temperature along the curve length of the absorber tube for geometry B1.
- Higher temperatures in B2 lead to more re-radiation in the cavity. Incident radiation is more intense in the lower half of this candidate geometry when compared to that of B1.

Table 5.12: Contour maps for temperature and incident radiation distribution for the second-generation receiver with variation in the focal point

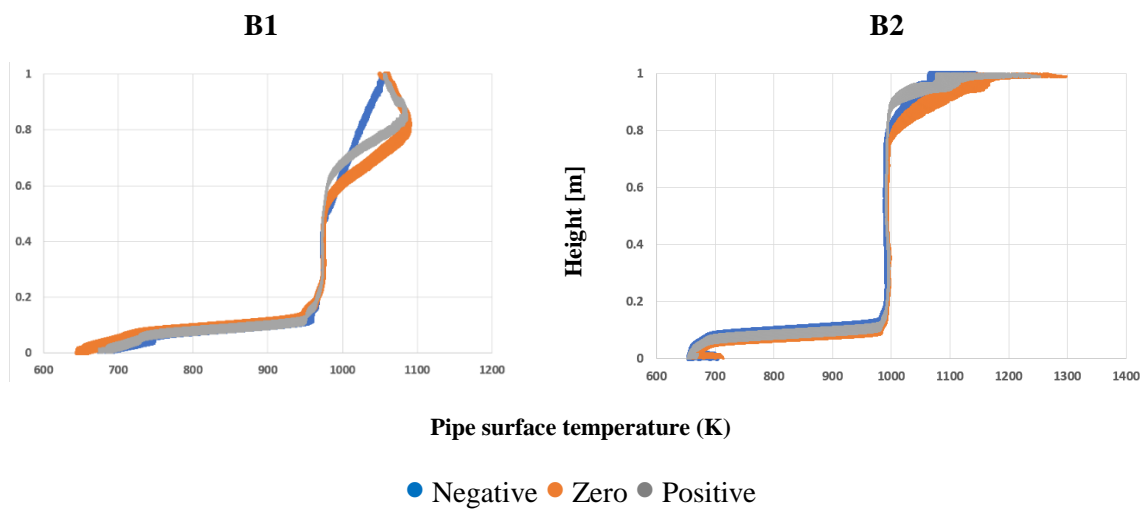
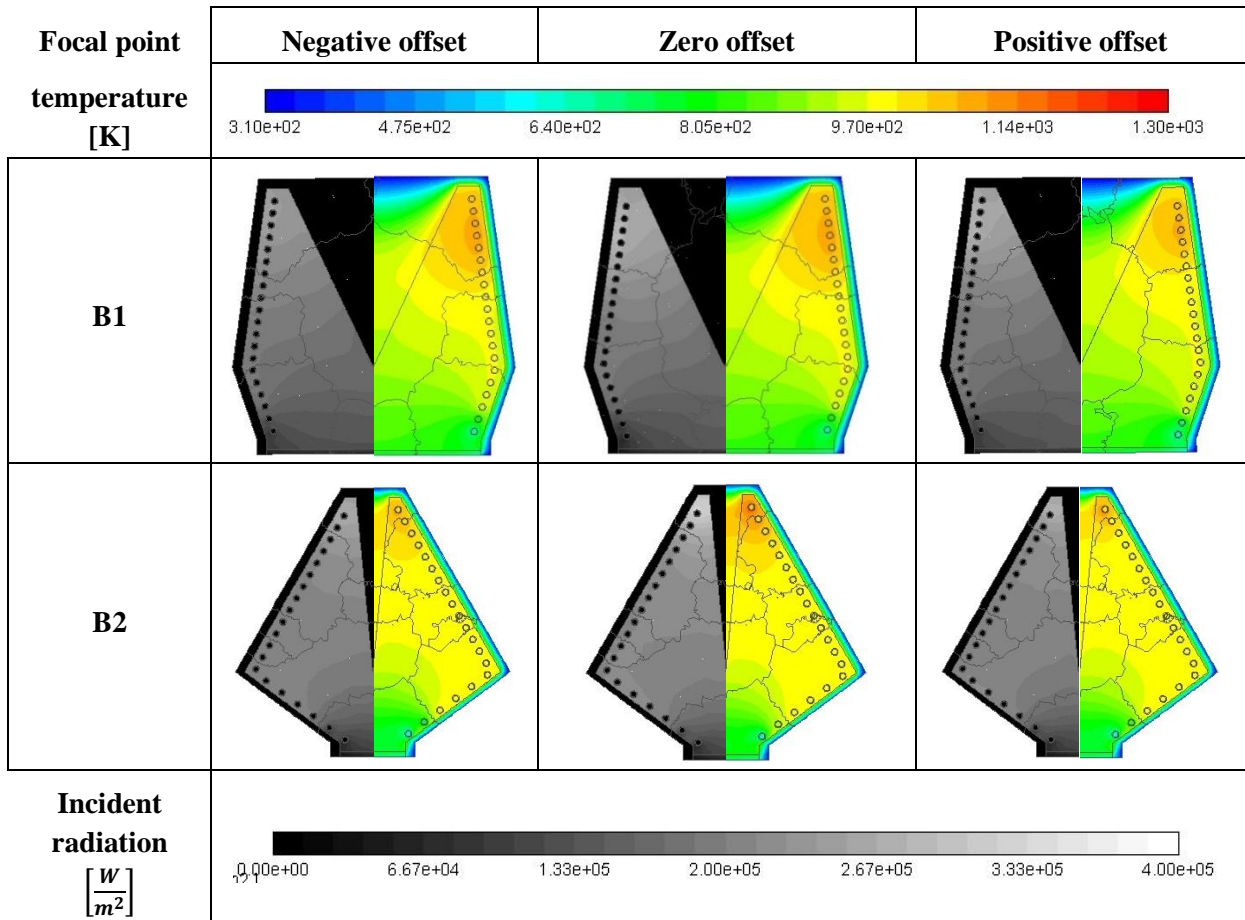


Figure 5.17: The variation of absorber tube surface temperature vs cavity height with a variation in focal point

To further analyse the cavity performance, Figure 5.18 compares each candidate's thermal losses and corresponding heat transfer to the HTF. These results allow the following deductions to be made:

- Even with elevated temperatures that may lead to re-radiation losses, the smaller aperture window of candidate B2 lessens the total radiation heat loss value.
- A larger aperture window will lead to higher re-radiation heat loss.
- Heat loss through the insulation led to the thermal inefficiencies experienced by receiver B2.
- Due to a better temperature distribution in receiver B1, convective heat losses were higher from the aperture window body, when compared to those experienced by candidate B2.

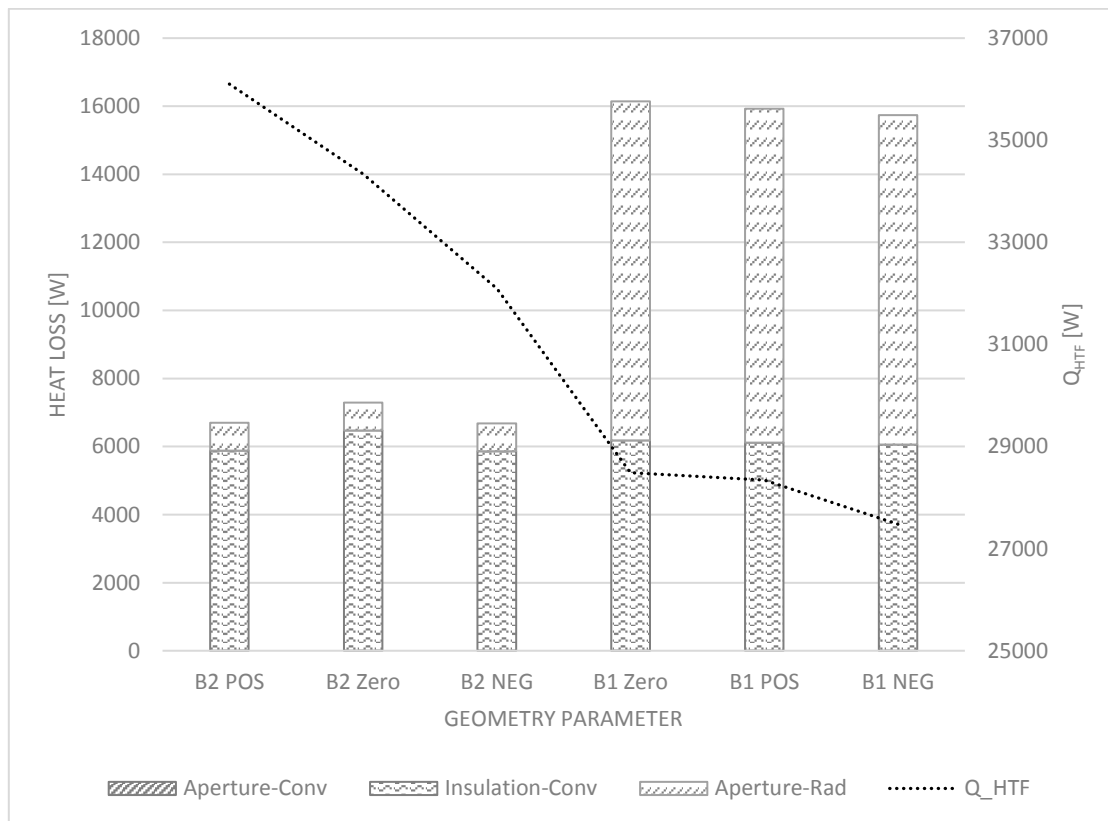


Figure 5.18: Heat loss with corresponding outlet temperature for second-generation receivers

As expected, the maximum temperature results (see Figure 5.19) show that candidate geometry B2 experiences largely elevated temperatures, beyond those that will be suitable for materials currently available for use in cavity receivers, as highlighted in red.

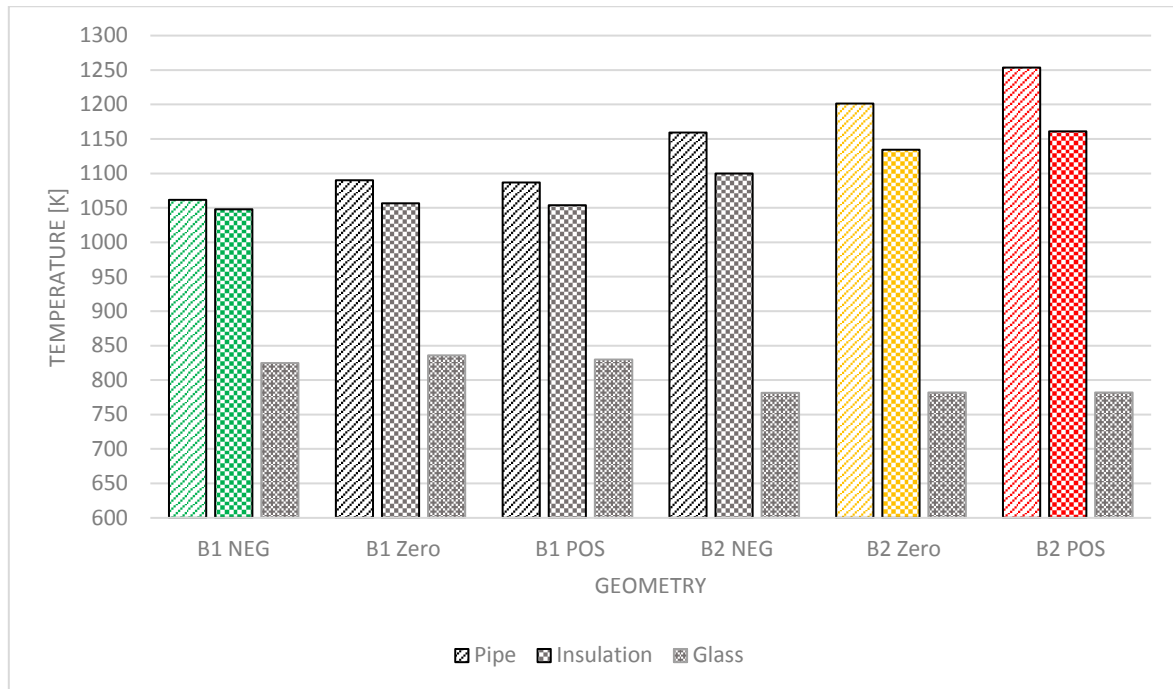


Figure 5.19: The maximum recorded temperatures for key components in second-generation receiver geometry

From the results discussed for the second generation of candidate receiver geometries, both B1 and B2 have their respective advantages and disadvantages. B1 performs well thermally, with acceptable heat distribution throughout the domain, operating temperatures within bounds of material limits and an outlet temperature within the range of what is required for a Brayton cycle. Due to the large aperture window, results are more inconsistent with a change in focal point. However, this can be an advantage if this cavity is used in an optimised heliostat field study, as it allows for greater parameter flexibility. However, this aperture size makes this candidate more prone to re-radiation losses.

Candidate B2 appears to have far more drawbacks than B1. Although optically it performs more efficiently, temperatures in the receiver are beyond those that are possible for current receiver materials. These elevated temperatures and the temperature distribution in the receiver leads to the formation of hot spots, accelerated material and coating degradation, and induces thermal stresses. Elevated temperatures such as these can be minimised by adapting the flow rate of the HTF through the absorber tube. More absorbed energy into the HTF and a higher flow rate will decrease the overall maximum temperatures throughout the cavity, decrease thermal losses and lower the outlet temperature of the HTF to the requirement of the Brayton cycle.

Since the overall performance of the second-generation receivers are similar, based on the above discussion, cavity B2 appears to have the highest performance moving forward into future generations. For significant improvement of the overall efficiency, these generations will require a more in-depth parameter study, perhaps using full optimisation methods. From the results, new parameters, such as flow rate and internal spike length, will need to be introduced to determine the effect on irradiation distribution within the cavity. A combination such as  $0.2D_1 : 0.8D_2$  is suggested as a future concept that may decrease re-radiation losses and improve temperature distribution throughout the domain.

## 5.5 Optimisation

From the process that is followed in section 5.4, it is apparent that improvements can be made on an initial candidate design, which improves the overall thermal and optical efficiency of the system by using methods proposed in this dissertation.

To provide a simple proof of concept, and due to the limitations in computational power that were available, three parameters, helix height, helix diameter and focal point, were chosen as variables to the iterative process that would have a notable effect on the system's performance.

With the proof of concept showing promising results, using only iterative methods, a full optimisation problem definition is proposed in this section, which will allow for refinement in the optimisation process and clearer identification of the quality of solutions and the performance of improvements by means of multidimensional response surface analysis.

Optimisation tools are available in the ANSYS Workbench environment. These tools allow for a streamlined problem formulation process (Ansys, 2011). Assuming that there would be an effectively unlimited amount of computational power and time available, this section of the dissertation lays out a full optimisation problem definition with the assumption of using the tools of ANSYS Workbench.

### 5.5.1 Design of experiments

The design of experiments effectively samples the design space, which is defined by specifying variables and their limitations and spreading statistically determined candidate points across the design space in an attempt to minimise model uncertainty. Although these parameters are numerous, the most likely to influence the solution are stated in Table 5.13, as well as their limitations. These limitations are based on those that have been determined in sections 5.2 and 5.3.

Table 5.13: Variables for use in the design of experiments

Variable	Description	Constraint
$T_{out}$	Outlet temperature of heat transfer fluid	$750\text{ °C} \leq T_{out} \leq 850\text{ °C}$
$T_{max}$	Maximum allowable temperature in the cavity receiver	$T_{max} \leq 1\ 000\text{ °C}$
$H_1$	Height of bottom helix in geometry	$0.5\text{ m} \leq H_1 \leq 3.5\text{ m}$
$H_T$	Total height of cavity receiver	$1\text{ m} \leq H_T \leq 4\text{ m}$
$H_{cone}$	Total height of cone	$H_{cone} \leq H_T$
$D_1$	Diameter of bottom helix	$D_1 \leq D_T$
$D_2$	Diameter of upper helix	$D_2 \leq D_T$
$D_T$	Total diameter of cavity receiver	$0.5\text{m} \leq D_T \leq 2\text{ m}$
$D_{cone}$	Diameter of cone	$D_{cone} \leq D_2$
$\dot{m}_{HTF}$	Mass flow rate of heat transfer fluid	$\dot{m}_{HTF} \geq 0.056\text{ kg/s}$



$d_{OD,tube}$	Outside diameter of tube	$10 \text{ mm} \leq d_{OD,tube} \leq 40 \text{ mm}$
$t_{tube}$	Wall thickness of tube	$2 \text{ mm} \leq t_{tube} \leq 7 \text{ mm}$
$t_{insul}$	Thickness of insulation	$40 \text{ mm} \leq t_{insul} \leq 100 \text{ mm}$
$t_{glass}$	Thickness of glass aperture	$5 \text{ mm} \leq t_{glass} \leq 40 \text{ mm}$
$\Delta p$	Pressure drop	$0 \leq \Delta p \leq 0.25 \text{ bar}$
$\Delta FP$	Focal point	$-\frac{1}{2}D_1 \tan\theta_D \leq \Delta FP \leq \frac{1}{2}D_1 \tan\theta_D$

### 5.5.2 Response surface and sensitivity analysis

Although not strictly necessary, determining the sensitivity of variables to others in the model can prove to be useful and time saving, particularly when there is a large number of variables in the definition of an optimisation problem.

There are a number of response surface methods to choose from. The response of the solution, which is determined from simulation results, appears to be stable, allowing for predictability in the response surface gradients. Since simulations are expensive, the most successful optimisation algorithms are expected to be either the sparse grid or Kriging response surface methods should be selected as candidate response surface methods due to the prediction of new candidate points being based on the current response surface data that is available, which will reduce the number of required simulations. With the increase in parameters, the solution may become non-linear, which is sufficiently handled by both methods.

Although more computationally expensive, the Kriging method offers a more reliable result, as the solution is forced to fit the provided datapoints as long as these points have been adequately selected with the appropriate density at areas of high gradient. As such, this is the most preferred method with which to proceed in a full optimisation process (Ansys, 2011).

### 5.5.3 Goal-driven optimisation

To determine system performance, one would need to define an objective function that would provide a goal towards which a solution can be driven. For this problem definition, two objective functions are identified to be maximised, as in Equation 5.10.

$$\max \eta_{thermal}(x_1, x_2, \dots, x_n); \max \eta_{optical}(x_1, x_2, \dots, x_n) \quad 5.10$$

This would require using a multi-objective optimisation algorithm. ANSYS has a number of these options from which to choose, such as the multi-objective genetic algorithm (MOGA) and adaptive multi-objective optimisation (AMO). Notably, it will not be possible to maximise both the selected objectives simultaneously. A common strategy to negate this drawback is to reduce the objective functions to one and generate a set of solutions known as the Pareto-optimal set. Although the multi-objective algorithms AMO and MOGA simulate this process, a proposed solution that was utilised in section 5.4 is to assess the overall efficiency of the system. This objective is expressed mathematically in Equation 5.11.

$$\max \eta_{overall}(\eta_{thermal}, \eta_{optical})$$

5.11

With the solution now defined with only a single objective, the adaptive single-objective optimisation (ASO) algorithm is recommended for use in the solution of the optimisation problem.

## 5.6 Conclusion

In two generations of candidate receivers, key design parameters for this sample geometry have been identified, using the novel numerical methodology of combining MCRT with FVM. Implementing an iterative method to determine candidate geometry performance has proven to be successful in efficiently improving on sample designs.

This methodology is proven to provide an efficient, accurate method to predict the performance of candidate geometry, and provides encouraging evidence for the confidence of implementation into full response surface optimisation methods.

# Chapter 6: Conclusion

## 6.1 Preamble

The aim of this study was to address the problem of determining heat flux distributions in point-focus cavity receivers.

A numerical model was developed by integrating MCRT and CFD to predict heat flux on a receiver surface, and to solve for the resulting conjugate heat transfer. Some of the important results and conclusions gained in this study include the following:

- I. The prediction of solar irradiation using purely CFD methods is extremely computationally expensive and time-consuming.
- II. Using MCRT and FVM can increase accuracy, while decreasing computational time and memory requirements.
- III. Accurate results can be generated by combining MCRT with FVM to predict the performance of solar power plants, for both point- and line-focus systems.
- IV. The developed methodology can be used to explore a large number of design points and optimise a base design timelessly and accurately without increasing computational cost.

## 6.2 Scope of future work

As indicated throughout the chapters of this dissertation, a number of simplifications and assumptions were made in an effort to determine best-practice guidelines for any future research. Exclusions from this dissertation's scope may be implemented in future to improve the accuracy of simulations and the overall relevance of the determined results.

### 6.2.1 Convective losses from cavity receivers

Quartz glass windows in receiver geometries are well known for being complex, while they need to be regularly maintained and are subject to overheating and cracking. Many projects and designs have considered excluding such windows to avoid their complications. However, this introduced the increase of convective heat loss from the cavity aperture.

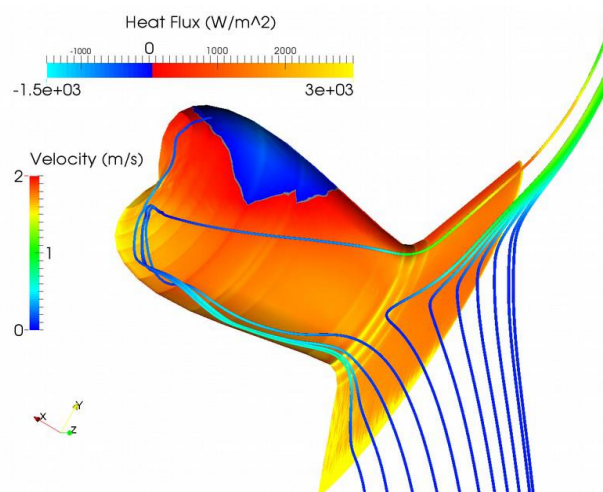


Figure 6.1: An open cavity receiver that experiences convective loss (Pye et al., 2015)

A number of researchers have conducted research into the effect of natural convection heat loss on cavity receivers. The work of Pye et al. (2015) is most relevant to this study, an example of which is illustrated in Figure 6.1. This highlights the effects of convective heat loss on the performance of these cavity receivers. The authors discuss how geometry parameters can be manipulated to minimise these effects.

### 6.2.2 SolTrace complex surface modelling

Up to this point, complex surfaces have been represented in the SolTrace domain by means of circles, with diameters large enough to ensure the coverage of the entire meshed, irregularly shaped element. Although this simplification has provided satisfactory results with acceptable accuracy, improvements can still be made by means of matching element with irregular shapes using the primitives of the SolTrace library.

Figure 6.2(a) and 6.2(b) are represented with an illustration of the shadow zone effect of the overlapping circular surfaces used to model the complex geometric surface, and how using irregular SolTrace elements can minimise these effects. Since SolTrace will intersect surfaces in chronological order of addition to the stage, rays will always intersect the surface that appears higher up in the chronological list. This shadowing zone causes errors in estimating flux distribution, which means that interpolation errors in ANSYS Fluent are exacerbated. With the changes recommended, this error is eliminated, due to the lack of shadowing. Therefore, the smudging of flux distribution is minimised and ray “leakage” is eliminated.

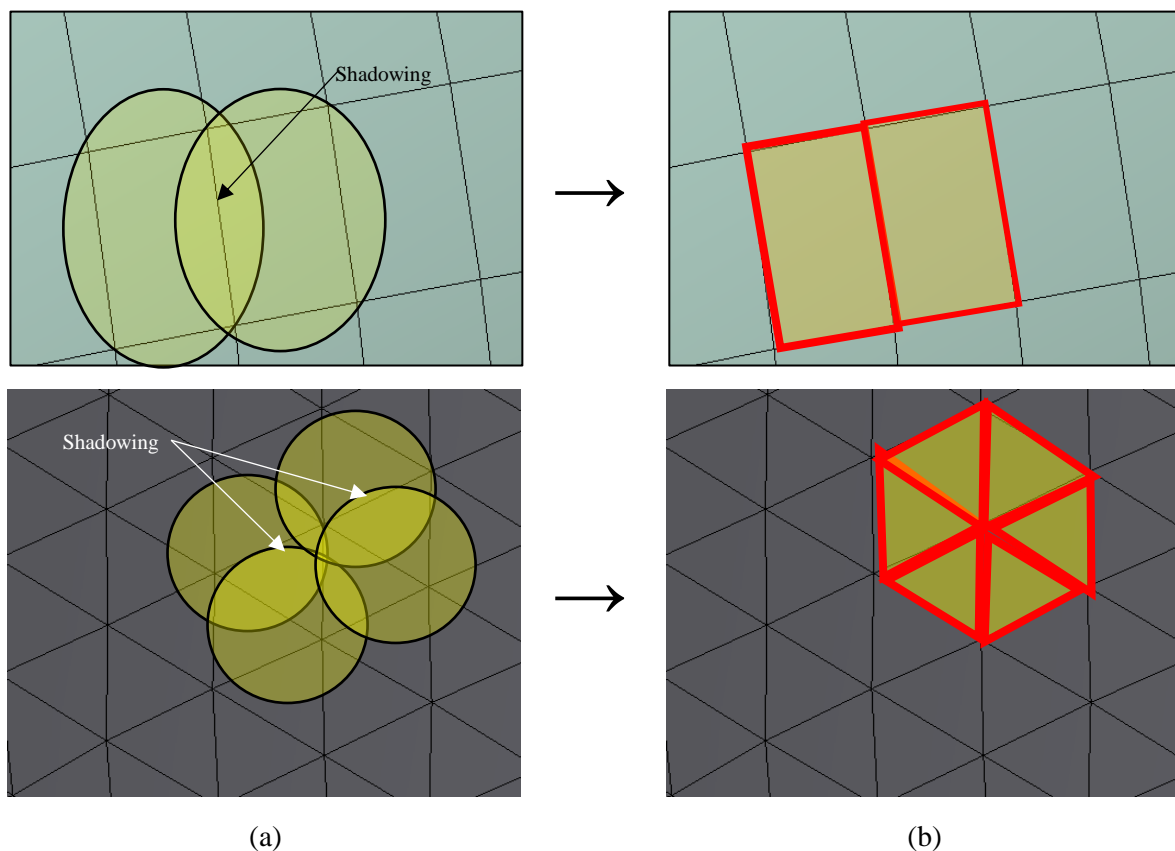


Figure 6.2(a): The shadowing zone due to circular elements; and (b): irregular quadrilateral elements used to minimise shadowing effects

### **6.2.3 Full optimisation study**

The iterative performance improvement methods used in Chapter 5 proved to be a powerful tool in determining the effect of candidate geometry in defining parameters on the performance of the receiver. More powerful still will be to incorporate the developed numerical method into a full multidimensional optimisation study, as discussed in section 5.5, which allows for a more in-depth study with larger parameter sets.

## **6.3 Conclusion**

A new methodology has been developed to investigate flux distributions in point-focus solar collector systems, which allows for future development and research in the University of Pretoria's Clean Energy Research Group.

# References

- ABENGOA SOLAR. 2018. *Abengoa Solar* [Online]. Available: [www.abengoasolar.com/web/en](http://www.abengoasolar.com/web/en) [Accessed 29 January 2018].
- ANSYS, A. F. 2011. 14.0 Theory Guide. *ANSYS inc.*
- ÁVILA-MARÍN, A. L. 2011. Volumetric receivers in Solar Thermal Power Plants with Central Receiver System technology: A review. *Solar Energy*, 85, 891-910.
- BEHAR, O., KHELLAF, A. & MOHAMMEDI, K. 2013. A review of studies on central receiver solar thermal power plants. *Renewable and Sustainable Energy Reviews*, 23, 12-39.
- BINDER, K. 1987. Monte Carlo Methods. *Quantum Monte Carlo Methods*, 241.
- BRIGHTSOURCE ENERGY INC. 2015. *Ivanpah* [Online]. Available: <http://www.brightsourceenergy.com/ivanpah-solar-project> [Accessed 22/02 2018].
- BROOKS, M. J., DU CLOU, S., VAN NIEKERK, W. L., GAUCHÉ, P., LEONARD, C., MOUZOURIS, M. J., MEYER, R., VAN DER WESTHUIZEN, N., VAN DYK, E. E. & VORSTER, F. J. 2015. SAURAN: A new resource for solar radiometric data in Southern Africa. *Journal of energy in Southern Africa*, 26, 2-10.
- BUCK, R., BRÄUNING, T., DENK, T., PFÄNDER, M., SCHWARZBÖZL, P. & TELLEZ, F. 2001. Solar-Hybrid Gas Turbine-based Power Tower Systems (REFOS)\*. *Journal of Solar Energy Engineering*, 124, 2-9.
- CENGEL, Y. A. & GHAJAR, A. 2011. Heat and mass transfer (a practical approach, SI version). McGraw-Hill Education.
- CHEN, H., CHEN, Y., HSIEH, H.-T. & SIEGEL, N. 2006. Computational Fluid Dynamics Modeling of Gas-Particle Flow Within a Solid-Particle Solar Receiver. *Journal of Solar Energy Engineering*, 129, 160-170.
- CHEN, J., MÜLLER-STEINHAGEN, H. & DUFFY, G. G. 2001. Heat transfer enhancement in dimpled tubes. *Applied Thermal Engineering*, 21, 535-547.
- CHENG, Z. D., HE, Y. L. & CUI, F. Q. 2013. A new modelling method and unified code with MCRT for concentrating solar collectors and its applications. *Applied Energy*, 101, 686-698.
- CRAIG, K. J., HARKNESS, A., KRITZINGER, H. & HOFFMANN, J. 2010. Analysis of AP1000 TM reactor vessel cavity and support cooling. *European Nuclear Conference*. Barcelona, Spain.
- CRAIG, K. J., MARSBERG, J. & MEYER, J. P. Combining ray tracing and CFD in the thermal analysis of a parabolic dish tubular cavity receiver. AIP Conference Proceedings, 2016b. AIP Publishing, 030009.
- CRAIG, K. J., MEYER, J. P. & LE ROUX, W. G. Computational fluid dynamics analysis of parabolic dish tubular cavity receiver. 2015. 3rd Southern African Solar Energy Conference, South Africa, 11-13 May, 2015.

- CRAIG, K. J., MOGHIMI, M. A., RUNGASAMY, A. E., MARSBERG, J. & MEYER, J. P. 2016a. Finite-volume ray tracing using Computational Fluid Dynamics in linear focus CSP applications. *Applied Energy*, 183, 241-256.
- DEPARTMENT OF ENERGY 2015. State of Renewable Energy in South Africa.
- EBERT, M., ARNOLD, W., AVILA-MARIN, A., DENK, T., HERTEL, J., JENSCH, A., REINALTER, W., SCHLIERBACH, A. & UHLIG, R. 2015. Development of Insulation for High Flux Density Receivers. *Energy Procedia*, 69, 369-378.
- EUROSTAT. 2015. *Renewable energy statistics* [Online]. Available: [http://ec.europa.eu/eurostat/statistics-explained/index.php/Renewable\\_energy\\_statistics#Electricity](http://ec.europa.eu/eurostat/statistics-explained/index.php/Renewable_energy_statistics#Electricity) [Accessed 20 July 2016].
- FANG, J. B., WEI, J. J., DONG, X. W. & WANG, Y. S. 2011. Thermal performance simulation of a solar cavity receiver under windy conditions. *Solar Energy*, 85, 126-138.
- GARBRECHT, O., AL-SIBAI, F., KNEER, R. & WIEGHARDT, K. 2013. CFD-simulation of a new receiver design for a molten salt solar power tower. *Solar Energy*, 90, 94-106.
- GEOSUN AFRICA. 2016. *Direct Normal Irradiation South Africa* [Online]. Available: <http://geosun.co.za/solar-maps/>.
- GHAZY, A. & FATH, H. E. S. 2016. Solar desalination system of combined solar still and humidification-dehumidification unit. *Heat and Mass Transfer : Wärme- und Stoffübertragung*, 52, 2497-2506.
- HAMILTON, J. 2010. *Careers in Solar Power* [Online]. Available: [http://www.bls.gov/green/solar\\_power/](http://www.bls.gov/green/solar_power/) [Accessed 22/02 2018].
- HAMILTON, J. & STATISTICS, U. S. B. O. L. 2011. *Careers in solar power*, U.S. Bureau of Labor Statistics.
- HARRIS, J. A. & LENZ, T. G. 1985. Thermal performance of solar concentrator/cavity receiver systems. *Solar Energy*, 34, 135-142.
- HELLER, L., ALLEN, K. G., LUBKOLL, M., PITOT DE LA BEAUJARDIERE, J.-F. P., GAUCHÉ, P. & HOFFMANN, J. 2017. The SUNDISC cycle: A direct storage-charging dual-pressure air receiver cycle. *Solar Energy*, 153, 435-444.
- HERAEUS. 2017. *Quartz Glass for Optics Data and Properties* [Online]. Available: [https://www.heraeus.com/media/media/hqs/doc\\_hqs/products\\_and\\_solutions\\_8/optics/Data\\_and\\_Properties\\_Optics\\_fused\\_silica\\_EN.pdf](https://www.heraeus.com/media/media/hqs/doc_hqs/products_and_solutions_8/optics/Data_and_Properties_Optics_fused_silica_EN.pdf).
- HO, C. K. & IVERSON, B. D. 2014. Review of high-temperature central receiver designs for concentrating solar power. *Renewable and Sustainable Energy Reviews*, 29, 835-846.
- HO, C. K., MAHONEY, A. R., AMBROSINI, A., BENCOMO, M., HALL, A. & LAMBERT, T. N. 2012. Characterization of Pyromark 2500 for High-Temperature Solar Receivers. 509-518.
- HOFFSCHMIDT, B., TÉLLEZ, F. L. M., VALVERDE, A., FERNÁNDEZ, J. S. & FERNÁNDEZ, V. 2003. Performance Evaluation of the 200-kWth HiTRec-II Open Volumetric Air Receiver. *Journal of Solar Energy Engineering*, 125, 87-94.



- HOFMANN, A., SCHENK, C. & UHLIG, R. 2009. Optical quartz glass windows for high concentrated thermal power plants. *Proceedings of SolarPACES*.
- JEDAMSKI, J., AMSBECK, L., BUCK, R., COUTURIER, R., HELLER, P., TOCHON, P., UHLIG, R. & VASQUEZ, F. 2010. Development of a Profiled Multilayer Tube for High Temperature Solar Receivers and Heat Exchangers. 483-489.
- JORGENSEN, G. 1991. Comparison of predicted optical performance with measured results for dish concentrators. National Renewable Energy Lab., Golden, CO (United States).
- JORGENSEN, G. 1993. Reflective coatings for solar applications. National Renewable Energy Lab., Golden, CO (United States).
- KOLB, G. J., ALPERT, D. J. & LOPEZ, C. W. 1991. Insights from the operation of Solar One and their implications for future central receiver plants. *Solar Energy*, 47, 39-47.
- KORZYNIETZ, R., BRIOSO, J. A., DEL RÍO, A., QUERO, M., GALLAS, M., UHLIG, R., EBERT, M., BUCK, R. & TERAJI, D. 2016. Solugas – Comprehensive analysis of the solar hybrid Brayton plant. *Solar Energy*, 135, 578-589.
- KRIBUS, A., DORON, P., RUBIN, R., KARNI, J., REUVEN, R., DUCHAN, S. & TARAGAN, E. 1999. A Multistage Solar Receiver:: The Route To High Temperature. *Solar Energy*, 67, 3-11.
- LI, Y., LIU, G., RAO, Z. & LIAO, S. 2015. Field synergy principle analysis for reducing natural convection heat loss of a solar cavity receiver. *Renewable Energy*, 75, 257-265.
- LICHTY, P., PERKINS, C., WOODRUFF, B., BINGHAM, C. & WEIMER, A. 2010. Rapid High Temperature Solar Thermal Biomass Gasification in a Prototype Cavity Reactor. *Journal of Solar Energy Engineering*, 132, 011012-011012.
- LOENEN, E. & VAN DER TEMPEL, L. 1996. Determination of absorption coefficients of glasses at high temperatures, by measuring the thermal emission. Philips Research.
- LUBKOLL, M. 2017. *Performance characteristics of a spiky central receiver air pre-heater (SCRAP)*. Stellenbosch: Stellenbosch University.
- MAHARAJ, N. 2015. *Computational and Experimental Investigation into a Tubular Cavity Receiver for a Parabolic Dish*. University of Pretoria.
- MARSBERG, J., CRAIG, K. J. & MEYER, J. P. Central solar receiver CFD modelling utilising generated heliostat field heat flux maps. 2015. 3rd Southern African Solar Energy Conference, South Africa, 11-13 May, 2015.
- MARTINEK, J. & WEIMER, A. W. 2013. Evaluation of finite volume solutions for radiative heat transfer in a closed cavity solar receiver for high temperature solar thermal processes. *International Journal of Heat and Mass Transfer*, 58, 585-596.
- MODEST, M. F. 2013. *Radiative heat transfer*, Academic press.
- MOGHIMI, M., CRAIG, K. J. & MEYER, J. P. 2015. A novel computational approach to combine the optical and thermal modelling of Linear Fresnel Collectors using the finite volume method. *Solar Energy*, 116, 407-427.
- NREL, N. R. E. L. 2017. *Concentrating Solar Power Projects* [Online]. Available: <http://sterg.sun.ac.za/publications/> [Accessed 05 February 2018].



- PYE, J., HUGHES, G., ABBASI, E., ASSELINEAU, C.-A., BURGESS, G., COVENTRY, J., KAUFER, M., VENN, F. & ZAPATA, J. 2015. Development of a higher-efficiency tubular cavity receiver for direct steam generation on a dish concentrator. *Proc. SolarPACES*.
- RAJPUT, R. 2010. *Thermal engineering*, Laxmi Publications.
- ROGER, M., RICKERS, C., UHLIG, R., NEUMANN, F. & POLENZKY, C. 2009. Infrared-Reflective Coating on Fused Silica for a Solar High-Temperature Receiver. *Journal of solar energy engineering.*, 131, 21004.
- S.T.E.R.G. 2017. *Publications* [Online]. Available: <http://sterg.sun.ac.za/publications/> [Accessed 05 February 2018].
- SEGAL, A. & EPSTEIN, M. 2003. Optimized working temperatures of a solar central receiver. *Solar Energy*, 75, 503-510.
- SOLARRESERVE. 2018. *Crescent Dunes* [Online]. Available: <http://www.solarreserve.com/en/global-projects/csp/crescent-dunes> [Accessed 02 February 2018].
- SONNTAG, R. E., BORGNACKE, C., VAN WYLEN, G. J. & VAN WYK, S. 1998. *Fundamentals of thermodynamics*, Wiley New York.
- TESSERA SOLAR. 2010. *Salt River Project (SRP)* [Online]. Available: <http://graphiquecreative.com/wp-content/sites/tessera/north-america/projects.htm> [Accessed 02 January 2018].
- TUBOSOL PE2. 2011. *TUBOSOL PE2* [Online]. Available: <http://www.puertoerrado2.com> [Accessed 03 January 2018].
- VERSTEEG, H. K. & MALALASEKERA, W. 2007. *An Introduction to Computational Fluid Dynamics: The Finite Volume Method.*, Pearson Education.
- WANG, F., SHUAI, Y., YUAN, Y., YANG, G. & TAN, H. 2010. Thermal stress analysis of eccentric tube receiver using concentrated solar radiation. *Solar Energy*, 84, 1809-1815.
- WENDELIN, T., DOBOS, A. & LEWANDOWSKI, A. 2013. SolTrace: A Ray-Tracing Code for Complex Solar Optical Systems. *NREL - Technical Report*, 303, 275-300.



# Appendix A: UDF COPY UDS TO UDM

```
#include "udf.h"
#include "sg.h"
/*=====*/
DEFINE_ON_DEMAND(copy_uds_to_udm)
{
Domain* d=Get_Domain(1);
Thread *t;
cell_t c;
thread_loop_c(t,d)
{
begin_c_loop(c,t)
{
C_UDMI(c,t,0)=C_UDSI(c,t,0);
}
end_c_loop (c,t)
}
return;
}
/*=====*/
DEFINE_SOURCE(solar_heat,c,t,dS,eqn)
{
real source;
dS[eqn]=0.0;
source=C_UDMI(c,t,0);
return source;
}
```



UNIVERSITEIT VAN PRETORIA  
UNIVERSITY OF PRETORIA  
YUNIBESITHI YA PRETORIA

}

/\*-----\*/

# Appendix B: PYTHON FUNCTIONS FOR SOLTRACE MESH IMPORT

## Code overview

The main executable code, below, and all imported modules, perform the function of interpreting a body meshed in ANSYS Mesher, and extracting a surface/s of interest, and converting these element faces into data interpretable by SolTrace. The code also defines optical properties. SolTrace is fully executable from inside the Python script, which allows the possible integration into a fully automated optimisation loop.

## Python main executable code

```
"""
```

```
Created on Wed Jul 01 10:09:07 2015
```

```
author: Justin Marsberg
```

```
This file is created to join all separately created functions
```

```
which complete various processes in the solving process including:
```

1. Reading mesh information
2. Running SolTrace
3. Interpreting SolTrace Ray data generated
4. Creating UDS for interpretation in Fluent

```
"""
```

```
from Read_MSH_Func import Read_MSH
```

```
import os
```

```
import subprocess
```

```
curr_dir = os.getcwd()
```

```
a=[]
```

```
b=[]
```

```
c=[]
```



```
mesh_file = "
```

```
mesh_file,a,b,c=Read_MSH(curr_dir,mesh_file,a,b,c)
```

```
Sol_dir = curr_dir + "\sol_bash.bat"
```

```
if os.path.isfile(Sol_dir):
```

```
try:
```

```
p = subprocess.Popen(Sol_dir)
```

```
p.wait()
```

```
except:
```

```
print "The executable.bat file is incorrect. Create this file such that SolTrace is executed with the correct script file called.\n"
```

```
print "This file should have the format:\n"
```

```
print "C:\SolTrace\2012.7.9\SolTrace.exe -s C:\SolTrace\2012.7.9\scripts\Soltrace_Script_File.lk"
```

## **Read\_\_MSH\_Func.py**

```
# -*- coding: utf-8 -*-
```

```
"""
```

```
Created on Fri Jan 23 11:54:03 2015
```

```
@author: Justin Marsberg
```

This code is written to be able to convert a.msh file to a suitable format such that elements from this file can be replicated in a SolTrace environment.

At this point in time the code is not generic and cannot replicate any geometry.

The code imports node values as defined in.msh file.

These values are with reference to the elements local coordinate system.

An aim point needs to also be defined such that element faces are directed in the correct direction.

```
"""  
  
def Read_MSH(curr_dir,mesh_file,a,b,c):  
  
    import os.path  
  
    import os  
  
    import string, re  
  
    import numpy as np  
  
    import math as m  
  
    import Optic_Lib_Tools, shutil, time  
  
  
    if mesh_file == "":  
  
        exclude = set(string.punctuation)  
  
        regex = re.compile('[%s]' % re.escape(string.punctuation))  
  
  
        dir0 = str(raw_input("Please enter the directory of the mesh file location: "))  
  
  
        while not(os.path.isdir(dir0)):  
  
            print " "  
  
            print "This is an invalid file location, please try again."  
  
            dir0 = str(raw_input("Enter the file location: "))  
  
  
            if os.path.isdir(dir0):  
  
                print " "  
  
                print "File directory is valid."
```



```
print " "
```

```
FileList = []
```

```
for file in os.listdir(dir0):
```

```
if file.endswith(".msh"):
```

```
FileList.append(file)
```

```
j = len(FileList)
```

```
if FileList:
```

```
print "List of.msh files within directory: "
```

```
print " "
```

```
for i in range(len(FileList)):
```

```
print i+1, ". ", FileList[i]
```

```
else:
```

```
print "There are no files with the.msh extension in this directory"
```

```
print " "
```

```
file_select = input("Select the file number from list to be processed: ") - 1
```

```
file_name = str(dir0 + "\\") + str(FileList[file_select])
```

```
mesh_file = file_name
```

```
f = open(file_name, 'a')
```

```
f.write('/n/n/n')
```

```
f.close()
```

```
f = open(file_name, 'r')
```



```
f.seek(0,2)
eof = f.tell()
f.seek(0,0)
current_pos = f.tell()

node_num = 0
sec_num = 0
nodes = []
Faces = []
BCs = []
new_line = f.readline()

while current_pos!= eof:
if new_line.startswith("(10 (") and not new_line.startswith("(10 (0)":
new_line = f.readline()
sec_num+=1
while not new_line.startswith(")"))):
temp_node = map(float,new_line.split())
node_num+=1
nodes.append([sec_num, node_num, temp_node[0], temp_node[1], temp_node[2]])
new_line = f.readline()

if new_line.startswith("(13 (") and not new_line.startswith("(13 (0)": #Element-type Zone-id Node1
Node2 Node3 Node4
temp_line = regex.sub(" ", new_line)
temp_line1 = [int(s,16) for s in temp_line.split()]
new_line = f.readline()
while not new_line.startswith(")"))):
if temp_line1[len(temp_line1)-1] == 0: #For mixed elements
```



```
temp_store = []
temp_store = [int(s,16) for s in new_line.split()]
if len(temp_store) > 0:
if temp_store[0] == 3:
Faces.append([temp_store[0], temp_line1[1],temp_store[1],temp_store[2],temp_store[3]])
if temp_store[0] == 4:
Faces.append([temp_store[0],
temp_line1[1],temp_store[1],temp_store[2],temp_store[3],temp_store[4]])

if temp_line1[len(temp_line1)-1] == 3: #For triangular elements
temp_store = [int(s,16) for s in new_line.split()]
if len(temp_store) > 0:
Faces.append([3, temp_line1[1],temp_store[0],temp_store[1],temp_store[2]])

if temp_line1[len(temp_line1)-1] == 4: #For quad elements
temp_store = [int(s,16) for s in new_line.split()]
if len(temp_store) > 0:
Faces.append([4, temp_line1[1],temp_store[0],temp_store[1],temp_store[2],temp_store[3]])

new_line = f.readline()

if new_line.startswith("(45 ("):
temp_str = regex.sub(",new_line)
temp_arr = [s for s in temp_str.split()]
if temp_arr[2] == "wall":
Zone_id = int(temp_arr[1])
BCs.append([Zone_id, temp_arr[3]])
```

```
new_line = f.readline()
```

```
current_pos = f.tell()
```

```
f.close()
```

```
Faces = np.array(Faces)
```

```
"""Select boundaries which are to be used as Soltrace Surfaces.
```

```
Boundary names should match named selections (after punctuation removal), which have been defined  
in ANSYSsys or other meshing programs. Only wall boundaries can be selected.
```

```
Additionally, at this stage of the setup, boundaries are further defined by assigning optical properties to  
them.
```

```
These properties are recorded inside a library which will be displayed to the Python Console or viewable  
inside
```

```
the working folder in.txt format.
```

```
Surfaces will also need to be defined as refractive or reflective."""
```

```
if len(a)==len(b)==len(c)==0:
```

```
k=0
```

```
BC_select = []
```

```
if BCs:
```

```
print "Select boundaries to be processed:"
```

```
print " "
```

```
for k in range(len(BCs)):
```

```
print k+1, ". ", BCs[k][1]
```

```
else:
```

```
print "There are no boundaries which are classified as walls."
```

```
print " "
```

```
BC_select = input("Select the Boundaries to be processed in list form[:]: ")
```

```
print Optic_Lib_Tools.optical_library_reader(curr_dir)[1]
```

```
add_entry = str(raw_input('Add an entry to the Optical Library[Y or N]:'))
```

```
while add_entry == 'Y' or add_entry == 'y':
if Optic_Lib_Tools.add_to_optic_library(curr_dir):
print "Entry added successfully."
add_entry = str(raw_input('Add an entry to the Optical Library[Y or N]:'))
else:
print "Optical property not added to library. This surface name already exists."
add_entry = str(raw_input('Add an entry to the Optical Library[Y or N]:'))
BC_prop_set = []
BC_RorR = []
for i in BC_select:
print "\nFor surface " + str(BCs[i-1]) + " select Optic properties and if surface is reflective or refractive:
"

cnt = 1
for i in Optic_Lib_Tools.optical_library_reader(curr_dir)[1]:
print str(cnt) + ". " + i
cnt+=1
BC_prop_set.append(input("\nChoose Optic set number from library: ")-1)
BC_RorR.append(input("Choose 1=Reflective or 2=Refractive: "))

rows = len(Faces)-1
temp_file_name = curr_dir + "\Boundary_Info.txt"
if os.path.isfile(temp_file_name):
os.remove(temp_file_name)
f = open(temp_file_name,'a')
for j in range(len(BC_RorR)):
temp = str(BC_select[j]) + '\n' + str(BC_prop_set[j]) + '\n' + str(BC_RorR[j]) + '\n'
f.write(temp)
f.close()
else:
```



```
BC_select = a
```

```
BC_prop_set = b
```

```
BC_RorR = c
```

```
Optic_Lib_Tools.temp_folder_create(curr_dir,BC_prop_set)
```

```
Element = []
```

```
Node_Vals = []
```

```
Node_Coords = [] #Coordinates of each node[X1,X2,X3,X4,Y1,Y2,Y3,Y4,Z1,Z2,Z3,Z4]
```

```
Element_Area = []
```

```
approx_circle = 1 #This will determine if surfaces in Soltrace are approximated by a circular aperture  
with radius to ensure surface area remains constant
```

```
"""
```

```
3 element types are possible:
```

```
0: circular aperture with approximated area
```

```
3: triangular aperture
```

```
4: quad aperture
```

```
"""
```

```
for i in (BC_select):
```

```
Zone_ID = BCs[i-1][0]
```

```
for j in range(rows):
```

```
Normal_Vec = []
```

```
Centre = []
```

```
if Faces[j][1]==Zone_ID:
```

```
Node1 =nodes[Faces[j][2]-1]
```

```
Node2 =nodes[Faces[j][3]-1]
```

```
Node3 =nodes[Faces[j][4]-1]
```

```
Vec1 = np.array([Node1[2]-Node2[2],Node1[3]-Node2[3],Node1[4]-Node2[4]])
```

```

Vec2 = np.array([Node1[2]-Node3[2],Node1[3]-Node3[3],Node1[4]-Node3[4]])
temp_Vec = np.cross(Vec1,Vec2)
C = 10
magnitude = C*(1/(temp_Vec[0]**2+temp_Vec[1]**2+temp_Vec[2]**2)**(0.5))

Normal_Vec = [temp_Vec[0]*magnitude,temp_Vec[1]*magnitude,temp_Vec[2]*magnitude]

if Faces[j][0] == 3:
    Centre =
    [(Node1[2]+Node2[2]+Node3[2])/3,(Node1[3]+Node2[3]+Node3[3])/3,(Node1[4]+Node2[4]+Node3
    [4])/3]

    Element.append([Centre[0],Centre[1],Centre[2],Centre[0]+Normal_Vec[0],Centre[1]+Normal_Vec[1
    ],Centre[2]+Normal_Vec[2],3,i])

    N_L1 = m.sqrt((Centre[0]-Node1[2])**2 + (Centre[1]-Node1[3])**2 + (Centre[2]-Node1[4])**2)
    N_L2 = m.sqrt((Centre[0]-Node2[2])**2 + (Centre[1]-Node2[3])**2 + (Centre[2]-Node2[4])**2)
    N_L3 = m.sqrt((Centre[0]-Node3[2])**2 + (Centre[1]-Node3[3])**2 + (Centre[2]-Node3[4])**2)
    maxL = max(N_L1,N_L2,N_L3)

    if approx_circle == 1:
        a = m.sqrt((Node1[2]-Node2[2])**2 + (Node1[3]-Node2[3])**2 + (Node1[4]-Node2[4])**2)
        b = m.sqrt((Node1[2]-Node3[2])**2 + (Node1[3]-Node3[3])**2 + (Node1[4]-Node3[4])**2)
        c = m.sqrt((Node2[2]-Node3[2])**2 + (Node2[3]-Node3[3])**2 + (Node2[4]-Node3[4])**2)
        p = (a+b+c)/2
        A = m.sqrt(p*(p-a)*(p-b)*(p-c))
        d = 2*maxL
        Node_Vals.append([d,0,0,0,0,0,0])

    Node_Coords.append([Node1[2],Node1[3],Node1[4],Node2[2],Node2[3],Node2[4],Node3[2],Node3[
    3],Node3[4],None,None,None])

    Element_Area.append(A)

    elif approx_circle == 0:

```

```
Node_Vals.append([Node1[2],Node1[3],Node2[2],Node2[3],Node3[2],Node3[3],0,0])
```

```
Node_Coords.append([Node1[2],Node1[3],Node1[4],Node2[2],Node2[3],Node2[4],Node3[2],Node3[3],Node3[4],None,None,None])
```

```
if Faces[j][0] == 4:
```

```
Node4=nodes[Faces[j][5]-1]
```

```
Centre = [(Node1[2]+Node2[2]+Node3[2]+Node4[2])/4,(Node1[3]+Node2[3]+Node3[3]+Node4[3])/4,(Node1[4]+Node2[4]+Node3[4]+Node4[4])/4]
```

```
Element.append([Centre[0],Centre[1],Centre[2],Centre[0]+Normal_Vec[0],Centre[1]+Normal_Vec[1],Centre[2]+Normal_Vec[2],4,i])
```

```
N_L1 = m.sqrt((Centre[0]-Node1[2])**2 + (Centre[1]-Node1[3])**2 + (Centre[2]-Node1[4])**2)
```

```
N_L2 = m.sqrt((Centre[0]-Node2[2])**2 + (Centre[1]-Node2[3])**2 + (Centre[2]-Node2[4])**2)
```

```
N_L3 = m.sqrt((Centre[0]-Node3[2])**2 + (Centre[1]-Node3[3])**2 + (Centre[2]-Node3[4])**2)
```

```
N_L4 = m.sqrt((Centre[0]-Node4[2])**2 + (Centre[1]-Node4[3])**2 + (Centre[2]-Node4[4])**2)
```

```
maxL = max(N_L1,N_L2,N_L3,N_L4)
```

```
if approx_circle == 1:
```

```
a = m.sqrt((Node1[2]-Node2[2])**2 + (Node1[3]-Node2[3])**2 + (Node1[4]-Node2[4])**2)
```

```
b = m.sqrt((Node2[2]-Node3[2])**2 + (Node2[3]-Node3[3])**2 + (Node2[4]-Node3[4])**2)
```

```
c = m.sqrt((Node1[2]-Node3[2])**2 + (Node1[3]-Node3[3])**2 + (Node1[4]-Node3[4])**2)
```

```
d = m.sqrt((Node4[2]-Node3[2])**2 + (Node4[3]-Node3[3])**2 + (Node4[4]-Node3[4])**2)
```

```
e = m.sqrt((Node1[2]-Node4[2])**2 + (Node1[3]-Node4[3])**2 + (Node1[4]-Node4[4])**2)
```

```
p1 = (a+b+c)/2
```

```
p2 = (c+d+e)/2
```

```
A1 = m.sqrt(p1*(p1-a)*(p1-b)*(p1-c))
```

```
A2 = m.sqrt(p2*(p2-c)*(p2-d)*(p2-e))
```

```
A = A1+A2
```

```
#d = m.sqrt(4*A/m.pi)
```

```
d = 2*maxL
```

```
Element_Area.append(A)
```

```
Node_Vals.append([d,0,0,0,0,0,0])
```

```
Node_Coords.append([Node1[2],Node1[3],Node1[4],Node2[2],Node2[3],Node2[4],Node3[2],Node3[3],Node3[4],Node4[2],Node4[3],Node4[4]])
```

```
elif approx_circle == 0:
```

```
Node_Vals.append([Node1[2],Node1[3],Node2[2],Node2[3],Node3[2],Node3[3],Node4[2],Node4[3]])
```

```
Node_Coords.append([Node1[2],Node1[3],Node1[4],Node2[2],Node2[3],Node2[4],Node3[2],Node3[3],Node3[4],Node4[2],Node4[3],Node4[4]])
```

```
temp_folder_path = curr_dir + '\Processed Mesh'
```

```
if os.path.exists(temp_folder_path):
```

```
shutil.rmtree(temp_folder_path)
```

```
time.sleep(1)
```

```
os.mkdir(temp_folder_path)
```

```
C_x = open(temp_folder_path + '\C_x.txt','a',1)
```

```
C_y = open(temp_folder_path + '\C_y.txt','a',1)
```

```
C_z = open(temp_folder_path + '\C_z.txt','a',1)
```

```
Xaim = open(temp_folder_path + '\Xaim.txt','a',1)
```

```
Yaim = open(temp_folder_path + '\Yaim.txt','a',1)
```

```
Zaim = open(temp_folder_path + '\Zaim.txt','a',1)
```

```
Elem_type = open(temp_folder_path + '\Elem_type.txt','a',1)
```

```
Nodes_X1 = open(temp_folder_path + '\Node_X1.txt','a',1)
```

```
Nodes_Y1 = open(temp_folder_path + '\Node_Y1.txt','a',1)
Nodes_X2 = open(temp_folder_path + '\Node_X2.txt','a',1)
Nodes_Y2 = open(temp_folder_path + '\Node_Y2.txt','a',1)
Nodes_X3 = open(temp_folder_path + '\Node_X3.txt','a',1)
Nodes_Y3 = open(temp_folder_path + '\Node_Y3.txt','a',1)
Nodes_X4 = open(temp_folder_path + '\Node_X4.txt','a',1)
Nodes_Y4 = open(temp_folder_path + '\Node_Y4.txt','a',1)
Surf_Num = open(temp_folder_path + '\Surf_Num.txt','a',1)
Node_array = open(temp_folder_path + '\Node_array.txt','a',1)
Element_A = open(temp_folder_path + '\Element_Areas.txt','a',1)
print "\nProcessing files...\n"

for x in range(len(Element)):
    C_x.write(str(Element[x][0])+"\n")
    C_y.write(str(Element[x][1])+"\n")
    C_z.write(str(Element[x][2])+"\n")
    Xaim.write(str(Element[x][3])+"\n")
    Yaim.write(str(Element[x][4])+"\n")
    Zaim.write(str(Element[x][5])+"\n")
    if approx_circle == 0:
        Elem_type.write(str(Element[x][6])+"\n")
    elif approx_circle == 1:
        Elem_type.write(str(0)+"\n")
    Nodes_X1.write(str(Node_Vals[x][0])+"\n")
    Nodes_Y1.write(str(Node_Vals[x][1])+"\n")
    Nodes_X2.write(str(Node_Vals[x][2])+"\n")
    Nodes_Y2.write(str(Node_Vals[x][3])+"\n")
    Nodes_X3.write(str(Node_Vals[x][4])+"\n")
    Nodes_Y3.write(str(Node_Vals[x][5])+"\n")
```



```
Nodes_X4.write(str(Node_Vals[x][6])+"\n")
Nodes_Y4.write(str(Node_Vals[x][7])+"\n")
Surf_Num.write(str(Element[x][7])+"\n")
Element_A.write(str(Element_Area[x])+"\n")
for n in range(12):
    if n < 11:
        Node_array.write(str(Node_Coords[x][n])+",")
    else:
        Node_array.write(str(Node_Coords[x][11])+"\n")

C_x.close(), C_y.close(), C_z.close(), Xaim.close()
Yaim.close(), Zaim.close(), Elem_type.close()
Nodes_X1.close(),Nodes_Y1.close(),Nodes_X2.close()
Nodes_Y2.close(),Nodes_X3.close(),Nodes_Y3.close()
Nodes_X4.close(),Nodes_Y4.close(), Surf_Num.close()
Node_array.close(),Element_A.close()
return mesh_file,BC_select,BC_prop_set,BC_RorR
```

## **Optic\_Lib\_Tools.py**

```
# -*- coding: utf-8 -*-
```

```
"""
```

```
Created on Fri Jun 26 20:11:03 2015
```

```
author: Justin Marsberg
```

```
"""
```

```
import numpy as np
```

```
def optical_library_reader(curr_dir):
```

```
    f = open(curr_dir + '\optic_property_lib.txt','r')
```



```
f.seek(0,2)
eof = f.tell()
f.seek(0,0)
current_pos = f.tell()
templine=f.readline()
a = []
names = []
while not templine.startswith("Optical"):
templine=f.readline()
current_pos = f.tell()
while current_pos!= eof:
temp_Arr = np.zeros(4)
templine = f.readline()
temp_list = templine.split(",")

for i in range(len(temp_list)):
if i==0:
names.append(temp_list[i])
else:
temp_Arr[i-1] = float(temp_list[i])
if len(a)!=0:
a = np.row_stack((a,temp_Arr))
else:
a = temp_Arr
current_pos = f.tell()
f.close()
return a,names

def add_to_optic_library(curr_dir):
```



```
Lib_Arr,Names = optical_library_reader(curr_dir)

f = open(curr_dir + '\optic_property_lib.txt','a')

temp = input('Insert values for new material optic property in the list
format:\n["Name",Refectivity,Transmisivity,Slope Error(mrad),Specularity Error(mrad)]:\n')

if Names._contains_(temp[0]):

f.close()

return False

else:

line = "\n" + temp[0] + "," + str(temp[1]) + "," + str(temp[2]) + "," + str(temp[3]) + "," + str(temp[4])

f.write(line)

f.close()

return True

def temp_folder_create(curr_dir,Lib_Line):

import shutil,os,time

a,names = optical_library_reader(curr_dir)

curr_dir1 = curr_dir + "\\temp_lib_files"

r,c = np.shape(a)

if os.path.isdir(curr_dir1):

shutil.rmtree(curr_dir1)

time.sleep(1)

print "Folder deleted"

os.mkdir(curr_dir1)
```



```
for i in Lib_Line:
temp_f = open(curr_dir1 + "\\" + str(i) + ".txt",'a')
temp_f.write(str(names[i]) + "\n")
for j in a[i][:]:
temp_f.write(str(j) + "\n")
temp_f.close()
```

# Appendix C: SOLTRACE FUNCTIONS

## Code overview

The following list of functions written in C# are executable SolTrace scripts which automate the process of interpretation of files created by the Python scripts from the.msh files, and import the elements as well as optic and trace options.

Once a full trace is completed a number of data exporting scripts are available to write the ray-tracing data to a file which can be interpreted by ANSYSsys Fluent.

## Import mesh elements

```
/* *****
configure an optical property data set
***** */
clearoptics();

/* *****
add a stage with multiple flat elements
***** */
curr_dir = cwd() + "\\Processed Mesh';
outln(curr_dir);
C_x=split(read_text_file(curr_dir + "\\C_x.txt"),"n");
C_y=split(read_text_file(curr_dir + "\\C_y.txt"),"n");
C_z=split(read_text_file(curr_dir + "\\C_z.txt"),"n");
Xaim=split(read_text_file(curr_dir + "\\Xaim.txt"),"n");
Yaim=split(read_text_file(curr_dir + "\\Yaim.txt"),"n");
Zaim=split(read_text_file(curr_dir + "\\Zaim.txt"),"n");
Elem_type=split(read_text_file(curr_dir + "\\Elem_type.txt"),"n");
X1=split(read_text_file(curr_dir + "\\Node_X1.txt"),"n");
Y1=split(read_text_file(curr_dir + "\\Node_Y1.txt"),"n");
X2=split(read_text_file(curr_dir + "\\Node_X2.txt"),"n");
Y2=split(read_text_file(curr_dir + "\\Node_Y2.txt"),"n");
```

```
X3=split(read_text_file(curr_dir + "\\Node_X3.txt"),"\n");
Y3=split(read_text_file(curr_dir + "\\Node_Y3.txt"),"\n");
X4=split(read_text_file(curr_dir + "\\Node_X4.txt"),"\n");
Y4=split(read_text_file(curr_dir + "\\Node_Y4.txt"),"\n");
Surf_Num = split(read_text_file(curr_dir + "\\Surf_Num.txt"),"\n");
Optic_lines = split(read_text_file(cwd() + "\\Boundary_Info.txt"),"\n");
Element_Area = split(read_text_file(curr_dir + "\\Element_Areas.txt"),"\n");
num_rows = #C_x;
outln("There are " + num_rows + " elements");
line_num = 0;

while(line_num < num_rows)
{
    Array[line_num][0]=to_real(C_x[line_num]);
    Array[line_num][1]=to_real(C_y[line_num]);
    Array[line_num][2]=to_real(C_z[line_num]);
    Array[line_num][3]=to_real(Xaim[line_num]);
    Array[line_num][4]=to_real(Yaim[line_num]);
    Array[line_num][5]=to_real(Zaim[line_num]);
    Array[line_num][6]=to_real(Elem_type[line_num]);
    Array[line_num][7]=to_real(Surf_Num[line_num]);

    Nodes[line_num][0]=to_real(X1[line_num]);
    Nodes[line_num][1]=to_real(Y1[line_num]);
    Nodes[line_num][2]=to_real(X2[line_num]);
    Nodes[line_num][3]=to_real(Y2[line_num]);
    Nodes[line_num][4]=to_real(X3[line_num]);
    Nodes[line_num][5]=to_real(Y3[line_num]);
    Nodes[line_num][6]=to_real(X4[line_num]);
```

```
Nodes[line_num][7]=to_real(Y4[line_num]);

Element_Area_Arr[line_num][0] = to_real(Element_Area[line_num]);
line_num=line_num+1;
}

num_rows1 = #Optic_lines;
line_num = 0;
i = 0;
while(line_num < num_rows1)
{

    Optic_info[i][0] = to_real(Optic_lines[line_num]);
    Optic_info[i][1] = to_real(Optic_lines[line_num+1]);
    Optic_info[i][2] = to_real(Optic_lines[line_num+2]);
    line_num = line_num + 3;
    i = i + 1;
}

file_list = dir_list(cwd() + "\\temp_lib_files","*");
len_fl = #file_list;
cnt = 0;
while(cnt < len_fl)
{

    temp_info = split(read_text_file(cwd() + "\\temp_lib_files\\" + file_list[cnt]),"\n");
    len_ti = #temp_info;
    Optic_Lib[cnt][0] = to_string(temp_info[0]);
    i=1;
```



```
while (i < len_ti)
{
    Optic_Lib[cnt][i] = to_real(temp_info[i]);
    i=i+1;
}
close(temp_info);
cnt=cnt+1;
}

clearstages();

addstage('Eurodish');
activestage('Eurodish');
stageopt('Eurodish',{'virtual'=false,'multihit'=true,'tracethrough'=false});

i = 0;
surf_change = 0;
old_Surf = 300;

while (i < num_rows)
{
    if (Array[i][7] != old_Surf)
    {
        Name = 'Surface_' + to_string(Array[i][7]) + " (" +
Optic_Lib[Optic_info[surf_change][1]][0] + ")";
addoptic(Name);
        opticopt(Name, 1, {'refl'=Optic_Lib[Optic_info[surf_change][1]][1],
'trans'=Optic_Lib[Optic_info[surf_change][1]][2],
'errslope'=Optic_Lib[Optic_info[surf_change][1]][3],
'errspec'=Optic_Lib[Optic_info[surf_change][1]][4]});
    }
}
```



```
    opticopt(Name,          2,          {'refl'=Optic_Lib[Optic_info[surf_change][1]][1],
'trans'=Optic_Lib[Optic_info[surf_change][1]][2],
'errslope'=Optic_Lib[Optic_info[surf_change][1]][3],
'errspec'=Optic_Lib[Optic_info[surf_change][1]][4]});

    if (Optic_info[surf_change][2]==1)
        {inter = 'Reflection';}
    else
        {inter = 'Refraction';}
    surf_change++;
}

addelement();
stateEN = true;
if (Array[i][6] == 3)
{
    elementopt(i,{'en'=stateEN, 'x'=Array[i][0], 'y'=Array[i][1], 'z'=Array[i][2],
'ax'=Array[i][3], 'ay'=Array[i][4], 'az'=Array[i][5],
'zrot'=0,
'aper'=['i',Nodes[i][0],Nodes[i][1],Nodes[i][2],Nodes[i][3],Nodes[i][4],Nodes[i][5],Nodes[i][6],Nodes
[i][7]],
'surf'=['f',0,0,0,0,0,0,0,0], 'interact'= inter, 'optic' = Name, 'comment' =
Element_Area_Arr[i] } );
}

if (Array[i][6] == 4)
{
    elementopt(i,{'en'=stateEN, 'x'=Array[i][0], 'y'=Array[i][1], 'z'=Array[i][2],
'ax'=Array[i][3], 'ay'=Array[i][4], 'az'=Array[i][5],
'zrot'=0,
'aper'=['q',Nodes[i][0],Nodes[i][1],Nodes[i][2],Nodes[i][3],Nodes[i][4],Nodes[i][5],Nodes[i][6],Node
s[i][7]],
```



```
'surf'=['f',0,0,0,0,0,0,0,0,0], 'interact'= inter, 'optic' = Name, 'comment' =  
Element_Area_Arr[i] } );  
  
}  
  
if (Array[i][6] == 0)  
{  
  
    elementopt(i, {'en'=stateEN, 'x'=Array[i][0], 'y'=Array[i][1], 'z'=Array[i][2],  
    'ax'=Array[i][3], 'ay'=Array[i][4], 'az'=Array[i][5],  
    'zrot'=0,  
'aper'=['c', Nodes[i][0], Nodes[i][1], Nodes[i][2], Nodes[i][3], Nodes[i][4], Nodes[i][5], Nodes[i][6], Nodes  
[i][7]],  
    'surf'=['f',0,0,0,0,0,0,0,0,0], 'interact'= inter, 'optic' = Name, 'comment' =  
Element_Area_Arr[i] } );  
}  
old_Surf=Array[i][7];  
  
i=i+1;  
  
}  
  
notice("Elements Added Successfully");  
  
//adds the Eurodish and insulation to the initial stage, as well as the specified optical properties  
  
addoptic('Dish');  
opticopt('Dish', 1, {'refl'=1.0, 'trans'=0, 'errslope'=0.0001, 'errspec'=0.0001});  
opticopt('Dish', 2, {'refl'=1.0, 'trans'=0, 'errslope'=0.0001, 'errspec'=0.0001});  
  
addoptic('Insulation');  
opticopt('Insulation', 1, {'refl'=0.0, 'trans'=0, 'errslope'=0.0001, 'errspec'=0.0001});  
opticopt('Insulation', 2, {'refl'=0.0, 'trans'=0, 'errslope'=0.0001, 'errspec'=0.0001});  
  
addelement();
```

```

elementopt(i,{'en'=true, 'x'=0,'y'=0, 'z'=-0.587,
            'ax'=0, 'ay'=0, 'az'=1,
            'zrot'=0, 'aper'=['c',1.5,0,0,0,0,0,0],
            'surf'=['p',0.90667,0.90667,0,0,0,0,0,0],'interact'= 'Reflection',
            'optic' = 'Dish' } );

addelement();

elementopt(i+1,{'en'=true, 'x'=0,'y'=0, 'z'=0.16635,
            'ax'=0, 'ay'=0, 'az'=-1,
            'zrot'=0, 'aper'=['c',0.22,0,0,0,0,0,0], /* was 0.2*/
            'surf'=['c',40.5429,0,0,0,0,0,0],'interact'= 'Reflection', /* was 29.79 */
            'optic' = 'Insulation' } );

addelement();

elementopt(i+2,{'en'=true, 'x'=0,'y'=0, 'z'=-0.1,
            'ax'=0, 'ay'=0, 'az'=1,
            'zrot'=0, 'aper'=['r',0.0127,2,0,0,0,0,0],
            'surf'=['f',0,0,0,0,0,0,0,0],'interact'= 'Reflection',
            'optic' = 'Insulation', 'comment' = 'stingshadow' } );

/* *****

Run Simulation

***** */

Ray_Count = to_int(in("Enter number of desired ray intersections"));

traceopt({'rays'= Ray_Count, 'maxrays' = 10*(Ray_Count), 'cpus' = 8, 'include_sunshape'=true,
'optical_errors'=true});

trace();

```



## Write.ip file

```
/* *****  
  
Write Element Hits in stage to File  
  
***** */  
  
activestage(liststages()[0]);  
  
//subtract number of elements added on top of meshed elements  
elem_num = nelements()-3;  
outln(elem_num);  
DNI = to_real(in("Enter DNI value[W/m2]"));  
j=0;  
fileName = to_string(in("Enter file name for interpolation file"));  
fileID=cwd() + "\\ip files\\seed results\\" + fileName + "XYZ.ip";  
notice("Writing file to " +fileID);  
if (file_exists(fileID))  
    {if (yesno("File with this name already exists. Overwrite and continue?"))  
        {remove_file(fileID);}  
    else  
        {break;}  
    }  
  
mkdir(cwd() + "\\ip files\\seed results',true);  
open(fileID,'w');  
write_line(1,2);  
write_line(1,3);  
write_line(1,to_string(elem_num));  
write_line(1,1);  
write_line(1,"uds-0");
```



```
t = to_real(in("Enter thickness of tube [m]"));
while (j < elem_num)
    {
    write_line(1,(elementopt(j){"x"}));
    j = j+1;
    }
outln(j);
j=0;
while (j < elem_num)
    {
    write_line(1,(elementopt(j){"y"}));
    j = j+1;
    }
outln(j);
j=0;
while (j < elem_num)
    {
    write_line(1,(elementopt(j){"z"}));
    j = j+1;
    }
outln(j);
j=0;
close(1);

for (k = 0; k < 20; k++){
seed_nr = ceil(1000*rand());
traceopt({'rays'=1000000, 'maxrays'=10000000, 'cpus'=8,'seed'=seed_nr});
trace();
fileID=cwd() + "\\ip files\\seed results\\" + fileName + "seed_"+to_string(seed_nr) + ".ip";
```



```
open(fileID,'w');
outln("Writing: "+fileID);
T_area = (sundata(){"xmax"}-sundata(){"xmin"})*(sundata(){"ymax"}-sundata(){"ymin"});
ppr = DNI*T_area/sundata(){"nrays"};
while (j < elem_num)
    {
        area = to_real(elementopt(j){"comment"});
        elem_hits = rayhits(0,j,1);
        Elem_Watts = (ppr*elem_hits)/(area*t);
        write_line(1,(Elem_Watts));
        j = j+1;
    }
outln(j);
j=0;
close(1);
}
```



## Write profile file

```
/* *****  
  
Write Element Hits in stage to File  
  
***** */  
  
activestage(liststages()[0]);  
elem_num = nelements()-3;  
outln(elem_num);  
j=0;  
  
fileID=cwd() + "\\prof files\\" + to_string(in("Enter file name for profile file")) + ".prof";  
notice("Writing file to " +fileID);  
if (file_exists(fileID))  
    {if (yesno("File with this name already exists. Overwrite and continue?"))  
        {remove_file(fileID);}  
    else  
        {break;}  
    }  
  
T_area = (sundata>{"xmax"}-sundata>{"xmin"})*(sundata>{"ymax"}-sundata>{"ymin"});  
DNI = to_real(in("Enter DNI value[W/m2]));  
ppr = DNI*T_area/sundata>{"nrays"};  
  
mkdir(cwd() + "\\prof files',true);  
open(fileID,'w');  
write_line(1,("heat-prof point " + to_string(elem_num)+ "));  
write_line(1,"x");  
t = to_real(in("Enter thickness of tube [m]));
```



```
while (j < elem_num)
    {
        write_line(1,(elementopt(j){"x"}));
        j = j+1;
    }
write_line(1,"");
write_line(1,"(y)");
outln(j);
j=0;
while (j < elem_num)
    {
        write_line(1,(elementopt(j){"y"}));
        j = j+1;
    }
write_line(1,"");
write_line(1,"(z)");
outln(j);
j=0;
while (j < elem_num)
    {
        write_line(1,(elementopt(j){"z"}));
        j = j+1;
    }
write_line(1,"");
write_line(1,"(heat-val)");
outln(j);
j=0;

while (j < elem_num)
```



```
{  
  area = to_real(elementopt(j){"comment"});  
  elem_hits = rayhits(0,j,1);  
  Elem_Watts = (ppr*elem_hits)/(area); //This value is adjusted from a power per volume to  
  power per surface area. ie. thickness of tube is not considered.  
  write_line(1,(Elem_Watts));  
  j = j+1;  
}  
write_line(1,"");  
  
outln(j);  
close(fileID);
```